Structure de couches antiferromagnétiques ultra-minces utilisées dans les systèmes à couplage d'échange: alliages à base de Mn; couches de CoO

Maurizio de Santis

▶ **To cite this version:**

Maurizio de Santis. Structure de couches antiferromagnétiques ultra-minces utilisées dans les systèmes à couplage d'échange: alliages à base de Mn; couches de CoO. Science des matériaux [cond-mat.mtrl-sci]. Université Joseph-Fourier - Grenoble I, 2014. tel-00995451

HAL Id: tel-00995451

https://theses.hal.science/tel-00995451

Submitted on 23 May 2014

HAL is a multi-disciplinary open access archive for the deposit and dissemination of scientific research documents, whether they are published or not. The documents may come from teaching and research institutions in France or abroad, or from public or private research centers.

L'archive ouverte pluridisciplinaire **HAL**, est destinée au dépôt et à la diffusion de documents scientifiques de niveau recherche, publiés ou non, émanant des établissements d'enseignement et de recherche français ou étrangers, des laboratoires publics ou privés.

Université de Grenoble

Structure of ultrathin antiferromagnetic films for exchange coupling systems: metallic Mn alloys and insulating CoO films.

Habilitation à diriger des recherches

Maurizio De Santis

date de soutenance : 7 fevrier 2014

COMPOSITION DU JURY :

Bruno GILLES, Président
Sylvie ROUSSET, Rapporteur
Conrad BECKER, Rapporteur
Dominique GIVORD, Examinateur
Geoffroy PREVOT, Examinateur

Contents

Foreword 1

1. Introduction 2

1.1. Exchange coupling at the interface. 3

1.2. Theoretical models 5
a) Domain walls close to uncompensated interface
b) “Spin-flop”
c) Random field model
d) Domain state model
e) Coercivity enhancement

2. Surface X-ray diffraction 9

2.1. X-ray diffraction from surfaces and ultrathin films 11
a) Introduction to x-ray diffraction
b) Crystal truncation rods.
c) X-ray diffraction from the surface region.

2.2. Surface x-ray diffraction experimental set-up 17

2.3. Angular settings of the *Z*-axis diffractometer 18

2.4. Measurements of the rod intensities. 19
a) Polarization factor.
b) Lorentz correction
c) Lorentz correction in SXRD and rod intercept correction
d) Linear γ table correction
e) Area correction
f) Stationary scans
g) Line shape and detector acceptance correction
h) Total correction factor

3. MnPt and MnNi alloys 27

3.1. Bulk atomic and magnetic structure 27

3.2. ultrathin films 28

3.3. Chemical order 28
a) Order parameter

b) Antiphase domains
c) Domains in MnPt films

3.4. 2D Mn surface alloys 31
a) Structure of Ni(110)-*c*(2×2)Mn (revisited)
b) Pt(110)-*p*(2×1)Mn

3.5. Codeposited MnPt ultrathin films. 38

4. CoO/PtCo/Pt(111) 42

4.1. PtCo/Pt(111) 43

4.2. CoO/Pt(111) 45
a) Surface structure and morphology of CoO/Pt(111)
b) Structure of ultrathin CoO/Pt(111) films

4.3. Magnetic properties of NiO/CoO/PtCo/Pt(111) multilayers 53

5. Conclusion and perspectives 55

Foreword

This manuscript resembles a selection of x-ray diffraction experiments that I have performed over more than one decade on the French “cooperative research group on the interfaces (CRG-IF)” beamline at ESRF. It is dedicated to the study of the structure of two-dimensional (2D) and ultrathin magnetic films, and of ferromagnetic/antiferromagnetic bilayers.

In the first chapter theories elaborated to explain the exchange bias phenomenon are reviewed. This is intended as an introduction for young experimentalists to understand which are the relevant structural parameters in exchange coupling.

The second chapter is dedicated to a introductory but complete treatment of the surface x-ray diffraction technique in grazing incidence geometry. It is conceived as a working tool, the diffractometer settings and formula about the instrumental resolution being given for a specific (z-axis) geometry.

Chapter 3 is devoted to the structure and chemical order in metallic Mn based 2D alloys and ultrathin films, and to the illustration of the relationship with their magnetic properties.

In chapter 4 the growth and the structure of CoO ultrathin films is discussed, showing as reciprocal space analysis and direct space imaging complete themselves.

Chapter 5 is dedicated to the short and medium term perspective.

The results discussed here are in large part the fruit of a collective research activity (I give here more relevance to the structural studies and to the growth processes, where my contribution is more original). A part of them are the subject of the PhD thesis of Marcio M. Soares. I have to acknowledge for their contribution all the members of the research group on surfaces, interfaces and nanostructures of the Néel institute at which I belong, and Helio Tolentino. Great thanks also to the CRG-IF staff, and specially to Gilles Renaud, Olivier Ulrich and Olivier Geaymond.

The STM experiments have been performed during my year of secondment at Vienna in the Peter Varga's group, where I learned the basis of the scanning tunneling spectroscopy technique. The study of the properties of the Co/Pt(111) system is a collaboration with the Giorgio Rossi group at the ELETTRA synchrotron light source.

The exhaustive list of collaborators can be extracted from the related publications.

I would like still to thanks two former member of our group, Robert Baudoing-Savois and Yves Gauthier, who learned my a lot about surface physics.

Finally, I am indebted to Wolgang Moritz and Ian K. Robinson for all what they explained me about surface x-ray diffraction during a one month staying in Munich and Brookhaven, respectively.

1. Introduction

In the last two decades, the research on antiferromagnetic films has been boosted by the emergence of the so called spintronics. In this technology, information is carried by the electron spin and not only by its charge. It uses spin-dependent effects that arise from the interaction between the spin of the carrier and the magnetic properties of the material. The discovery of the giant magnetoresistive effect (GMR)[1,2] is considered as the beginning of spintronics. The nobel prize in physics 2007 was awarded jointly to Albert Fert and Peter Grünberg for their experiment on this subject.

GMR is observed in a layered structure composed of alternated ferromagnetic and non-magnetic films. The electrical resistance of the system is lower when the magnetic layers are aligned parallel then when there are aligned antiparallel. The GMR effect is exploited in spin valves. In such devices an antiferromagnetic layer pins one of the two magnetic layers of the system, while the second one can be rotated, for example under the influence of the stray fields above the stored bits in current high-density magnetic storage disks. The spin valve is then the main element of a high-sensitivity read-head.

An antiferromagnetic film is also employed as pinning layer in magnetic tunnel junctions. The free layer is in this case separated by a ultrathin insulating barrier, commonly made by aluminum oxide. The resulting tunneling current depend also on the relative orientation of the two ferromagnetic layers, and changes in the magnetoresistence are even larger than in spin valves. Schematic structures of a spin valve and of a magnetic tunnel junction are depicted in Fig. 1(a) and 1(b) respectively, taken from ref. [3]

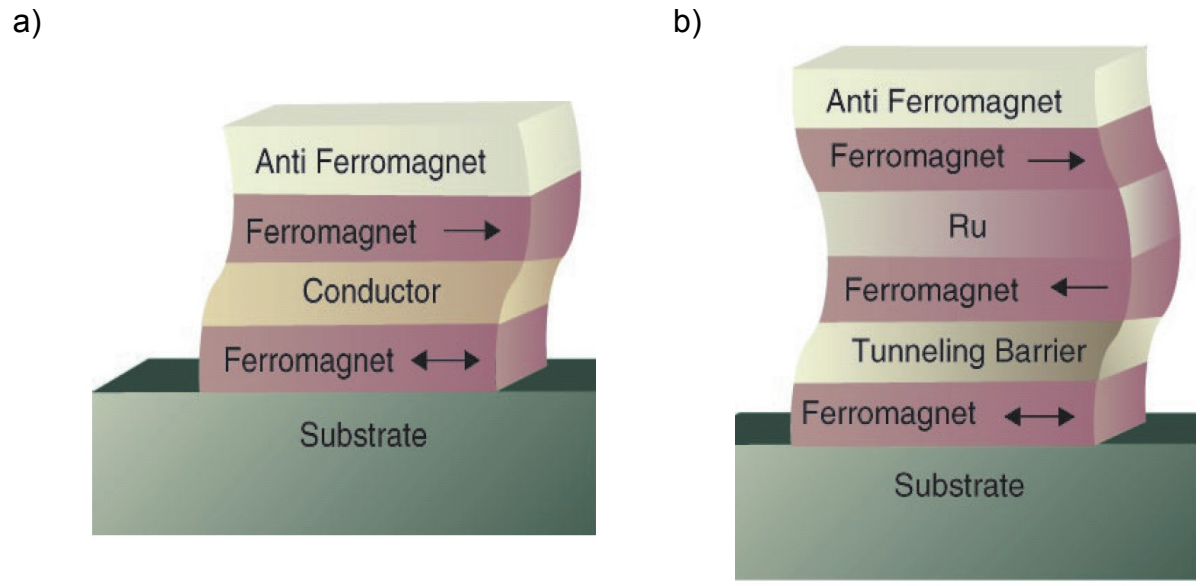

FIG. 1 Spin-dependent transport structures. a) Spin valve. b) Magnetic tunnel junction. (taken from ref. 3)

Applications for spin valves and magnetic tunnel junctions include read heads for hard

1 M. N. Baibich, J. M. Broto, A. Fert, F. Nguyen Van Dau, F. Petroff, P. Eitenne, G. Creuzet, A. Friederich, and J. Chazelas, *Phys. Rev. Lett.* **61**, 2472 (1988).

2 J. Barnas, A. Fuss, R. Camley. P. Grunberg, W. Zinn, *Phys. Rev. B* **42**, 8110 (1990).

3 S. A. Wolf, D. D. Awschalom, R. A. Buhrman, J. M. Daughton, S. von Molnár, M. L. Roukes, A. Y. Chtchelkanova and D. M. Treger, *Science* **294**, 1488 (2001)

drives, magnetic field sensors, magnetoresistive random access memories, and galvanic isolators.

1.1. Exchange coupling at the interface.

In 1956 Meiklejohn and Bean discovered that nanoparticles formed by a metallic cobalt core and a cobalt oxide shell show a new magnetic anisotropy, described as an exchange anisotropy.[4] This magnetic interaction is commonly observed when a material with ferromagnetic (FM)-antiferromagnetic (AFM) interfaces is cooled through the Néel temperature T_N of the AFM (supposed here to be lower than the Curie temperature T_C of the FM layer), in the presence of a saturating magnetic field. The material shows then a unidirectional anisotropy that can be observed both tracing the torque curve, which is proportional to the sine of the angle between the easy direction of magnetization and the applied magnetic field, or the hysteresis loop, which is displaced by the amount H_{EB} (exchange bias field).

This phenomenon is observed in a large variety of interfaces and materials (surface oxides, films, nanoparticles, spin glasses, …). It can also involve ferrimagnets, which can play both the role of the FM and of the AFM material. A large panorama of systems showing exchange bias (EB) can by found in the revue from Nogues and Schuller.[5] Here we will focus mainly on EB materials in the form of ultrathin film bilayers, which allow the best control and characterization of the interfaces.

The basic energies involved in this phenomenon are exchange and anisotropy. The former controls the magnetic order and the coupling at the interface, while the latter determine the preferred orientation. They have their origin in the electron correlation and in the crystal field energies, respectively. The general description assume that the ferromagnet has a large exchange but a relatively small anisotropy compared to the AFM. The exchange bias then can be explained qualitatively making these assumptions.[5]

Applying a magnetic field in the temperature interval between T_N and T_C ($T_N < T_C$) the FM aligns with the field, while the AFM is in the paramagnetic state and the spins are oriented random (Fig. 2(1)). When cooling below the Néel temperature in presence of the field (field cooling), the interfacial spins of the AFM align ferromagnetically with the FM layer, while the spins in the next plane follow the antiferromagnetic order (Fig. 2(2)). When the field is reversed to describe the hysteresis loop of the FM layer, the AFM spins at the interface remain unchanged (for large enough anisotropy), and they exert a torque on the FM spins. This is equivalent to an additional inner field (exchange bias field) displacing the hysteresis loop (Fig. 2(3-5)).

4 W. H. Meiklejohn and C. P. Bean, Phys. Rev. **102**, 1413 (1956)
5 J. Nogués, Ivan K. Schuller, JMMM **192**, 203 (1999)

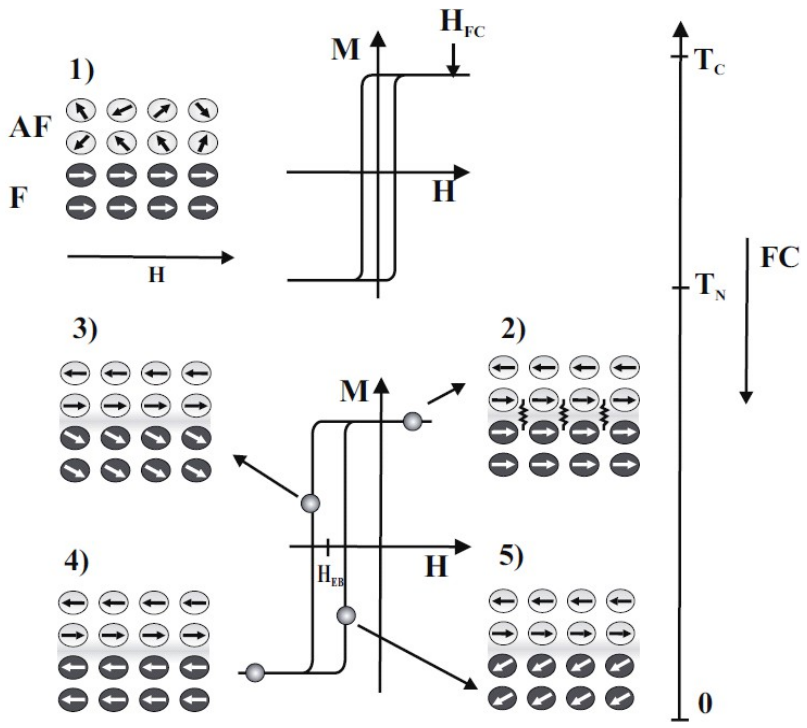

FIG. 2 (Taken from ref.[6]) Sketch of the spin configuration at the FM-AFM interface resulting from a field cooling (1-2) and then following an hysteresis loop (2-5).

The energy per unit area corresponding to such a model is given by[7,8,9]

$$E = -\mu_0 H M t_f \cos\theta - \frac{\Delta\sigma}{2}\cos\theta + K_f t_f \sin^2\theta, \qquad (1.1)$$

Where H is the applied magnetic field, M is the saturation magnetization of the ferromagnet, t_f is the thickness of the ferromagnetic film, $\Delta\sigma$ is the exchange interfacial energy difference for unit area, and K_f is the uniaxial anisotropy in the ferromagnet (with the easy axis parallel to the interface and to the AFM one). The angle θ is taken between the magnetization and the uniaxial anisotropy easy axis of the ferromagnet. The bias field is then

$$H_{EB} = \frac{\Delta\sigma}{2\mu_0 M t_f}. \qquad (2.1)$$

Taking a simple cubic structure with the same a lattice constant for the AFM and FM films,

$$\Delta\sigma = \frac{2J_i}{a^2}, \qquad (3.1)$$

6 F. Radu, H. Zabel, in Springer Tracts in Modern Physics, Springer-Verlag, Berlin Heidelberg, **227**, 97 (2007)
7 W. H. Meiklejohn, J. Appl. Phys. 33, 1328 (1962)
8 Malozemoff, Phys. Rev. **B 35**, 3679 (1987)
9 R. L. Stamps, J. Phys. D: Appl. Phys. **33** R247 (2000)

where J_i is the interatomic exchange across the interface, the coupling being assumed ferromagnetic.

This model allows to understand qualitatively the EB phenomenon, however is far too simplified to explain it quantitatively. For example, the predicted H_{EB} is two orders of magnitudes too large. In Fig. 2 the AFM interface is fully uncompensated, i.e. all the spins of the interfacial AFM plane are oriented in the same direction. The picture described above in unable to explain the coupling in films with compensated AF/AFM interfaces. In this last ones the two AFM magnetic sublattice compensate in the interface plane, whose net magnetic moment vanishes. The AF/AFM systems present several additional features which reveal the complexity of the interface coupling. Among them, the existence of a blocking temperature T_B above which the exchange bias vanish. This temperature can be considerably lower than the (bulk) T_N (as for example in ultrathin epitaxial Fe3O4/CoO bilayers,[10] for a review see ref. 5). The origin of this effect seems to be related to the thickness or to the grain size of the AFM layer. Another remarkable feature is the observation of positive EB,[11] which cannot be explained within the simple picture of Fig. 2. Several systems exhibit the training effect, i.e. the dependence of the exchange bias field on the number of hysteresis loops performed, which is a clear evidence that a metastable equilibrium establishes after field cooling. Another characteristic of EB systems is the increases of the coercivity below T_B.

In the next paragraph the basic principles of the theoretical model which can help to understand the complex properties observed in the EB materials are reviewed.

1.2. Theoretical models

Several theories have been developed in the last 30 years to explain the exchange coupling at the AFM/FM interfaces. Each of them take into account some aspects of the interaction and it is well suited for a class of materials and interfaces. A review is given in the papers from Berkowitz and Takano[12], Kiwi[13] and Stamps.[9] The description below is aimed to a qualitative understanding and to give hints on which new systems could show interesting properties and which are the key parameters to look for in the experiments.

a) Domain walls close to uncompensated interface

It was already recognize by Néel that a perfectly rigid AFM, and a perfectly uniform FM layer, may not properly describe the lowest energy magnetic configuration near the interface.[14] This idea was developed by Mauri *et al.*.[15] They started from the model described above, and considered that an AFM domain develops at the interface, which has the effect of imposing an upper limit on the exchange energy. They assumed that the AFM film thickness is much larger than the domain wall and that the FM thickness is too small to form domains in the direction perpendicular to the interface. Then the energy difference obtained by reversing the magnetization is that one of the wall in the AFM film:

$$\Delta\sigma = 4\sqrt{AK} \qquad (4.1)$$

10 P. J. van der Zaag, A. R. Ball, L. F. Feiner, R. M. Wolf, P. A. A. van der Heijden, J. Appl. Phys **79**, 5103 (1996)
11 J. Nogues, D. Lederman, T. J. Moran, Ivan K. Schuller, Phys. Rev. Lett. **76**, 4624 (1996)
12 A. E. Berkowitz, K. Takano, J. Mag. Mag. Mat. **200**, 552 (1999)
13 M. Kiwi, J. Mag. Mag. Mat. **234**, 584 (2001)
14 Néel, Ann. Phys., **2**, 61 (1967)
15 D. Mauri, H. C. Siegmann, P. S. Bagus, E. Kay, J. Appl. Phys. **62**, 3047 (1987)

where $A \simeq J/a$ is the exchange stiffness and K is the in-plane uniaxial anisotropy energy of the AFM layer. This gives realistic values of H_E. Figs. 3(b) and 3(c) show a schematic side view of possible atomic moment configurations close to interface when reversing the polarization with respect to the field cooled configuration [Fig. 3(a)]. The exchange interfacial energy term is given by the frustrated bonds (indicated by stars) and by the domain wall, respectively.

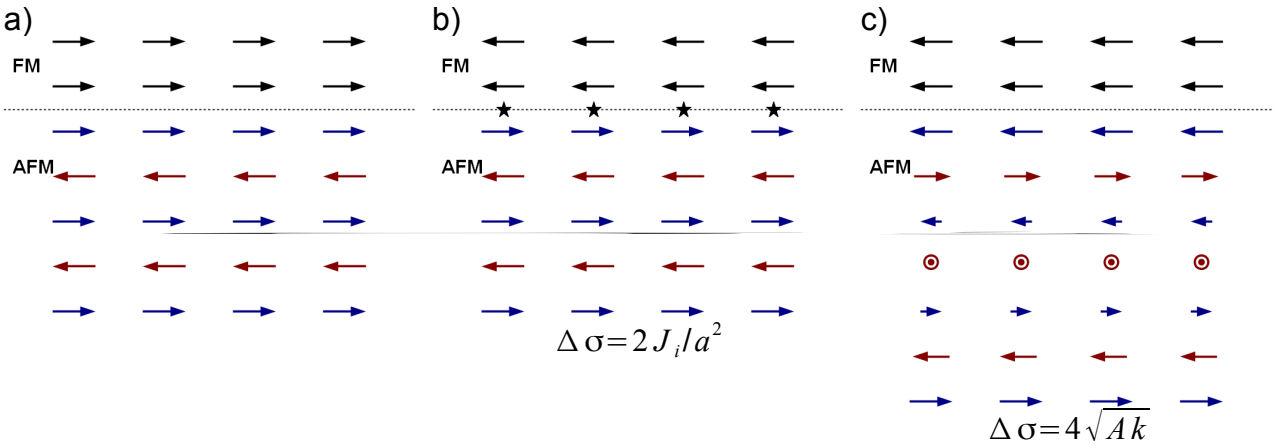

FIG. 3. Schematic side view of atomic moment configurations at the interface after a field cooling (i), and reversing the polarization for a rigid model (ii) and with the formation of a domain wall (iii).

b) "Spin-flop"

A microscopic explanation of EB in films with compensated FM/AFM interfaces was given by Koon.[16] Its model takes a simple body centered tetragonal magnetic structure. The FM/AFM interface is parallel to the (110) plane, and the AFM uniaxial anisotropy is along the [001] direction (Fig. 4). Micromagnetic calculations show a perpendicular orientation between the FM and AFM axis directions in the ground state. Close to the interface a canting is observed with the AFM spins slightly rotating in the direction of the FM ones or at the opposite, in the case of ferromagnetic and antiferromagnetic exchange coupling at the interface, respectively.

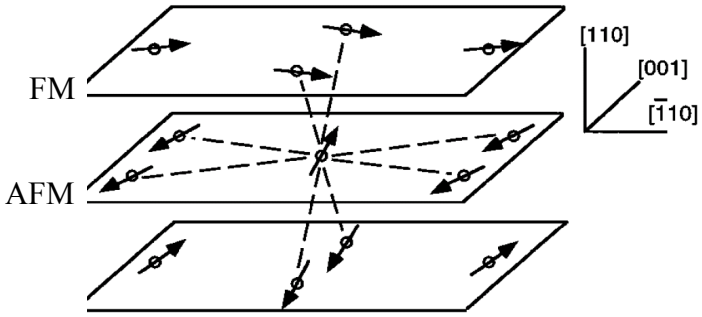

FIG. 4 Spin configuration near the FM/AFM interface plane (from ref. 16)

However, as discussed later,[17] this model should not lead to exchange bias. Instead, it gives rise to an uniaxial anisotropy which can explain the increase in coercivity observed in exchange coupled systems.

16 N. C. Koon, Phys. Rev. Lett. **78**, 4865 (1997)
17 T. C. Schulthess, W. H. Butler, Phys. Rev. Lett. **81**, 4516 (1998)

c) Random field model

The role of roughness was put in evidence for the first time by Malozemoff,[8] who pointed out as a randomly disordered interface can lead to an expression for the exchange bias close to the Mauri result. Fig. 5 shows a single monoatomic bump at a compensated AFM/FM interface. At the microscopic level, this defect generates an exchange interfacial energy difference by reversing the magnetization, owing to the different number of frustrated bonds. They are represented by stars in Fig. 5(a) and 5(b), respectively, where the coupling at the interface is supposed to be ferromagnetic. For a rough surface such a local unidirectional anisotropy is randomly oriented parallel or antiparallel with respect to the AFM anisotropy axis, and its average value decreases with the size of the considered area.

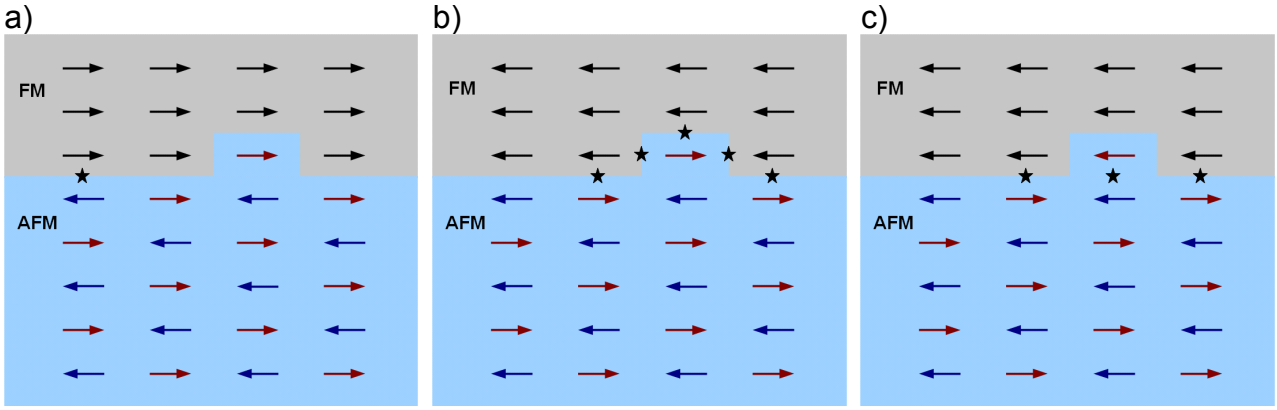

FIG. 5 Spin orientation at a compensated FM/AFM interface after field cooling (a), and after inversing the applied field considering frozen AFM spins only (b), and allowing rotable spins (c).

When the spin anisotropy is maintained on a region which is large enough, it will be energetically favorable to rotate the anisotropy field creating a domain wall in the AFM film, as shown in Fig. 6. This domain wall is perpendicular to the interface and is permanently present in the AFM layer. Then the expression for the exchange interfacial energy difference resembles to eq. (4):[8]

$$\Delta\sigma = \frac{4 n_z \sqrt{A K}}{\pi^2} \quad , \qquad (5)$$

where n_z is a number of order unity and is related to an effective number of frustrated bonds. Depending on the relative values of AFM and interface exchange coupling, a lower exchange anisotropy if found by inverting the spin polarization of the atomic defects, as shown in Fig. 5(c). This introduce the concept of rotable AFM spins at the interface. This was observed during the experiments we performed on the MnPt films.

It is easy to show that the local anisotropy can also be induced by steps and kinks at the interface.

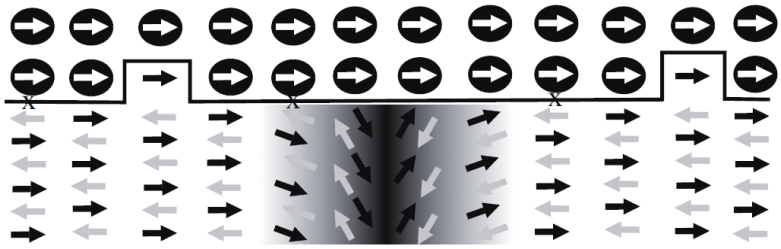

FIG. 6 Schematic view of a vertical domain wall in the AF layer. It appears as an energetically favorable state of F/AF systems with rough interfaces (from ref. 6)

d) Domain state model[18]

This model is also based on the random field theory. But in this case the random field does not originate at the interface, but is dues to defects in the volume of the AFM layer. It is well established that a diluted antiferromagnet in an external field develops a domain state when cooled below its Néel temperature.[19] Statistically unbalanced impurities between the two sublattices result in a net magnetization which couples to the external field. This alter the spin structure at the interface, resulting in exchange coupling. This mechanism can explain some of the experimental finding. Field cooling in a strong field aligns the surplus magnetization of the AFM domains. This yield positive change bias, if the coupling between AFM and FM is antiparallel. The training effect can also been explained with a rearrangement of the AFM domain structure during the hysteresis loops, which results in a lost of the domain state magnetization.

The random field approach is quite general, and can be applied independently on the detailed origin of the local exchange anisotropy. This is the case for example for the random alloy effect proposed by Kouvel,[20] where the statistical composition fluctuation play the role of the roughness in the Malozemoff model or of the impurities in the domain state one. This mechanism is pertinent to the MnPt films.

e) Coercivity enhancement

Several explanations have been proposed to explain the coercivity enhancement, based on domain wall pinning. Kim and Stamps[21] developed a theory based on the partial domain-wall model of Mauri *et al.*,[15] where magnetic defects in the AFM, such as local variations in the exchange or magnetocristalline anisotropy, lead to an attractive potential for the domain wall that can pin the wall under suitable conditions. The depinning transition leads to a coercivity enhancement.

f) Spin-glass like model

The interface between AFM and FM layers is never perfect. Depending on the growing conditions structural inhomogeneities, chemical intermixing and deviation from stoichiometry are observed, resulting in a transition region from the pure AFM state to a pure FM state. This magnetically disordered interface has been modeled with a frustrated spin system. A part of the AFM spins are uncompensated and frozen-in, they are responsible for EB. An other part has a weaker anisotropy, which allows some spins of the

18 P. Miltényi, M. Gierlings, J. Keller, B. Beschoten G. Güntherodt, U. Nowak, K. D. Usadel, Phys. Rev. Lett. **84,** 4224 (2000)
19 W. Kleemann, Int. J. Mod. Phys. B **7,** 2469 (1993)
20 J. S. Kouvel, J. Phys. Chem. Solids **24**, 795 (1963)
21 Joo-Von Kim, R. L. Stamps, Phys. Rev. B **71**, 094405 (2005)

AFM layer to rotate together with the magnetization of the FM layer. This interfacial part is a frustrated (spin-glass-like) region and gives rise to an increased coercivity. The behavior of this EB system was studied in details by Radu *et al.* as function of the effective exchange bias and spin disorder anisotropy.[22,6] The advantage of such a model is that it does not require a detailed description of the interface.

22 F. Radu, A. Westphalen, K. Theis-Bröhl, H. Zabel, J. Phys.: Condens. Matter **18** L29 (2006)

2. Surface X-ray diffraction

We have seen in the previous chapter how the EB properties depend critically on the spin configuration and on the structure of the interface and of the magnetic films. Key parameters are the surface roughness and the structural defects at the interface, but magnetic domains size in the films play also a crucial role. Most of the recent theoretical works consider explicitly the domain structure in the AFM layer, which usually shows a stronger anisotropy and hence a smaller domain wall width with respect to the FM.[8] In AFM metallic alloys, magnetic domain size and chemical order are strictly related. Interface structure and chemical order correlation length will be discussed in this manuscript.

One ingredient that, to my knowledge, is not explicitly taken into account in any EB model is the misfit between the AFM and FM lattice of epitaxial layers. Fig 7 shows an interface model where the misfit accommodation is shared between strain and dislocations. In this example, the dislocation induces a net exchange coupling in a otherwise compensated interface. Moreover the exchange coupling depends on the relative atomic positions at the interface. Lattice matching and dislocations will be discussed in the chapter devoted to CoO films.

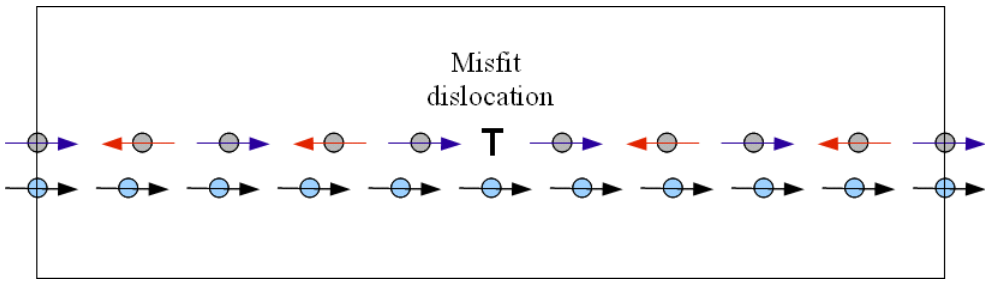

FIG. 7 Model of misfit accommodation with the appearance of dislocations in an epitaxial AFM layer on top of a FM substrate.

When ultrathin films are involved, the finite-size effects on the ordering temperature needs to be considered. Intrinsic fundamental properties such as the magnetic exchange interactions, magnetic moment and magnetic anisotropies change markedly in ultrathin films as compared with their bulk counterparts.[23,24] Such properties are moreover influenced by the epitaxial growth induced strains.

Exchange interaction and spin structure are quite different in metallic and insulating AFM materials. Most of the AFM films used in high-density read-heads were metallic Mn alloys. In these films the spin structure is generally more complex, multi-spin sublattices as well as temperature-dependent spin phases are often observed.[25] In the last decade the more robust insulating AFM materials have gained importance in EB applications. Most of them are transition metal monoxides (mainly CoO and NiO), and exhibit a much simpler spin structure. However, as will be pointed out in the following, their interface with metallic magnetic films is much less sharp.

23 C. A. F. Vaz, J. A. C. Bland, G. Lauhoff, Rep. Prog. Phys. **71**, 056501 (2008)
24 F. J. Himpsel, J. E. Ortega, G. J. Mankey, R. F. Willis, Advances in Physics, **47**, 511, 1998
25 K. Fukamichi, R. Y. Umetsu, A. Sakuma, C. Mitsumata, Handbook of Magnetic Materials, edited by K. H. J. Buschow, Volume 16, Elsevier (2006)

I will focus on the AFM films, which plays a mayor role in most of the theories. A detailed description of the films structure at an atomic level is the starting point for modeling their properties. Here epitaxial layers grown by molecular beam epitaxy (MBE) on single crystal substrates are considered. On such a kind of samples the structural analysis can performed using *in-situ* x-ray diffraction.

The next section is dedicated to the theory of x-ray diffraction applied to ultrathin films. A details description of sample preparation methods and of employed ultra high vacuum techniques is not in the objectives of this manuscript.

2.1. X-ray diffraction from surfaces and ultrathin films

The mode of nucleation and initial growth of epitaxial films is governed by the bonding between deposit and substrate. The surface and interface energies determine the growth mode. In thermodynamical equilibrium three classic growth mode are observed: a layer by layer growth, the formation of islands directly on the substrate, on an initial flat layer followed by island growth (e.g. ref. [26]). In all of them, the initial deposit can be strained elastically to match the substrate. This is referred to as "pseudomorphic" growth.[27]

When the atomic planes are in registry at the interface, the x-ray diffraction pattern of the substrate and of the film has to be considered as a whole and the two contributions cannot be separated. This topic is discussed in details in several papers.[28,29,30]

a) Introduction to x-ray diffraction

The scattering of a photon of wave vector $\vec{K}_i$ and energy ω_i (here $\hbar=1$) on an ensemble of atoms can by described in quantum mechanics by the cross section

$$d\sigma = 2\pi |V_{21}|^2 \frac{\omega_f^2 \, d\Omega}{(2\pi)^3} \qquad (2.1)$$

which define the probability of scattering a photon at final energy ω_f in the solid angle $d\Omega$ in the direction defined by $\vec{K}_f$ (see e.g. ref. [31]), accompanied by an atomic transition from the energy level E_1 to $E_2 = E_1 + \omega_i - \omega_f$. The matrix element is given by:

$$V_{21} = \sum_{n \neq i} \left(\frac{V_{2n}^f V_{n1}^i}{E_1 + \omega - E_n} + \frac{V_{2n}^i V_{n1}^f}{E_1 - E_n - \omega_f} \right) \quad , \qquad (2.2)$$

which is the first non zero term in the perturbation theory which describe the scattering process. The potential V describe the electromagnetic interaction and in the dipole approximation is simply $V = -\vec{d} * \vec{E}$, where $\vec{d}$ is the atom dipole and $\vec{E}$ the electric field. In the x-ray diffraction, only the elastic term (Rayleigh scattering) is relevant because the inelastic scattering is incoherent (Raman or Compton scattering) and therefore does

26 E. Bauer, Z. Kristallogr. **110**, 395 (1958)
27 Epitaxial Growth part B, edited by J. W. Matthews, Academic Press (1975)
28 I. K. Robinson, D. J. Tweet, Reports on Progress in Physics, **55**, 599 (1992)
29 I. K. Robinson, Handbook of Synchrotron radiation, vol. 3, North Holland, Amsterdam (1991)
30 R. Feidenhans'l, Surface Science Report, **10**, 105 (1989)
31 L. D. Landau, E. M. Lifšits, Teoria quantistica relativistica chap. VI, Editori Riuniti (1978)

not give any interference pattern. For large photon energies and in the dipole approximation, eq. (2.1) reduces to the classical formula of Thomson scattering. For an atomic cluster, it can be written:

$$\Delta\sigma = \frac{\int |\sum_{atoms} Z_j|^2 e^4}{m^2 c^4} \sin^2\theta \, d\Omega \qquad (2.3)$$

θ being the angle between the electric field of the incoming photon and the scattering direction.

In the dipole approximation the electromagnetic wave is supposed constant over the size of the cluster, which does not held for x-ray scattering. Then the sum in (2.3) needs to be replaced by an integral of the electronic density with the associated phase of the incoming and scattered photons (this integral will be indicated as $S(\vec{Q})$ and will be called in the following scattering amplitude):

$$\sum_{atoms} Z_j \Rightarrow \int e^{i\vec{K}_f\vec{r}} \rho(\vec{r}) d^3 r \, e^{-i\vec{K}_i\vec{r}} \approx \sum_{atoms} f^\circ_j(Q) e^{i\vec{Q}\vec{r}_j} \equiv S(\vec{Q}) \quad , \qquad (2.4)$$

where $\vec{Q} = \vec{K}_f - \vec{K}_i$ is the momentum transfer.

The the x-ray scattering cross section can then be written in the form

$$d\sigma = \frac{|S(\vec{Q})|^2 e^4}{m^2 c^4} \sin^2\theta \, d\Omega \quad . \qquad (2.5)$$

The atomic form factor, $f^\circ_j(Q)$, is defined as the Fourier transform of the electron density for the atom j. It depends on the modulus of the momentum transfer and not on its direction, in the limit of spherically symmetric electronic density, which is a good enough approximation for most of atoms. For photon energies close to a transition between electronic energy levels of the atom, eq. (2.2) contains a complex resonant term (anomalous scattering) which in a first approximation depends on energy only. The atomic form factor becomes in this case $f_j(Q,\omega) = f^\circ_j(Q) + f'_j(\omega) + if''_j(\omega)$. This is a tabulated function for all atoms in the periodic table.

Lets consider now a crystal (assumed for simplicity block shaped).[32] The periodic repetition of the unit cell is defined by the three vectors $\vec{a}_1$, $\vec{a}_2$ and $\vec{a}_3$ (crystal axes). The structure factor $F_u(\vec{Q})$ is defined as

$$F_u(\vec{Q}) = \sum_{Unit\,cell} f_j(Q) e^{\frac{-B_j Q^2}{16\pi^2}} e^{i\vec{Q}\vec{r}_j} \quad . \qquad (2.6)$$

Here a damping term has been added, which takes into account the (harmonics) oscillations of the atoms around their equilibrium positions. The Debye parameter B_j is temperature dependent and is proportional to the means square displacement from the atomic equilibrium positions. We obtain $S(\vec{Q})$ summing over the Bravais lattice:

$$S(\vec{Q}) = F_u(\vec{Q}) \sum_{n_1=0}^{N_1-1} \sum_{n_2=0}^{N_2-1} \sum_{n_3=0}^{N_3-1} e^{i\vec{Q}(n_1\vec{a}_1 + n_2\vec{a}_2 + n_3\vec{a}_3)} \quad . \qquad (2.7)$$

32 B. E. Warren X-RAY DIFFRACTION, Dover publications, New York (1969)

This sum can be easily performed, yielding

$$|S(\vec{Q})|^2=|F_u(\vec{Q})|^2\prod_{j=1}^{3}\left(\frac{\sin^2 N_j\vec{Q}\,\vec{a}_j/2}{\sin^2\vec{Q}\,\vec{a}_j/2}\right) \quad . \qquad (2.8)$$

Lets write now the momentum transfer in the basis of the reciprocal space vectors:

$$\vec{Q}=h\vec{b}_1+k\vec{b}_2+l\vec{b}_3 \qquad (2.9)$$

Replacing in (2.8), it is easy to observe that the three terms of the product have a maximum for integer h, k and l, respectively. This is equivalent to the Laue conditions for the diffraction which reduces to the Bragg law.

b) Crystal truncation rods.

The theory exposed up to now is kinematic, which means that only single scattering processes are considered. This is justified by the magnitude of the interaction ($\alpha=e^2/mc^2=1/137$). Multiple scattering effects however needs to be taken into account at least in two cases: for perfect crystals at Bragg angle, where the incoming wave is strongly attenuated (extinction) and the diffracted beam is a secondary source of scattering; and when the incidence angle of the x-rays is below the critical angle for total reflection.[30] This last case applies in particular to grazing incidence small angle x-ray scattering (GISAXS) experiments.[33,34] In studying the diffraction from ultrathin epitaxial films we are interested in the scattered intensity away from substrate Bragg peaks, and kinematics diffraction is rigorously valid. A comparison of surface x-ray diffraction (SXRD) in kinematics and dynamical theories can be find in ref.[35]. In the following, absorption of the x-ray beam in the crystal will be added only (this allows the sum over the Bravais lattice in the direction perpendicular to the surface to converge). Lets us now consider an x-ray beam impinging on the surface of a semi-infinite single crystal, taken coincident with the $\vec{a}_1\vec{a}_2$ plane. The sum

$$\sum_{n_3=0}^{N_3-1} e^{i n_3\vec{Q}\,\vec{a}_3} \qquad (2.10)$$

in eq. (2.7) becomes:

$$\sum_{n_3=0}^{\infty} e^{-i n_3\vec{Q}\,\vec{a}_3}e^{-n_3\varepsilon}=\frac{1}{1-e^{-i\vec{Q}\,\vec{a}_3}e^{-\varepsilon}} \quad . \qquad (2.11)$$

The term $e^{-\varepsilon}$ represents the x-ray absorption between two next (001) planes. It is needed for the convergence of the series but can be approximated to unity in the final result.
Writing the (2.8) for integer h, k values, we obtain:

33 G. Renaud, Surf. Sci. Rep. 32, 1 (1998)
34 G. Renaud, HDR, Université de Grenoble (2011)
35 V. M. Kaganer, Phys. Rev. B **75**, 245425 (2007)

$$|S(h,k,Q_3)|^2 = N_1^2 N_2^2 |F_u(h,k,Q_3)|^2 \left|\frac{1}{2\sin \vec{Q}\vec{a}_3/2}\right|^2 \quad . \qquad (2.12)$$

This formula shows a characteristic variation of the scattered intensity from a crystal surface as function of the momentum transfer perpendicular to the surface. This line-shape is called crystal truncation rod (CTR) and is indexed with the in plane Miller indexes (h k). Remembering that $\vec{Q}\vec{a}_3 = l\,\vec{b}_3\vec{a}_3 = 2\pi l$, it can be rewritten as:

$$|S(h,k,l)|^2 = N_1^2 N_2^2 |F_u(h,k,l)|^2 \left|\frac{1}{2\sin \pi l}\right|^2 = I_{CTR} \quad . \qquad (2.13)$$

where l takes non-integer values. At its minimum, the CTR intensity is equivalent to that one of half a 2D crystal of sides $N_1 a_1$, $N_2 a_2$ and a_3 . This is about 7 orders of magnitude less than a Bragg peak. In general synchrotron radiation is mandatory for measuring such low intensities, however experiments involving heavy atomic elements were performed using powerful rotating anode x-ray generators (see for example reference [36]).

An alternative way to find out the CTR distribution uses the Fourier transform (FT) properties. A semi-infinite crystal can be described by the product of a infinite lattice and the step function. Then the scattered amplitude $S(\vec{Q})$ is the convolution of the reciprocal lattice with the function $(i\vec{Q}\vec{a}_3)^{-1}$, FT of the step function. Summing all the strikes emanating from each Bragg peak leads to the CTR dependence discussed above.[28] The FT of the step function decreases slowly with Q , resulting in a detectable intensity all along the CTR. Any surface roughness has the effect of reducing such an intensity in between the Bragg peaks.[37] A commonly used approximation (the so-called β model[37]) describes the substrate roughness with an occupancy distribution β^n for the layer n above the last fully occupied one, resulting in pyramidal islands. The attenuation of the CTR intensity is then given by[38]

$$R_\beta = \frac{(1-\beta)^2}{(1-\beta)^2 + 4\beta \sin^2 \dfrac{\pi (l - l_{Bragg})}{M_{layers}}} \quad , \qquad (2.14)$$

where l_{Bragg} is the l value of the nearest Bragg peak and M_{layers} is the number of layers in the unit cell. It is important to realize that the relevant intensity measured in-between Bragg peaks along the CTR is mainly due to the fact that the surface is flat and not to the fact that the crystal has a finite size.

c) X-ray diffraction from the surface region.

The x-ray scattering amplitude from a film deposited onto a substrate can be simply written as the sum of the scattering from the substrate and from the atoms close to the surface:

$$S(\vec{Q}) = S_{Bulk}(\vec{Q}) + S_{Surf.}(\vec{Q}) \quad , \qquad (2.15)$$

36 H. L. Meyerheim, M. De Santis, W. Moritz, I. K. Robinson, Surf. Sci. **418**, 295 (1998)
37 I. K. Robinson, Phys. Rev. B **33**, 3830 (1986)
38 E. Vlieg, J. Appl. Cryst. **33**, 401 (2000)

where the first term contains all substrate atoms in bulk positions and the second term the deposited atoms and the substrate atoms close to the surface with displaced positions with respect to bulk. In the simple case of coherent (or pseudomorphic) epitaxy, the sum on the Bravais lattice in the two direction parallel to the surface gives delta-like functions as in Eq. (2.8): the scattering is observed at integer h and k values. Perpendicular to the surface, an intensity distribution is observed that is described through a generalized structure factor F, function of the continuous variable l :[38]

$$F(h,k,l)=F_{Bulk}+\sum_{j}^{\substack{surface\\unit\ cell}} f_j \theta_j e^{\frac{-B_j Q^2}{16\pi^2}} e^{2\pi i(hx_j+ky_j+lz_j)} \quad , \tag{2.16}$$

where

$$F_{Bulk}=\frac{F_u}{1-e^{-2\pi i l}e^{-\varepsilon}} \quad . \tag{2.17}$$

Here x_j, y_j, z_j, are the atomic positions and θ_j is an occupancy, which takes into account that an atomic site can be not occupied in each surface cell. The sum is on a surface unit cell that has the same in plane lattice vectors of the substrate, and which includes, in the direction perpendicular to the surface, all atoms that do not belong to the bulk lattice.

When a $(n_1\times n_2)$ surface reconstruction is observed, the surface cell in (2.15) is correspondingly larger. Beside the (h k) CTR, additional diffraction rods are observed at (h/n_1 k/n_2) in substrate reciprocal lattice units. Their intensity depends on the structure of the surface layer only.

Above a given thickness which is function of the misfit,[39] an epitaxial film relax and eventually takes its own bulk lattice parameter. Then the scattering amplitude can be written:

$$S(\vec{Q})=e^{i\varphi}F_{Bulk}\frac{\prod_{j=1}^{2}\sin N_j\vec{Q}\vec{a}_j/2}{\sin\vec{Q}\vec{a}_j/2}+e^{i\varphi'}\sum_{n}^{\substack{surface\\unit\ cell}} f_n\theta_n e^{\frac{-B_j Q^2}{16\pi^2}} e^{2\pi i(hx_n+ky_n+lz_n)}\frac{\prod_{j=1}^{2}\sin M_j\vec{Q}\vec{a}_j^{\,surf}/2}{\sin\vec{Q}\vec{a}_j^{\,surf}/2} \quad , \tag{2.18}$$

and the diffraction rods for the substrate and the overlayer are completely independent each other. However, when the misfit is a rational number, $\frac{a_j-a_j^{surf}}{a_j}=\frac{m_j}{n_j+m_j}$ (j=1,2), a moiré patter is often observed with the overlayer atoms periodically displaced within a $(n_1\times n_2)$ supercell. An example will be given in the STM image of Fig. 35 for the growth of a CoO layer on Pt(111). Then the surface cell will gives strong rods at $(h\frac{n_1+m_1}{n_1}, k\frac{n_2+m_2}{n_2})$, but also contributions at each other $(\frac{h}{n_1},\frac{k}{n_2})$, including hence the CTRs, with an intensity which will depend on the Fourier transform of the periodic displacement of the overlayer atomic positions in the supercell with respect to a constant interatomic distance.

The interface stress can also induce elastic displacements in the substrate which are governed by the Hooke's law. The atomic displacements for a $(n_1\times n_2)$ superstructure are

39 J. W. Matthews, *Epitaxial Growth*, Academic, New York (1975), Chap. 8.

given by:

$$\vec{r} - \vec{r}\,^{\circ} = \sum_{Q_1, Q_2} u(\vec{Q}) e^{i(Q_1 a_1 + Q_2 a_2)} \quad , \tag{2.19}$$

where the sum is over the Fourier series with $Q_1 = \frac{2\pi}{a_1}\frac{h}{n_1}$, $Q_2 = \frac{2\pi}{a_2}\frac{k}{n_2}$, and the amplitudes of the displacements $\vec{u}(\vec{Q})$ are function of the elastic constant of the substrate. Then, the strained region of the substrate close to the interface will give contributions to the scattering amplitude of the superstructure reflections which will depend on the corresponding Fourier component of the displacements.[40]

The role of stress is crucial in understanding the origin of self-organized nanostructures and x-ray diffraction helped to elucidate the strain field in some of them like is the case of CuO stripes on Cu(110) surface[41] and of the rows of squared domains formed by adsorption of nitrogen on Cu(100).[42] A quantitative study of strains at the interface requires however well ordered interfaces.

The misfit vernier accommodation mode at the interface that is behind the eq. (2.18) is often not adequate to describe the epitaxial growth of an ultrathin film. In several cases a deposited film starts growing pseudomorphic. Then above a critical thickness the transition from coherency to incoherency happens with the appearance of dislocations which accommodate a part of the misfit,[43] like schematically shown in Fig. 7. At some sites the film is however in registry with the substrate and therefore the Fourier transform of the film electronic density gives some contribution to the CTR intensity.[44]

40 G. Prevot, A. Coati, B. Croset and Y. Garreau, J. Appl. Cryst. **40**, 874 (2007).
41 G. Prevot, B. Croset, Y. Girard, A. Coati, Y. Garreau, M. Hohage, L. D. Sun, P. Zeppenfeld, Surface Science **549**, 52 (2004)
42 B. Croset, Y. Girard, G. Prévot, M. Sotto, Y. Garreau, R. Pinchaux and M. Sauvage-Simkin, Phys. Rev. Lett. **88**, 056103 (2002)
43 Jan H. van der Merwe and W. A. Jesser, J. Appl. Phys. **64**, 4968 (1988)
44 G. Renaud, O. Robach, A. Barbier, Faraday Discuss. **114**, 157 (1999).

2.2. Surface x-ray diffraction experimental set-up

The SXRD experiments discussed in this manuscript were performed at the BM32 (CRG-IF) beamline at ESRF. The photo of Fig. 8 shows the experimental station.

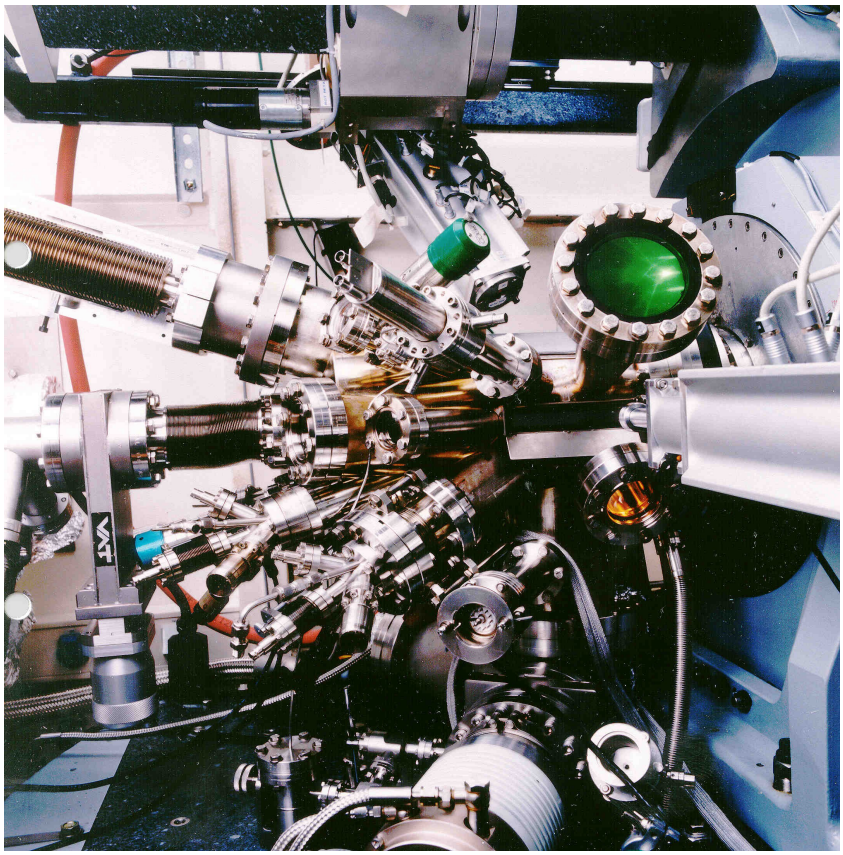

FIG. 8. SXRD dedicated experimental set-up at BM32.

It consists of an ultrahigh vacuum chamber, fully equipped for sample preparation, mounted on a *Z*-axis diffractometer. A complete description of the original set-up is given in ref.[45]. The diffractometer axes are sketched in Fig. 9. The sample is in the vertical position. α is the polar angle of incidence of the x-ray beam. The table α supports two concentric rotary tables ω and δ with their axis parallel to *Z*: ω defines the azimuthal angle of incidence and δ the in-plane scattering angle. The detector arm, supports a movable system which allows for the emergence polar angle of the diffracted beam γ. The γ angle is actually achieved by a combination of two movements: a translation along the detector arm is synchronized with a rotation so as to point to the homocenter; the only drawback is that the detector changes its distance to the sample during a γ scan, and hence the angular acceptance of the detector slits decreases increasing the angle: $\Delta\gamma_s = \cos\gamma\,\Delta\gamma_0$. Two further axis χ_1 and χ_2 allows the alignment of the surface normal $\hat{n}$ parallel to *Z*.

45 R. Baudoing-Savois, G. Renaud, M. De Santis, M.C. Saint-Lager, P. Dolle, O. Geaymond, P. Taunier, P. Jeantet, J.P. Roux, A. Barbier, O. Robach, O. Ulrich, A. Mougin, G. Berard, Nuclear Instruments and Methods in Physics Research B 149 (1999) 213-227

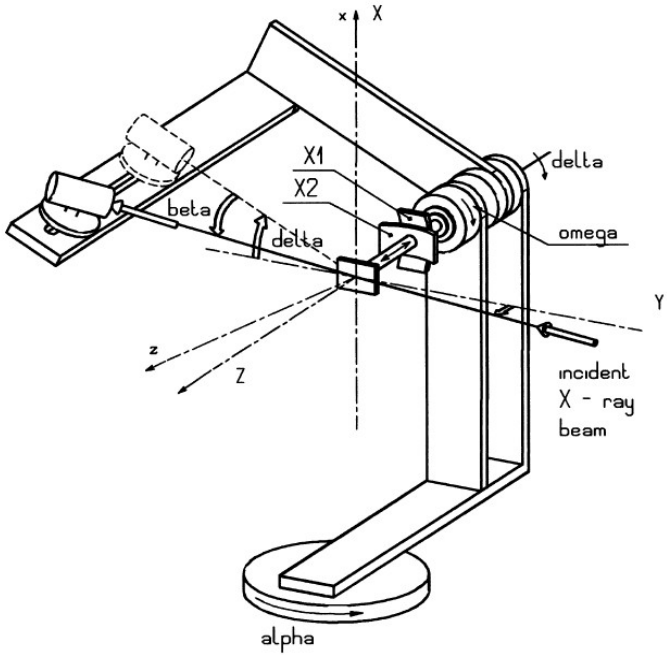

FIG. 9. Schema of the *Z*-axis diffractometer (taken from ref.45)

2.3. Angular settings of the *Z*-axis diffractometer

The angular settings of the diffractometer allows to measure the intensity $I(\vec{Q})$ at a well defined $\vec{Q}=\vec{K}_f-\vec{K}_i$, as shown be the Edwald construction of Fig. 10.

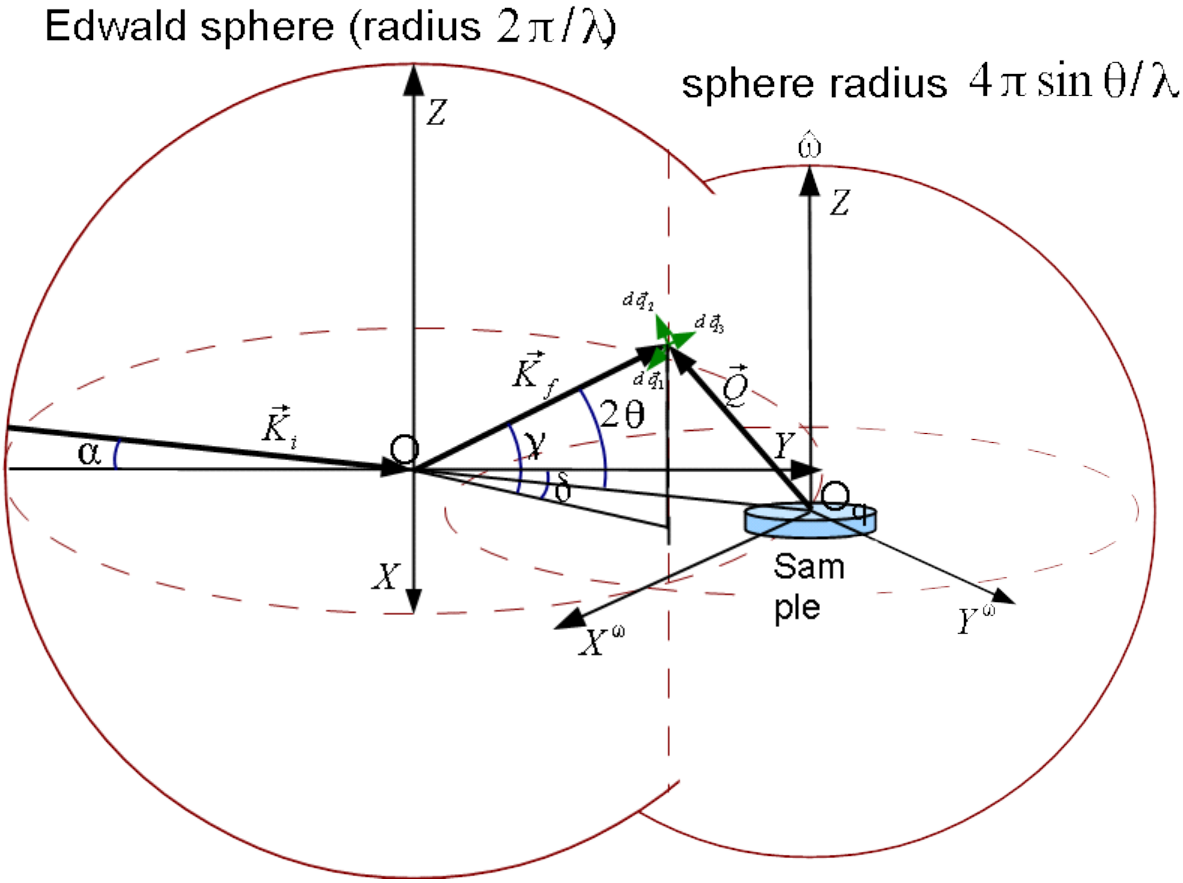

FIG. 10. Edwald construction.

We write the scattering vector $\vec{Q}$ in a Cartesian coordinate frame $X^{\omega}Y^{\omega}Z$ attached to the crystal reciprocal lattice. To find the related diffractometer settings, we need to write the incoming and outgoing wave vector is the same frame. We defines the rotation matrices:

$$A=\begin{pmatrix}1 & 0 & 0\\ 0 & \cos\alpha & -\sin\alpha\\ 0 & \sin\alpha & \cos\alpha\end{pmatrix} \quad , \quad \Delta=\begin{pmatrix}\cos\delta & \sin\delta & 0\\ -\sin\delta & \cos\delta & 0\\ 0 & 0 & 1\end{pmatrix} \quad , \quad \Gamma=\begin{pmatrix}1 & 0 & 0\\ 0 & \cos\gamma & -\sin\gamma\\ 0 & \sin\gamma & \cos\gamma\end{pmatrix} \quad ,$$

$$\Omega=\begin{pmatrix}\cos\omega & \sin\omega & 0\\ -\sin\omega & \cos\omega & 0\\ 0 & 0 & 1\end{pmatrix} \quad , \qquad (2.20)$$

which allow the transformation from the lab frame *xyz* to the frame $X^{\omega}Y^{\omega}Z$ attached to the circle ω (see Fig. 9) : $\vec{K_{i,\omega}}=\Omega^{-1}A^{-1}\vec{K_{i,lab.}}$ and $\vec{K_{f,\omega}}=\Omega^{-1}\Delta\Gamma\vec{K_{i,lab.}}$ (see Fig. 10).
Then the scattering equation writes:

$$\vec{Q}_{\omega}\equiv\begin{pmatrix}Q_{X^{\omega}}\\ Q_{Y^{\omega}}\\ Q_{Z}\end{pmatrix}=\Omega^{-1}\left(\Delta\Gamma-A^{-1}\right)\vec{K_{i,lab.}} \quad . \qquad (2.21)$$

Lets neglect the crystal miscut. Then we can take $\vec{b}_3\|\hat{n}\|\hat{Z}$. In the most relevant cases, like for low index faces of cubic crystals, $\vec{b}_1$ and $\vec{b}_2$ can be chosen in the surface plane. Taking $\vec{b}_1\|X^{\omega}$, and $\vec{K_{i,lab.}}$ along *y* in the laboratory frame, eq. (2.21) writes (see eq. 31 in ref. [46, 47]):

$$\begin{pmatrix}b_1 & b_2\cos\beta_3 & 0\\ 0 & b_2\sin\beta_3 & 0\\ 0 & 0 & \dfrac{2\pi}{a_3}\end{pmatrix}\begin{pmatrix}h\\ k\\ l\end{pmatrix}=\frac{2\pi}{\lambda}\begin{pmatrix}\cos\omega\sin\delta\cos\gamma-\sin\omega\left(\cos\delta\cos\gamma-\cos\alpha\right)\\ \sin\omega\sin\delta\cos\gamma+\cos\omega\left(\cos\delta\cos\gamma-\cos\alpha\right)\\ \sin\gamma+\sin\alpha\end{pmatrix} \qquad (2.22)$$

We have three equations and four degrees of freedom, and the extra condition of fixed grazing incidence is usually chosen to find all the angles corresponding to a given accessible l on a $(h\ k)$ rod, except for the specular reflectivity one where it must be $\delta=0$ and $\alpha=\gamma$ (and ω arbitrary).

2.4. Measurements of the rod intensities.

A detector placed on the diffractometer arm integrates the scattering cross section given by (2.5) over the solid angle $d\Omega$, which is defined by the detector slits for 0D NaI counters or by the pixels included in the region of interest in 2D ccd detectors. The atomic structure of ultrathin films and of 2D surface layers is solved through a fit of the

46 M. Lohmeier and E. Vlieg, J. Appl. Cryst. **26**, 706 (1993).
47 Note that in the reference there is printing mistake in the first line of the second term vector.

experimental structure factor amplitudes $|F(h,k,l)|$ with the expression given by Eq. (2.16). To get these amplitudes, several geometric correction factors [48] need to by applied to the measured intensities.

a) Polarization factor.

The first correction factor is the classical angular dependence in the dipole scattering [the $\sin^2\theta$ term in (2.3)]. Remembering that on BM32 the electric field is along the laboratory *z* axis it is easy, using the matrices (2.20), to find :

$$C_{pol} = 1 - (\sin\alpha\cos\delta\cos\gamma + \cos\alpha\sin\gamma)^2$$

b) Lorentz correction

In a single crystal diffraction experiment, the aim is to measure the intensity of a given (*hkl*) reflection. This requires an integration in reciprocal space over a region large enough to include all the coherent scattering originating from (*hkl*) planes, which will depend on the crystal quality. This integral is proportional to the structure factor modulus square:[32]

$$|F_{hkl}|^2 \propto \int I(Q_X, Q_Y, Q_Z)\, dQ_X\, dQ_Y\, dQ_Z \qquad (2.23)$$

where $I(Q_X, Q_Y, Q_Z)$ is the background-subtracted intensity distribution.

The diffractometer is set to put the desired reflection on the Edwald sphere surface, at the point where the detector is placed (Fig. 10). Then a scan is performed in such a way that the (*hkl)* node cross completely the sphere surface. For a given scan type, the time a reflection needs to pass through the Edwald sphere is function of the reflection itself. The inverse of the correction factor which has to be applied to the measured integrated intensities to obtain the squared structure amplitudes is called the Lorentz factor *L*.[49,50] It is calculated operating a change of variable in (2.23) from the reciprocal space Q_i to the real motor variables M_j, which are scanned with a constant step. The Lorentz factor is the inverse of the determinant of the Jacobian matrix $J_{ij} = \partial Q_i / \partial M_j$. *L* is easily calculated for the *Z*-axis diffractometer geometry. A first change of variable is operated to a local Cartesian coordinate system with origin at the point (*hkl)*, and with the axes $\vec{q}_1$ and $\vec{q}_2$ defining a plane that is tangent to the Edwald sphere. The third axis $\vec{q}_3$ is parallel to $\vec{K}_f$. Then the integration $I_{1,2}(q_3) = \int I(q_1, q_2, q_3)\, dq_1\, dq_2$ over the first two independent variables is operated directly by the counting detector or by a x-ray CCD detector, providing that the detector slits are wide enough. The third integral is operated by rotating the sample around the $\hat{\omega}$ axis, and the structure factor modulus square is:

$$|F_{hkl}|^2 \propto \int I_{1,2}(\omega) \frac{dq_3}{d\omega} d\omega \quad . \qquad (2.24)$$

The scattering vector increment during the rotation is given by $d\vec{Q} = \hat{\omega} \wedge \vec{Q}\, d\omega$ and its component along $\vec{q}_3$ is $dq_3 = \hat{q}_3 * \hat{\omega} \wedge \vec{Q}\, d\omega$. It is easy to obtain from Fig. 10:

48 E. Vlieg, J. Appl. Cryst. (1997). 30, 532-543
49 Azaroff, L. V. (1968), Elements of X-ray Crystallography, New York, McGraw-Hill.
50 G. J. McIntyre and R. F. D. Stansfield, Acta Cryst. **A44**, 257 (1988).

$\hat{q}_3=(\cos\gamma\sin\delta,\cos\gamma\cos\delta,\sin\gamma)$; $\hat{\omega}=(0,0,1)$;

$\vec{Q}=\frac{2\pi}{\lambda}(\cos\gamma\sin\delta,\cos\gamma\cos\delta-\cos\alpha,\sin\gamma+\sin\alpha)$.

Hence the expression for the Lorentz correction is: $L=1/(\hat{q}_3*\hat{\omega}\wedge\vec{Q})=1/(\cos\gamma\sin\delta\cos\alpha)$ (taking just the angular dependent factor).

c) Lorentz correction in SXRD and rod intercept correction

We have seen that the diffraction feature of a periodic surface structure consists in rods with an intensity distribution very sharp parallel to the surface, and which is a continuous functions of Q_z. Then, to solve the surface structure, a measurement of the intensity distribution

$$I_{h,k}(Q_Z)=\int I(Q_X,Q_Y,Q_Z)dQ_X\,dQ_Y\propto|F(h,k,l)|^2$$

is needed, where now $|F(h,k,l)|$ is a continuous function of l. The measurement is performed like for single crystals, i.e. the diffractometer is positioned with the detector at the (*hkl*) position in the reciprocal space and then an ω scan is performed. This results in the integration of the rod over the interval ΔQ_Z , which is the portion of the rod that crosses, during the scan, the Edwald sphere surface region delimited by the detector slits. If $I_{h,k}(Q_Z)$ is about constant in this interval,

$$\int I_{h,k}(\omega)\,d\omega\simeq I_{h,k}(Q_Z)\times L\times\Delta Q_Z \quad .$$

This is quite a good approximation for reasonable slit settings, except close to Bragg peaks.

For small polar angles of the scattered beam, the integration region is defined by the detector slits opening *HG6*, which is horizontal when all angles are set to zero. The angular acceptance is given by $\Delta\gamma_s=\frac{HG6}{D_{Detector}}$, where $D_{detector}$ is the sample-detector distance. The rod is then integrated over:

$$\Delta Q_Z=\frac{2\pi}{\lambda}\cos\gamma\,\Delta\gamma_s \quad \text{[see Fig. 11(a)].} \qquad (2.25)$$

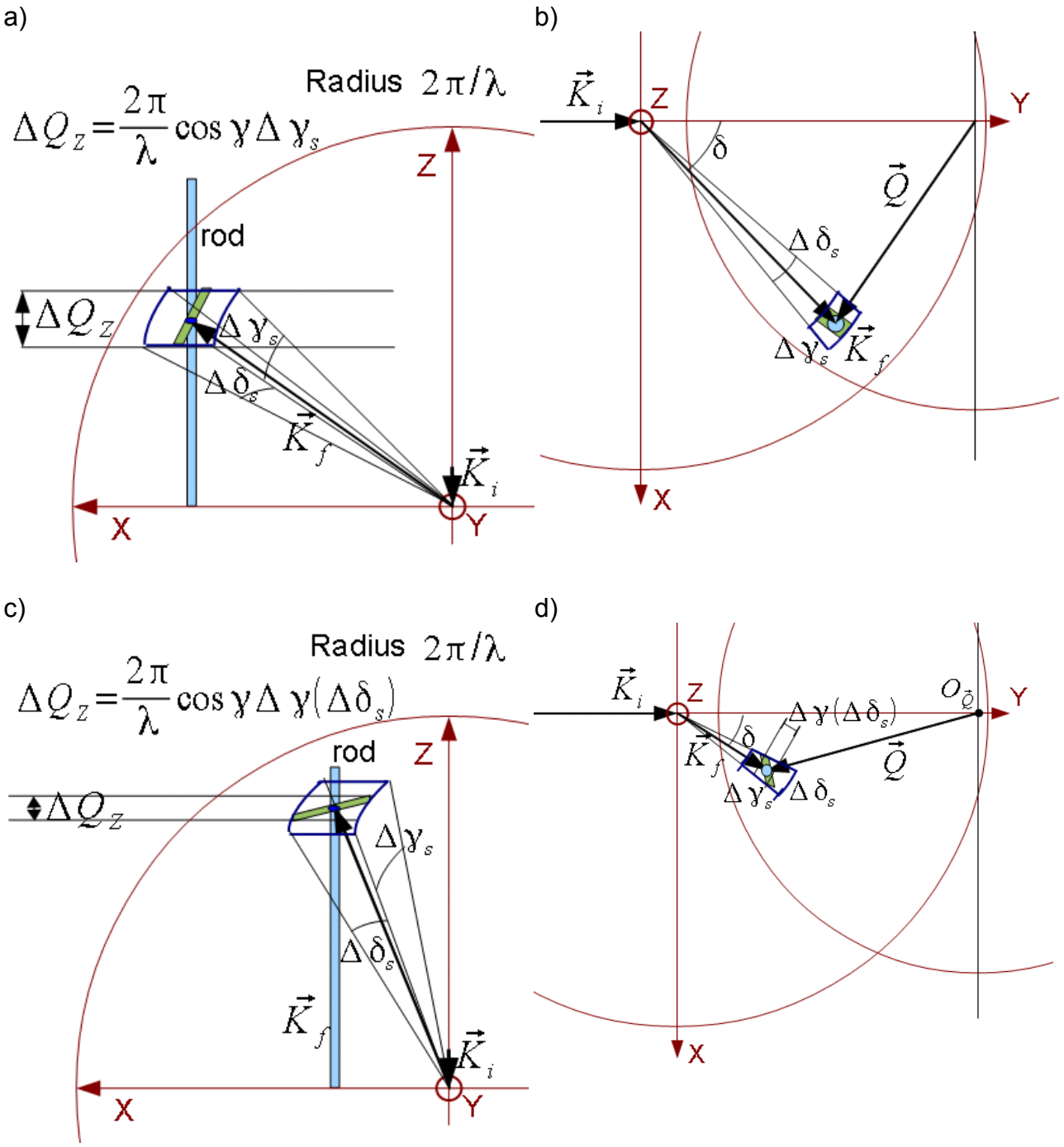

FIG. 11 (a), (c): schematic view along the Y axis of the trajectory (green) of the diffraction rod (blue) on the surface of the Edwald sphere during an ω scan at low and high γ, respectively. The detector acceptance ($\Delta\delta_s$, $\Delta\gamma_s$) is shown. (b), (d): Projection in the surface plane of case (a) and (c), respectively.

which gives the standard “rod intercept” correction for the *Z*-axis diffractometer:

$$C_{rod} = \cos\gamma \quad . \qquad (2.26)$$

This correction can be not valid for large γ values. It is easy to calculate from eq. (2.22) how the interception of the (*hk*) rod with the Edwald sphere surface moves during the ω scan. This curve is described by the equation:

$\delta = \arccos\left(\frac{\cos\delta_\circ}{\cos\gamma} - \frac{1-\cos^2\gamma}{2\cos\alpha\cos\gamma}\right)$, ($\delta_\circ = \delta(\gamma=0)$) .

The change in δ increases with γ (in particular for small δ values):

$$\Delta\delta = \frac{\sin\gamma}{\sin\delta}\left(\frac{1}{\cos\alpha} - \frac{\cos\delta}{\cos\gamma}\right)\Delta\gamma \simeq \frac{\sin\gamma}{\sin\delta}\left(1 - \frac{\cos\delta}{\cos\gamma}\right)\Delta\gamma \qquad (2.27)$$

Depending on the angular settings, the integration interval ΔQ_Z can be delimited by the opening of the vertical detector slits *VG6*, which define the angular acceptance $\Delta\delta_s = \frac{VG6}{D_{detector}\cos\gamma}$. The integration interval is then obtained replacing in (2.25) the $\Delta\gamma(\Delta\delta_s)$ value calculated from (2.27). In practical C_{rod} needs to be multiplied by the additional factor:

$$C_{Corr} = \frac{VG6}{HG6}\frac{1}{\cos\gamma\frac{\sin\gamma}{\sin\delta}\left(1-\frac{\cos\delta}{\cos\gamma}\right)} ,$$

when this is smaller than the unity.

Fig 11(a) [11(c)] shows a schematic view along the Y axis, forming the angle α with the incidence beam, of the trajectory of a diffraction rod on the surface of the Edwald sphere during an ω rotation, with respect to the detector acceptance ($\Delta\delta_s$, $\Delta\gamma_s$) at low γ (δ) and high δ (γ) values. Fig. 11(b) [11(d)] shows its projection in the surface plane.

d) Linear γ table correction

On the experimental set-up of BM32 the rotation γ is composed by a translation plus a rotation. The horizontal angular acceptance is then $\Delta\gamma_s = \cos\gamma\frac{HG6}{D^0_{detector}}$, where $D^0_{detector}$ is the sample-detector distance at $\gamma=0$, and the rod integration range is $\Delta Q_Z = \frac{2\pi}{\lambda}\cos\gamma^2\frac{HG6}{D^0_{detector}}$. In this case a further correction factor $C_{table}=\cos\gamma$ is needed.

e) Area correction

The schema of grazing incidence diffraction adopted on BM32 is shown in Fig. 12. As standard values, the sample is a circle of diameter $D_{sample}\sim 10\,mm$ and the incidence angle is $\alpha \leqslant 1°$. Under these conditions, the beam illuminates completely a slice of sample, whose height is defined by the opening of the vertical slits of the incoming beam $VG4$ (or by the beam size) Then the active area is defined by the couple of detector slits $VG5 = VG6$ (typically $2\,mm$ wides) which act as a collimator : $C_{area} = \frac{VG4 * VG6}{\sin\delta}$, except at low angles, where $C_{area} = VG4 * D_{sample}$.

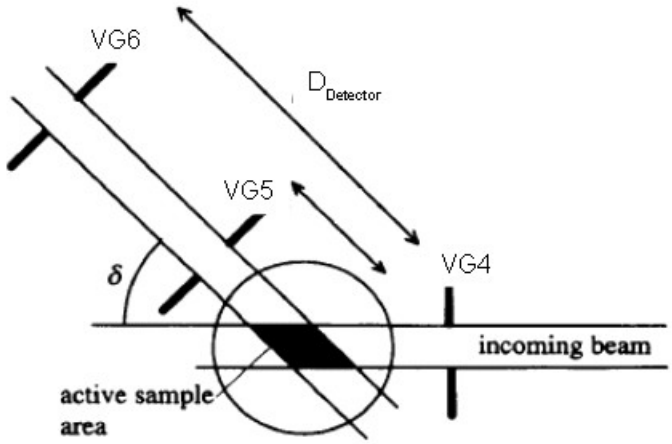

FIG. 12. Schema of active area in surface grazing incidence X-ray diffraction (from ref. 48)

f) Stationary scans

Studying the structure of films of increasing thickness, requires the measurement of the rod at smaller and smaller Δl steps. The rocking scan method of integration becomes very beam time consuming. In such cases the intensity $I_{h,k,l}$ is simply measured scanning along the rod. At each point, the integration is over the Edwald sphere surface region defined by the active detector area, shown as dark blue in Fig. 11. This area is proportional to $C_{rod}^{Stat} = \frac{1}{\sin \gamma}$ (this is called in some papers the Lorentz correction for stationary scans).
The quantitative measurement of intensities by scanning along the rod requires good crystals and a perfect alignment of the rod position.

g) Line shape and detector acceptance correction.

The previous intensity corrections apply to sharp rods. The rod line-shape parallel to the surface can be broadened due the lost of in-plane coherence. A relevant source of broadening is the growth of domains of characteristic size, like happens for example in films of ordered alloys. This broadening affects more strongly the stationary scans. The C_{rod}^{Stat} correction diverges at low γ and its validity is limited to rod size much smaller than the reciprocal space area integrated by the detector, parallel to the sample surface. This area is given by $\Delta Q_1 \times \Delta Q_2$, with $\Delta Q_1 = \frac{2\pi}{\lambda} \sin \gamma \, \Delta \gamma_s$ and $\Delta Q_2 = \frac{2\pi}{\lambda} \cos \gamma \, \Delta \delta_s$ (see Fig. 13). Rocking scans can integrate the intensity over a much wider region. Lets us write the in-plane projection of the slit integrated reciprocal space region in term of transverse (ΔQ_{tr}) and longitudinal (ΔQ_{long}) component with respect to the ω scan. In general a wide enough ω scan can be performed in the transverse direction to integrate properly the rod. The integration range in the longitudinal direction is easily calculated from the matrices (2.20) :

$$\Delta Q_{long} \simeq \frac{2\pi}{\lambda} \frac{\cos \gamma \sin \delta}{\sqrt{1 + \cos^2 \gamma - 2 \cos \gamma \cos \delta}} \Delta \delta_s$$

(in grazing incidence approximation, with $\cos\alpha \simeq 1$).
In general three cases can happen, illustrated in Fig. 13 by the three concentric circles, which represent rods of different width. The inner circle represents a rod which is fully integrated by the detector slits. Any acceptance correction is needed. The intermediate one represent a rod which is properly integrated by a rocking scans, but whose intensity needs to be corrected by a factor C_{Det}^{Stat} in stationary scans. For the large circle a correction C_{Det} is needed also with the rocking scan method. The detector correction represents the fraction of integrated intensity and can be evaluated knowing the normalized intensity distribution function $u(Q_{//}^2)$, whose line-shape can be measured by a high resolution scan parallel to the surface.
Quite important is the Gaussian distribution case. The detector correction is

$$C_{Det}^{Stat} = \iint u(Q_X, Q_Y)\, dQ_X\, dQ_Y = \frac{1}{2\pi\sigma^2} \int_{\frac{-\Delta Q_1}{2}}^{\frac{\Delta Q_1}{2}} dQ_1 \int_{\frac{-\Delta Q_2}{2}}^{\frac{\Delta Q_2}{2}} dQ_2\, \mathrm{e}^{-\frac{Q_1^2+Q_2^2}{2\sigma^2}} = erf\left(\frac{\Delta Q_1}{2\sqrt{2}\sigma}\right) \times erf\left(\frac{\Delta Q_2}{2\sqrt{2}\sigma}\right)$$

and

$$C_{Det} = \iint u(Q_X, Q_Y)\, dQ_X\, dQ_Y = \frac{1}{2\pi\sigma^2} \int_{\frac{-\Delta Q_{long}}{2}}^{\frac{\Delta Q_{long}}{2}} dQ_{long} \int_{-\infty}^{\infty} dQ_{tr}\, \mathrm{e}^{-\frac{Q_{long}^2+Q_{tr}^2}{2\sigma^2}} = erf\left(\frac{\Delta Q_{long}}{2\sqrt{2}\sigma}\right)$$

for stationary and rocking scans, respectively.
A second relevant case which can also be integrated analytically is given by the Lorentzian-like distribution (see ref. [51]):

$$u(Q_X, Q_Y) = \frac{1}{2\pi} \frac{\Gamma/2}{(Q_X^2 + Q_Y^2 + (\Gamma/2)^2)^{3/2}}$$

For stationary scans,

$$C_{Det}^{Stat} = \frac{1}{2\pi} \int_{\frac{-\Delta Q_1}{2}}^{\frac{\Delta Q_1}{2}} dQ_1 \int_{\frac{-\Delta Q_2}{2}}^{\frac{\Delta Q_2}{2}} dQ_2 \frac{\Gamma/2}{(Q_1^2 + Q_1^2 + (\Gamma/2)^2)^{3/2}} = \frac{1}{\pi} \int_{\frac{-\Delta Q_1}{2}}^{\frac{\Delta Q_1}{2}} dQ_1 \frac{\Gamma/2}{(Q_1^2 + (\Gamma/2)^2)\left(1 + \frac{Q_1^2 + (\Gamma/2)^2}{(\Delta Q_2/2)^2}\right)^{1/2}}$$

and, when $\Gamma \ll \Delta Q_2$

$$C_{Det}^{Stat} \simeq \frac{1}{\pi} \int_{\frac{-\Delta Q_1}{2}}^{\frac{\Delta Q_1}{2}} dQ_1 \frac{\Gamma/2}{(Q_1^2 + (\Gamma/2)^2)} = \frac{2}{\pi} \arctan \frac{\Delta Q_1}{\Gamma} \quad .$$

Analogously, for rocking scans :

$$C_{Det} = \frac{1}{\pi} \int_{\frac{-\Delta Q_{long}}{2}}^{\frac{\Delta Q_{long}}{2}} dQ_{long} \frac{\Gamma/2}{(Q_{long}^2 + (\Gamma/2)^2)} = \frac{2}{\pi} \arctan \frac{\Delta Q_{long}}{\Gamma} \qquad (2.28)$$

51 E. Vlieg, J. F. Van des Veen, S. J. Gurman, C. Norris, J. E. Macdonald, Surface Science 210 (1989) 301-321

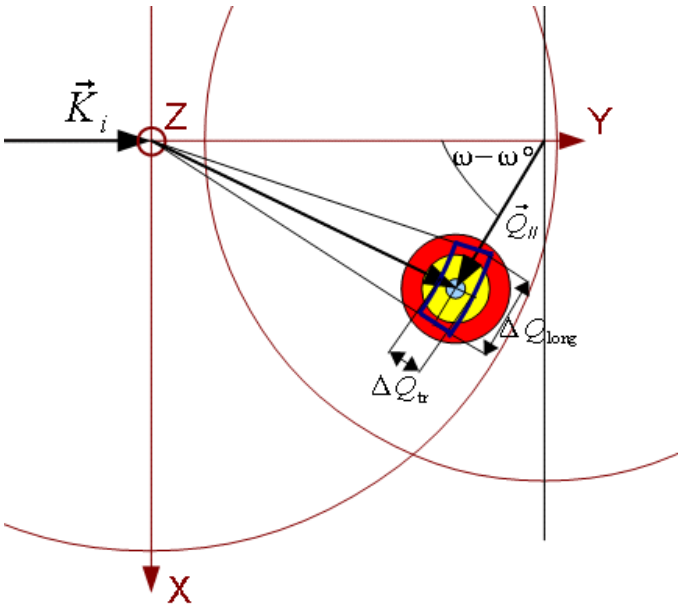

FIG. 13. Comparison within transverse rod width and in-plane detector acceptance. The blue rod is completely integrated also with a stationary measurement. The yellow one can be integrated with a rocking scan. The red one needs in any case a correction for the detector acceptance.

In these two simple cases the rod line-shape has a cylindrical symmetry around the center of the rod. However the line-shape can also be very anisotropic, like for example for the CdTe(001)-c(2×2) reconstruction.[52] These more complicated situations are discussed in ref. [53]. Mosaicity is an other important source of anisotropy, which can be quite relevant for metallic substrates.. When the substrate structure consists of slightly in-plane rotated domains, the integrated intensity is properly recovered with rocking scans. For stationary scans, the dispersion in the reciprocal space given by the in plane mosaicity $\Delta\omega_M$ should be small compared to the detector integration interval. In grazing incidence this condition is expressed by the inequality $\Delta\omega_M < \frac{\sin\gamma}{\sin\delta}\Delta\gamma_s$ (for $\Delta\delta_s$ wide enough).

h) Total correction factor

The total correction to apply at the intensity measured by rocking the sample azimuth to obtain the structure factor is given by the relationship :

$$|F(h,k,l)|^2 \propto \frac{\int I_{h,k}(\omega)\,d\omega}{L \times C_{rod} \times C_{pol} \times C_{area} \times C_{Table} \times C_{Det}} \qquad (2.29)$$

For stationary scans, we have:

$$|F(h,k,l)|^2 \propto \frac{I_{h,k,l}}{C_{rod}^{Stat.} \times C_{pol} \times C_{area} \times C_{Det}^{Stat}} \qquad (2.30)$$

52 M. B. Veron, V. H. Etgens, M. Sauvage-Simkin, S. Tatarenko, B. Daudin, D. Brun-Le Cunff, J. Cryst. Growth 159 (1996) 694-702.

53 O. Robach, Y. Garreau, K. Aïd, M. B. Véron-Jolliot, J. Appl. Cryst. 33 (2000) 1006-1018

3. MnPt and MnNi alloys

Chemically ordered Mn alloys have been extensively investigated because they exhibit a hight T_N. *In-situ* x-ray diffraction helps in growing epitaxial films with the desired structural properties and with improved chemical order. The first structure discussed here will be a MnNi surface alloy on top of Ni(110). This example allows to develop concepts which will be used for the study of MnPt surfaces and ultrathin films grown on Pt single crystals. Here more emphasis will be putted on the first stages of growth, the structure of the ultrathin films having been the subject of a PhD thesis in our group.[54]

3.1. Bulk atomic and magnetic structure

The Mn-Pt phase diagram shows below ~900°C three ordered phases of composition $MnPt_3$, MnPt and Mn_3Pt.[55] The Pt-rich and Mn-rich phases are both of $L1_2$-type (≡γ' phase) and are respectively FM (T_c= 390 K, Mn magnetic moment ~3.6 μ_B[56]) and AFM (T_N= 475 K[57]). The equiatomic ordered phase is of $L1_0$(≡CuAu I)-type, i.e. is a face centered tetragonal structure with pure Pt and Mn plane which alternate along the *c* axis. It is the most interesting for applications having a Néel temperature of 970 K. Its allowed spin configurations were discussed by Krén *et al.*[58] (see Fig. 14).

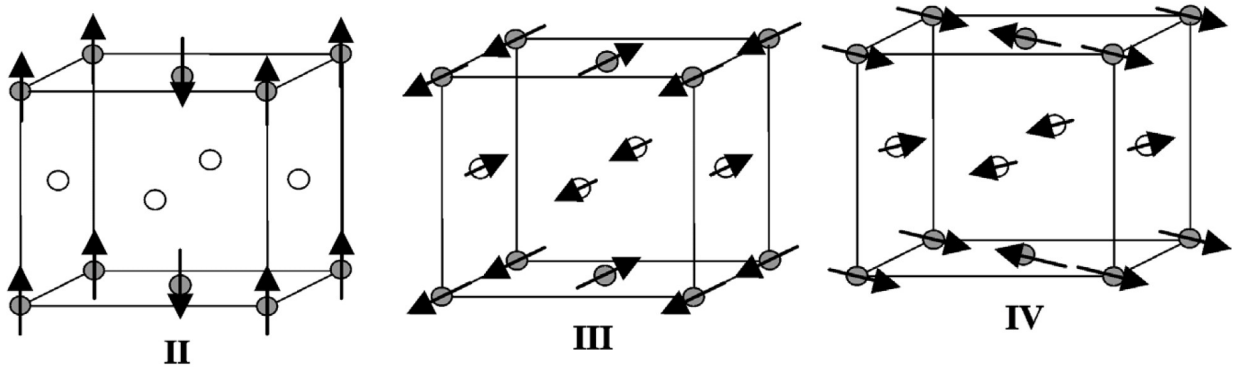

FIG. 14. Proposed spin structures of *L*10-type MnPt alloys in the vicinity of the equiatomic composition[58] (taken from ref. [59]).

Experimentally the phase diagram is quite complex. Both the type II and type III (or IV) magnetic order (see Fig. 15) have been found as function of the exact composition.[58,60] Note that the neutron diffraction experiments cannot distinguish between type III and IV order. A transition between type II and type III was also observed for the nominal MnPt stoichiometry as function of the temperature.

Theoretical calculation for MnPt bring out that the direction of the Mn magnetic moment

54 Marcio M. Soares, Université de Grenoble, (2011)
55 T. B. Massalski, *Binary Alloy Phase Diagrams*, 2nd ed., ASM International, Materials Park, Ohio, 1993.
56 B. Antonini, F. Lucari, F. Menzinger, A. Paoletti, Phys. Rev. **187**, 611 (1969)
57 T. Ikeda, Y. Tsunoda, J. Mag. Mag. Mat. 272-276 (2004) 482-484
58 E. Krén, G. Kadar, L. Pal, J. Solyom, P. Szabo, T. Tarnoczi, Phys. Rev. 171, 574 (1968)
59 K. Fukamichi, R. Y. Umetsu, A. Sakuma, C. Mitsumata, "Magnetic and electrical properties of practical antiferromagnetic mn alloys", Handbook of Magnetic Materials, ed. K.H.J. Buschow, Elsevier (2006)
60 H. Hama, R. Motomura, T. Shinozaki, Y. Tsunoda, J. Phys.: Condens. Matter **19** (2007) 176228

is parallel to the c-axis (type-II order),[61] in contrast to $L1_0$ MnNi equiatomic alloy in which the magnetic moments of Mn lie in the (001) plane.

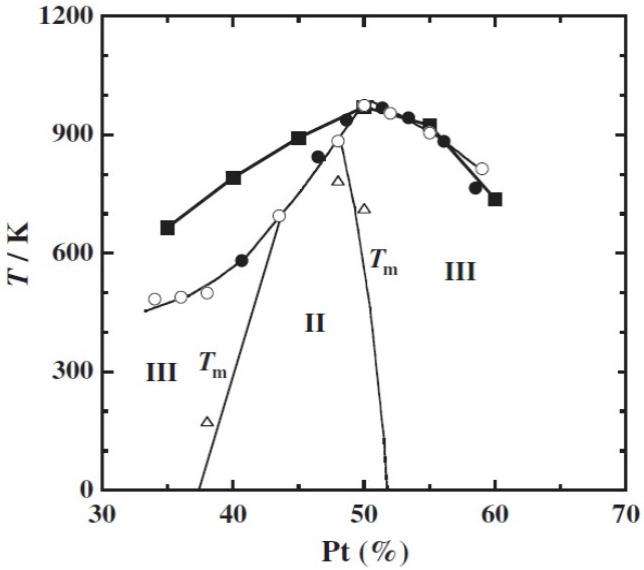

FIG. 15 The magnetic phase diagram of the $L1_0$-type MnPt ordered alloy system obtained by Krén *et al.*[58] (○ and Δ), together with recent experimental (●) and theoretical (■) results by Umetsu *et al.*[61] (taken from ref. 61).

3.2. ultrathin films

In future sensors, the total spin valve thickness must significantly decrease, and the AFM film is by far the thickest layer. However, high exchange bias and thermal stability are difficult to maintain when reducing the thickness. A decreasing with thickness of the exchange coupling is expected as a result of the finite-size scaling of the Néel temperature.[62] Exchange coupling disappears in sputtering-grown spin valves when the MnPt AFM layer is less than 6 nm.[63] However this lack of exchange coupling is mainly related to the film structure.[64] Although the MnPt ordered phase is stable in bulk, thin films obtained by sputtering grown in the disordered γ phase, which is paramagnetic at room temperature. Further studies on thick films have confirmed the close relationship between the degree of chemical order and exchange coupling.[65]

The control of the chemical order in ultrathin films is therefore crucial for applications requiring the exchange bias. The films discussed in this chapter are grown by molecular beam epitaxy, under given conditions they exhibit chemical order and they give an important input to the understanding of the link between exchange coupling and tetragonal phase.

3.3. Chemical order

Lets consider epitaxial ultrathin alloy films grown either by MBE deposition of a pure metal *A* on the substrate *B,* followed by annealing, or by co-deposition. In both cases the

61 R. Y. Umetsu, K. Fukamichi, A. Sakuma, Materials Transactions, Vol. 47, No. 1 (2006), 2-10
62 T. Ambrose, C. L. Chen, Phys. Rev. Lett. 76, 1743 (1996)
63 M. Rickart, A. Guedes, B. Negulescu, J. Ventura, J. B. Sousa, P. Diaz, M. MacKenzie, J. N. Chapman, P. P. Freitas, Eur. Phys. J. B **45**, 207–212 (2005)
64 M. F. Toney, M. G. Samant, T. Lin, D. Mauri, Appl. Phys. Lett. 81, 4565 (2002)
65 C. H. Lee, J. H. Lai, Y.-F. Wu, J. C. A. Huang, J. Magn. Magn. Mat., 303, e156 (2006)

substrate temperature play a crucial role in the establishment of chemically ordered phases. The degree of order is governed by the free energy of the system and by non-equilibrium processes, which are difficult to control. Segregation at the surface of one kind of atoms and diffusion in the substrate are key phenomena. For codeposited alloys, the stoichiometry is mainly determined by the real evaporation rate of each element. As a result, the degree of chemical order of a surface alloy is in general weaker than for bulk. Moreover, the ordering during the growth starts at a large number of equivalent sites at the substrate-film interface. This bring to antiphase domains.

a) Order parameter

Lets us consider a binary alloy formed by *A* and *B* atoms type, and with two different atomic sites, designed as α- and β-sites. In the ideal ordered phase *A* (*B*) atoms occupy α (β) sites. The order parameter *S* is then defined by $S=r_\alpha - w_\beta$, where r_α and w_β are, respectively, the fraction of α- and β-sites occupied by *A* atoms. It is easy to see that $S \leq 1$, and it is maximum for stoichiometric composition and perfect long-range order.

The intensity of superstructure reflections is directly related to the order parameter. For CuAu I type ordered alloy:[66]

$h+k$ unmixed; $F_u(h,k,l)=4(x_{Au}f_{Au}+x_{Cu}f_{Cu})$ (fundamental reflections) ,

were x_i is the fraction of atom-type *i,*

$h+k$ =even, $k+l$ = odd; $F_u(h,k,l)=2\mathrm{S}(f_{Au}-f_{Cu})$ (superstructure reflections).

Therefore both the exact stoichiometry and the degree of order have a strong influence on the superstructure reflections intensity.

b) Antiphase domains

Fig. 16 Shows a top view of the *c*(2×2) surface alloy structure obtained by deposition of 0.5 Mn ML on Ni(110), which will be discussed in the next paragraph. The dashed line represents an antiphase domain boundary between two regions. The structure factor of Ni(110)-*c*(2×2)Mn unit cell is given by:

$$F_u(h,k)=f_{\mathrm{Ni}}(1+\exp(i\pi(h+k)))+f_{Mn}(\exp(i\pi h)+\exp(i\pi k)) \quad .$$

Crossing an antiphase domain boundary, it is multiplied by a phase factor $\exp(i\pi h)$. The reflection line-shape can be calculated using the same method discussed in ref. 66 , paragraph 12.3. The scattered intensity around (2m+1,2n+1) superstructure reflections is proportional to

$$|S(\vec{Q})|^2=|F_u(h,k)|^2\frac{N_1 a_1 \gamma_1}{2\pi(\gamma_1^2+(\Delta\vec{Q}\vec{a}_1/2)^2)}\frac{N_1 a_2 \gamma_2}{2\pi(\gamma_2^2+(\Delta\vec{Q}\vec{a}_2/2)^2)} \qquad (3.1)$$

where γ_1 (γ_2) is the probability to cross a domain boundary shifting by the lattice vector $\vec{a}_1$ ($\vec{a}_2$). This expression is valid for small γ_i , assuming that the probability of

66 B. E. Warren, *x-ray diffraction*, Dover publications, New York (1990) chap. 12.

an antiphase boundary between any of two neighboring cell is the same, and neglecting the correlation between the two orthogonal directions. The lineshape is Lorentzian, with a full width at half maximum of $4\gamma_i/a_i$. In this approximation antiphase domains affect the line-shape of the superstructure diffraction rods but not the integrated intensity. However at the boundaries sites can be occupies by the wrong kind of atoms, which decreases the intensity also.

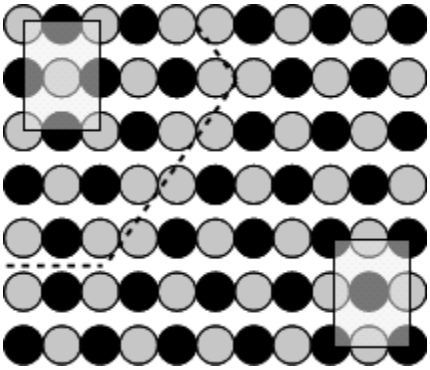

FIG. 16 Antiphase domain boundary (dashed line) in a c(2×2) surface alloy grown pseudomorphic on a fcc(110) substrate.

c) Domains in MnPt films

Figure 17 shows an antiphase domain boundary between two ordered MnPt $L1_0$ grains, obtained by shifting the left side by $(\frac{\vec{a}_1+\vec{a}_3}{2})$. These walls cost quite a low energy because atoms at the boundary (*B* site in the figure) have the same nearest-neighbors (4 of the same kind and 8 of the other) as atoms in bulk (*A*). Only distances are slightly different due to the tetragonal distortion. An equivalent boundary is created shifting a grain by $(\frac{\vec{a}_2+\vec{a}_3}{2})$. This are the only two kind of antiphase domains expected in $L1_0$ ultrathin ordered films.

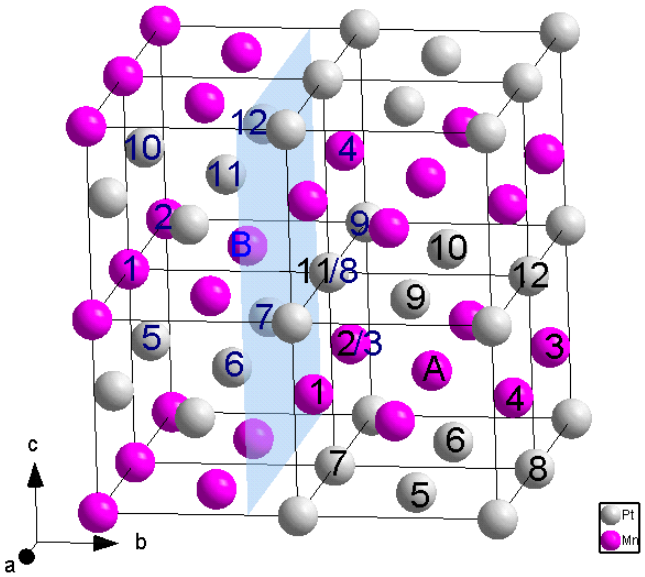

FIG. 17. Domain wall in MnPt $L1_0$. The number and kind of nearest-neighbors at the interface is the same as

in volume.

For epitaxial films, the scattered amplitude is given by eq. (2.18). Then the diffracted intensity will contain a sharp and a diffuse component. The situation is similar to the case of reconstructed domains on surface described by Vlieg *et al.*[51] If the different domains are equally occupied the "macroscopic" order parameter, measured on the film region which scatters coherently, is zero. The contribution of the film to the sharp component of the rod is that one of a disordered alloy. The chemical order give only a diffuse component, which can be calculated as in ref. 66 , assuming as additional hypothesis that the film thickness is constant:

$$|S(\vec{Q})|^2=|F_u(h,k,Q_z)|^2\frac{N_1 a_1 \gamma_1}{2\pi(\gamma_1^2+(\Delta\vec{Q}\vec{a}_1/2)^2)}\frac{N_1 a_2 \gamma_2}{2\pi(\gamma_2^2+(\Delta\vec{Q}\vec{a}_2/2)^2)}\frac{\sin^2 N_3\vec{Q}\vec{a}_3/2}{\sin^2\vec{Q}\vec{a}_3/2} \quad (3.2)$$

with $h+k$ =even, $k+l$ = odd.

3.4. 2D Mn surface alloys

Ultrathin film magnetism has brought important contributions to our fundamental understanding of the physics of magnetism. An important criterion about the existence of a magnetic moment in the case of delocalized electrons is due to Stoner.[67] It states that ferromagnetism is expected when $J\times n^\circ(e_F)>1$, where J is the exchange integral and $n^\circ(e_F)$ is the density of state at the Fermi level. At the surface of a single crystal, the atoms located in the topmost layer have a reduced number of nearest-neighbors, which means a narrower bandwidth. The Stoner criterion is then more easily fulfilled. More in general a detailed knowledge of the atomic structure allows the calculation of the magnetic properties of ultrathin metallic films. In this section the structure of 2D surface alloys obtained by deposition of 0.5 ML of Mn on the clean Ni(110) and Pt(110) substrates will be discussed.

a) Structure of Ni(110)-*c*(2×2)Mn (revisited)

Deposition of 0.5 Mn ML on Ni(110) results in a *c*(2×2) surface alloy[68], whose structure was resolved by SXRD. The details of this study are reported in ref.[69]

It was found by measuring superstructure reflections during the growth that their intensity is maximum after evaporation of about 0.5 Mn ML. The *c*(2×2) order establishes only for a Mn coverage ≥ 0.3 ML, over a large range of substrate temperatures (Fig. 18). The size of chemically ordered domains increases with the substrate temperature up to the limit of stability of this phase ($T_{max.}$≥ 440 K), as shown by the line shape of superstructure reflections (Fig. 19). A Lorentzian fit gives a reciprocal space FWHM of 0,93 nm^{-1}, 0,20 nm^{-1} and 0,15 nm^{-1} for 320 K, 390 K and 440 K respectively. The average spacing between two domain walls can be approximately found by Eq. (3.1):

$$L_D\equiv a_i/\gamma_i=4/\Delta Q_{FWHM} \quad . \quad (3.3)$$

67 E. C. Stoner, Rep. Prog. Phys., 11, 43 (1947)
68 O. Rader, T. Mizokawa, A. Fujimori, and A. Kimura, Phys. Rev. B **64**, 165414 (2001).
69 M. De Santis, V. Abad-Langlais,Y. Gauthier, P. Dolle, Phys. Rev. B 69, 115430 (2004)

The typical domain size is then, respectively, of 4.3 nm, 20 nm and 27 nm. Close values are obtained from the Scherrer particle size broadening equation which use a Gaussian lineshape approximation to find the grain size[32] ($L_D = 0{,}94 \times 2\pi / \Delta Q_{FWHM}$).

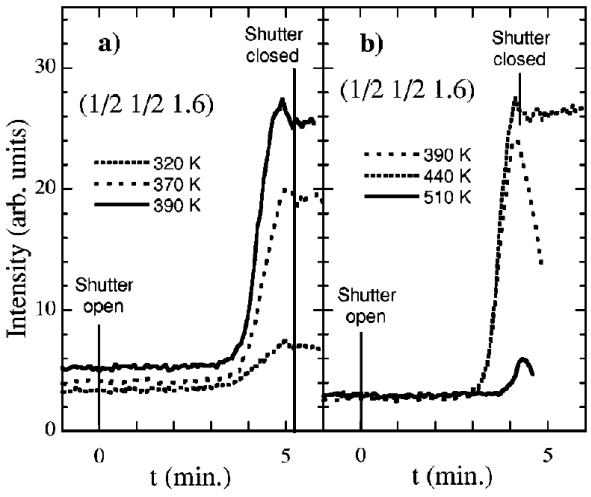

FIG. 18. Intensity of the (1/2 1/2) rod during deposition of Mn on Ni (110) at different substrate temperatures. The data were collected at *L*=1.6. (a) and (b) refer to slightly different deposition rates and slits settings.

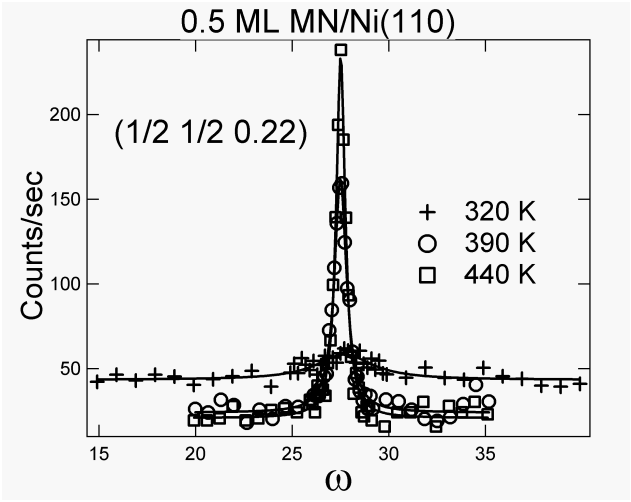

FIG. 19. Rocking scan through a superstructure reflection of Ni(110)-c(2×2)Mn surface, showing the increasing of domain size with temperature.

The Ni(110)-*c*(2×2)Mn surface structure was solved measuring a few CTRs and superstructure rods of the sample grown at 440 K. The structural model which well fit the diffraction data is a 2D alloy where Mn atoms occupy substitutional sites in the outermost layer with a checkerboard arrangement, as shown in Fig. 20.

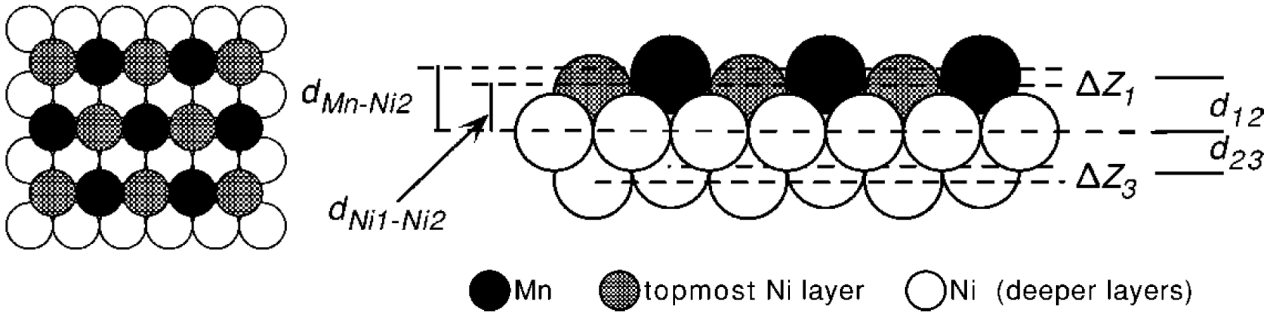

FIG. 20. Model of the 2D Ni(110)-*c*(2×2)Mn phase. b_3 denotes the buckling of the 3rd layer, d_{ij} corresponds to the interlayer distance between layers *i* and *j*. $d_{Mn\text{-}Ni2}$ and $d_{Ni1\text{-}Ni2}$ are the distances from the Mn and Ni sublattices of layer 1 to the second layer.

The detailed structure is described by a reduced number of free parameters: the corrugation in the top and in the 3rd layer (d_{Mn-Ni} , b_3), the first three average interlayer distances (d_{12} , d_{23} , d_{34}), plus a Debye parameter B_1 common to all top layer atoms describing the static disorder, and a scale factor between CTRs and fractional rods. This factor is completely equivalent to the order parameter *S* of bulk alloys, and quantifies the amount of atomic site occupied by the 'right' atom type. A correct value for *S* is only obtained after that the suited correction is applied to the superstructure rods intensities. Fig. 21 shows the C_{Det} correction [Eq.(2.28)] calculated for the measured

superstructure rods using the actual experimental settings. Reflections are indexed using the surface substrate unit cell ($\vec{a}_1=\frac{1}{2}[1\bar{1}0]a_{Ni}$, $\vec{a}_2=[001]a_{Ni}$, $\vec{a}_3=\frac{1}{2}[110]a_{Ni}$) and are labeled (HKL). Also shown in the figure is the Q-space acceptance in the longitudinal direction defined by the slits setting.

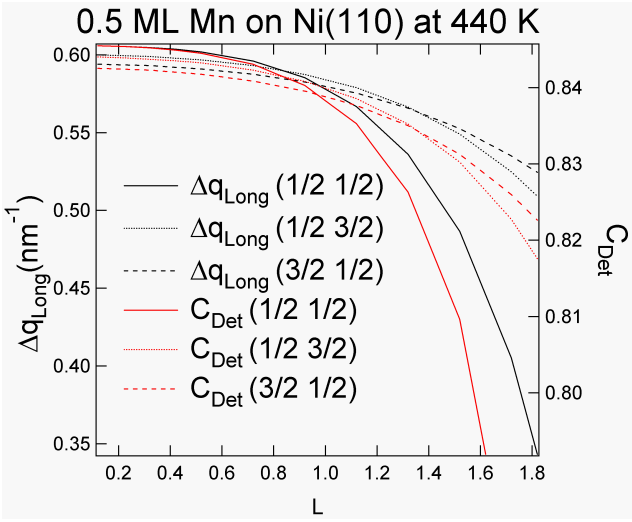

FIG. 21. Detector correction applied to the superstructure Ni(110)-c(2×2)Mn rods (red curves). The longitudinal Q-space resolution is also shown.

The experimental structure factor moduli extracted applying the corrections discussed in chapter 2 are plotted in Fig. 22, together with the calculated best fit.

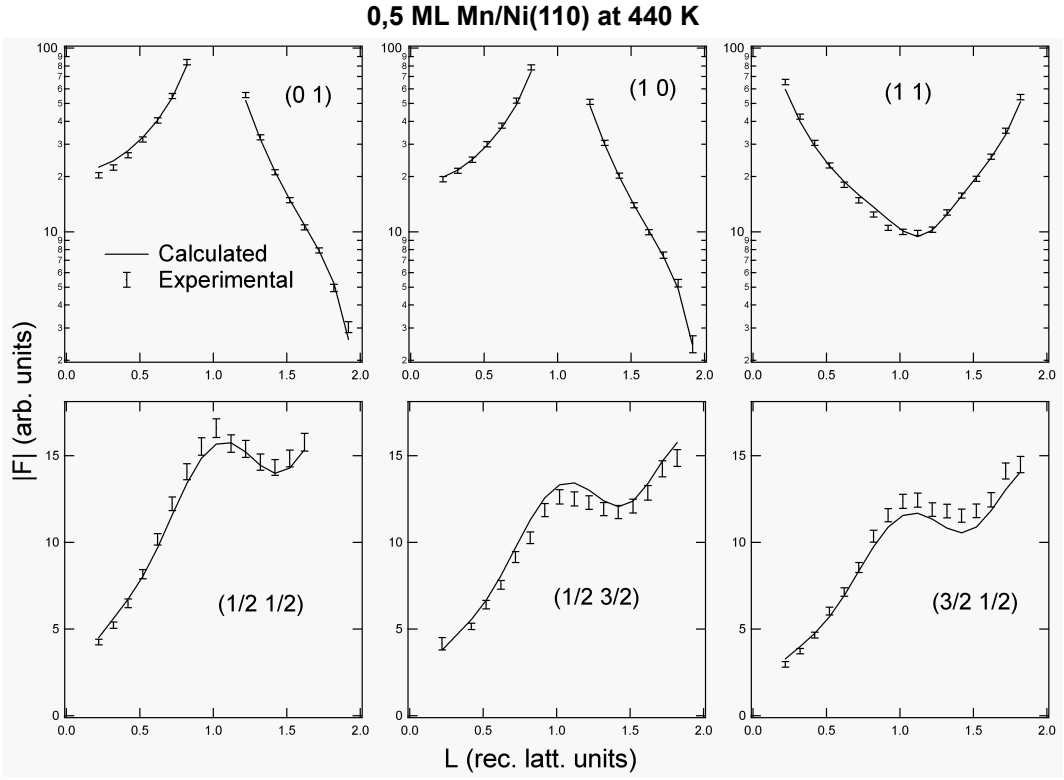

FIG. 22. Experimental rods and best fit curves for the Ni(110)-*c*(2×2)Mn surface alloy

The optimized parameters are given in Table I. The most relevant feature is the large surface rippling with Mn shifted outward by about 0,36 Å. Mn and Ni have close atomic numbers, and indeed the contribution to the superstructure intensities comes more from the geometry of the atomic sites then from their chemical nature. Therefore the data are very sensitive to d_{Mn-Ni} . As a result of this corrugation, the average interlayer distance d_{12} is expanded with respect to bulk.

TABLE I. Best fit parameters of the Ni(110)-c(2×2)Mn structure.

$d_{Mn-Ni}(\AA)$	0,36(1)
$b_3(\AA)$	0,039(2)
$d_{12}(\AA)$	1,284(6)
$d_{23}(\AA)$	1,260(4)
$d_{34}(\AA)$	1,240(2)
$d_{bulk}(\AA)$	1.246
$B_1(\AA^2)$	0,85(8)
$B_{2,3}=B_{Bulk}(\AA^2)$	0.35
Scale	0,81(3)
χ^2	2.5

Similar structures like Cu(100)-*c*(2×2)Pd[70] and also Cu(100)-*c*(2×2)Au,[71] in spite of a larger adsorbate radius, shows a much lower rippling. The growth of 2D surface alloys on fcc metals has been studied extensively.[72,73] A general trend was established to shorten the substrate-adsorbate nearest-neighbor distance, compared to what is expected on the basis of the sum of the atomic (metallic) radii. This was explained, at least in part, by a balance between the tendency to immerse the adsorbed atoms in a higher valence charge density and the compressive repulsion. The contraction is expected to be even larger for the fcc(110) surface, which has a low atomic density. An unusually large buckling in the surface alloy layer was already observed in similar Mn containing surface alloys like Cu(100)-*c*(2×2)Mn,[74,75] Ni(100)-*c*(2×2)Mn[76] and Cu(110)-*c*(2×2)Mn,[77] and was explained with a huge magneto-volume effect, with Mn atoms in a high spin state. Intuitively, electron with parallel spins have to occupy different atomic orbitals, which results in a larger atomic radius. Experimentally, a large magnetic moment was observed for Ni(100)-c(2×2)Mn by x-ray absorption spectroscopy (XAS) and x-ray magnetic circular dichroism (XMCD) experiments.[78]

Here a quite large order parameter (Scale ~0,8) was obtained. Note that the applied data analysis implies that the *Z*-position of each surface atom is function of its chemical

70 S. C. Wu, S. H. Lu, Z. Q. Wang, C. K. C. Lok, J. Quinn, Y. S. Li, D. Tian, F. Jona, and P. M. Marcus, Phys. Rev. B **38**, 5363 (1988).
71Z. Q. Wang, Y. S. Li, C. K. C. Lok, J. Quinn, and F. Jona, Solid State Commun. **62**, 181 (1987).
72 U. Bardi, Rep. Prog. Phys. **57**, 939 (1994).
73 D. Brown, P. D. Quinn, D. P. Woodruff, P. Bailey, and T. C. Q. Noakes, Phys. Rev. B **61**, 7706 (2000).
74 M. Wuttig, Y. Gauthier, and S. Blügel, Phys. Rev. Lett. **70**, 3619 (1993)
75 M. J. Harrison, D. P. Woodruff, and J. Robinson, Phys. Rev. B **72**, 113408 (2005)
76 M. Wuttig, T. Flores, and C. C. Knight, Phys. Rev. B **48**, 12082 (1993)
77 Ch. Ross, B. Schirmer, M. Wuttig, Y. Gauthier G. Bihlmayer and S. Blügel, Phys. Rev. B **57** 2607 (1998)
78 W. L. O'Brien and B. P. Tonner, Phys. Rev. B **51**, 617 (1995)

nature, either if it occupies the 'right' or the 'wrong' site parallel to the surface (at variance with the standard bulk treatment for ordered alloys).

b) Pt(110)-*p*(2×1)Mn[79]

The Pt(110) surface exhibits a (1×2) reconstruction, with one each second surface atomic row missing. This gives the opportunity to elaborate artificial atomic arrangements. Indeed, MBE deposition of ~0,5 ML of Mn on Pt(110)-(1×2) fills the missing rows, resulting in a surface alloy with alternated atomic chains, as depicted in Fig. 23(a), which keeps the same symmetry of the clean surface. As was already the case of Ni(110)-c(2×2)Mn surface, such an atomic configuration within the (110) plane has any counterpart in Pt-Mn bulk phase diagram. The structural analysis obtained thanks to SXRD is reported in detail in ref. 79. This phase is metastable and is unsuitable as germ for nucleation of a new alloy phase. It quickly disappears when the sample is gently annealed and a transition to a (2×1) phase is observed above 560 K. This Pt(110)-(2×1)Mn phase is also 2D and its structure, as obtained by SXRD, is depicted in Fig. 23(b). It consists of atomic rows where Pt and Mn atoms alternate along the $[1\bar{1}0]$ direction. Such an atomic arrangement is found in the mixed (110) planes of the Pt_3Mn bulk phase. Besides the surface corrugation d_{Mn-Pt}, the 3rd layer buckling b_3, and the average interlayer distances $d_{i,i+1}$, a further set of parameters is allowed by symmetry in this phase: the pairings between Pt atoms in even atomic plans (p_{2n}).

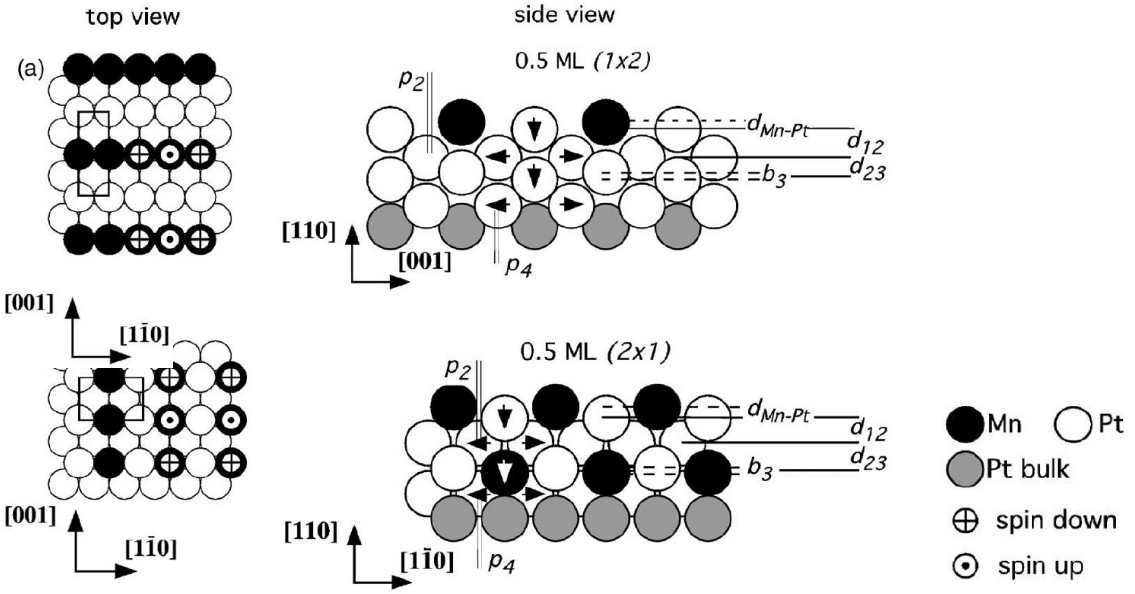

FIG. 23 Model structure of: (a) Pt(110)-(1×2)Mn, and (b) Pt(110)-(2×1)Mn. On the top view, the surface unit cell is shown and the magnetic order is sketched with arrows pointing up and down. Note that the AF ordering doubles the surface unit cell.

The best fit parameters are given in Table II. Like for the MnNi surface alloy, a large corrugation is found with Mn atoms shifted outward by about 0.16 Å.

In addition to the atomic positions, the chemical composition was also fitted for each site of the surface slab. At the surface, the deviation from the ideal model quantify the chemical order parameter. The Mn amount in deeper layers can be neglected, with a

79 M. De Santis, Y. Gauthier, H. C. N. Tolentino, G. Bihlmayer, S. Blügel, and V. Langlais, Phys. Rev. B **75**, 205432 (2007)

noticeable exception: one of the two 3rd layer site [C_{3Mn} , depicted as a Mn site in Fig. 23(b)], is occupied at 30% by Mn atoms. This is the onset of the $L1_2$ phase, because this site is a Mn one in Pt_3Mn.

TABLE II. Best fit parameters of 2D Pt(110)-(2×1)Mn surface alloy. b_i, p_i, and d_{ij} denote the buckling, the pairing, and the average interlayer spacing from layer i to j. $d_{Mn\text{-}Pt}$ is the vertical spacing between Mn and Pt in the first layer (Mn is shifted outward). C_{iMn} and C_{iPt} represent the Pt concentration on the Mn and Pt sites, respectively, of layer i. This labeling is referred to the bulk Pt_3Mn $L1_2$ structure.

	Exp.	Theor.
$d_{Mn\text{-}Pt}$ (Å)	0.16(2)	0.12
b_3 (Å)	0.026(6)	0.11
p_2 (Å)	0.017(4)	0.03
p_4 (Å)	0.006(2)	-
d_{12} (Å)	1.24(1)	1.20
d_{23} (Å)	1.443(6)	1.52
d_{34} (Å)	1.374(3)	1.38
d_{bulk} (Å)	1.3875	1.38
C_{1Pt} (at. % Pt)	80(4)	100
C_{1Mn} (at. % Pt)	5(+13/-5)	0
C_2 (at. % Pt)	96(4)	100
C_{3Pt} (at. % Pt)	100	100
C_{3Mn} (at. % Pt)	70(4)	100
χ^2	2.9	-

The comparison between experimental and calculated structure factor modulus is shown in Fig. 24.

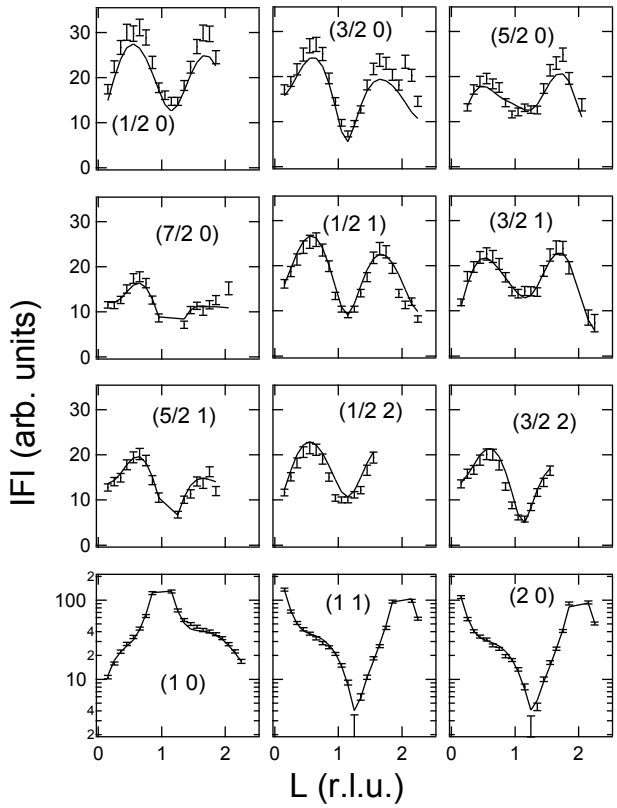

FIG. 24 . Experimental structure factors and best fit for 2D Pt(110)-(2×1)Mn surface alloy (from ref. 79).

The theoretical structure within the same model was obtained by *ab initio* calculations from the Jülich group.[79] The comparison with the SXRD experiment is reported in Table II, and the agreement is fairly good. A quantitative discrepancy is only observed for b_3, which is probably linked to the chemical composition of the Mn site in the 3rd layer. Within the same theoretical framework, the fundamental state energy and the atomic Mn magnetic moment were calculated for a ferromagnetic and an antiferromagnetic Mn ordering (see Fig. 23), and for three different and optimized structures: Pt(110)-(1×2)Mn, Pt(110)-(2×1)Mn, and for a Pt(110)-c(2×2)Mn 2D surface alloy analogous to the Ni(110)-c(2×2)Mn one. The results are reported in Table III.

TABLE III. Calculated magnetic moment (μ), total energy (E_{tot}), and energy difference between F and AF orderings [E(AF−F)]. Energies are given per Mn atom and they are referenced to the AF(2×1) surface alloy.

	(1×2)		(2×1)		c(2×2)	
	F	*AF*	*F*	*AF*	*F*	*AF*
μ (Bohr)	3.94	3.88	3.99	3.99	4.02	3,99
E_{tot} (meV)	267	139	13	0	51	65
E(AF-F) (meV)	-128		-13		14	

In agreement with the experience, the lowest energy phase is the Pt(110)-(2×1)Mn one. It is also observed that the magnetic order is clearly antiferromagnetic for the (1×2) structure, while the energy is almost independent on the magnetic ordering for the other two structure.

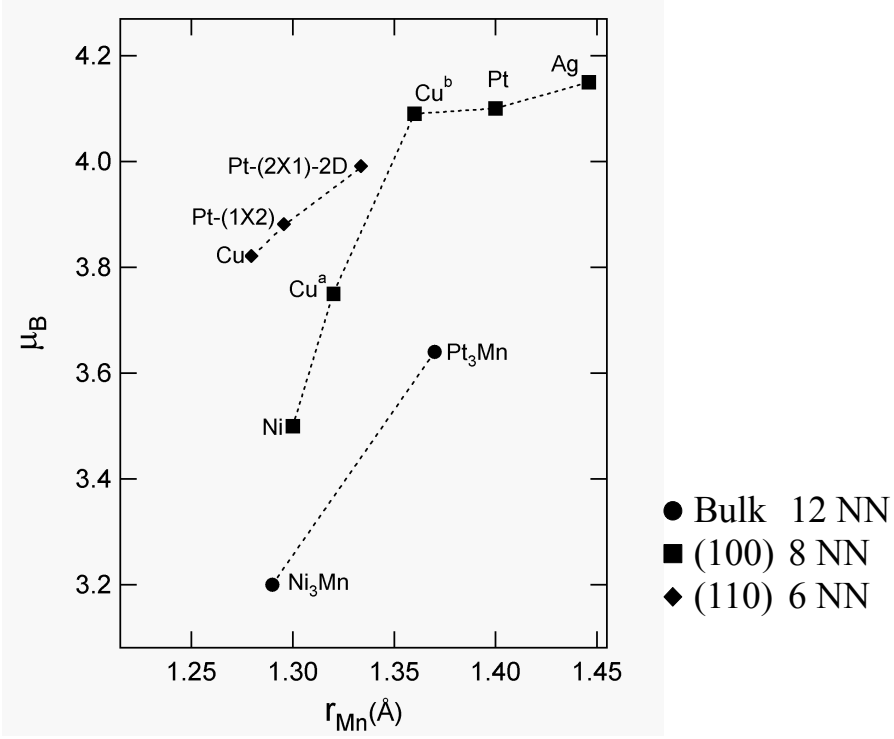

FIG. 25. Calculated magnetic moments of surface Mn atoms versus r_{Mn}. Diamonds are for (110) surfaces. Squares represent Me(100)-c(2×2)Mn surface alloys. Cu[a] and Cu[b] are the values calculated in Refs. 74 and 80, respectively, for the same surface. Experimental values for Ni_3Mn and Pt_3Mn alloys are also given (circles). The experimental r_{Mn} values for (1×2) and (2×1)-2D surfaces are 1.35±0.02 and 1.36±0.01 Å, respectively.

Finally, a large magnetic moment is found for all the calculated structures. In Fig. 25, the calculated Mn magnetic moment for Pt(110)-(1×2)Mn and Pt(110)-(2×1)Mn is plotted versus an effective Mn radius $r_{Mn,\ together}$ with that one calculated for Mn c(2×2) alloys formed on the (100) and (110) surfaces of Cu,[74,77,80] Ni,[81] Pt,[82] and Ag.[83] The radius r_{Mn} is calculated as the difference between the average (theoretical) Mn-Metal nearest-neighbor (NN) distance minus half of the metal-metal bulk distance: $r_{Mn}=\langle D_{Mn-Me}\rangle-(a_{bulk}/\sqrt{2})/2$. It appears clear from the figure the correlation between effective size of the Mn atoms, number of NN, and magnetic moment.

3.5. Codeposited MnPt ultrathin films.

Any attempt to growth ordered (AFM) MnPt alloys by annealing Mn films deposited by MBE on Pt(110) has been unsuccessful. Annealing at 790 K a film of 3 Mn MLs deposited at room temperature resulted in a 3D Pt(110)-(2×1)Mn alloy film with a bulk-like $MnPt_3$ structure (with the lattice distorted by the pseudomorphic epitaxy on the substrate). The order parameter obtained was about 0.8.[79] Similar experiments have been performed by other groups on low indexes Pt surfaces. Deposition of a few Mn monolayers on Pt(001) followed by annealing at about 700 K also gives a $MnPt_3$ surface alloy.[84] In the case of a few Mn MLs deposited on Pt(111), two different alloy phases were observed.[85,86] Annealing at about 770 K results in the $MnPt_3$ phase, which under further annealing at about 920 K transforms into a new surface-layered ($Pt/MnPt_3$) ordered alloy. Theoretical calculations also show as, in terms of the reduction of the total energy, situations where the Mn atoms are completely surrounded by Pt are favored.[87]

MnPt films used in exchange couples bilayers were grown by MBE co-deposition or sputtering.[88,89,90] We have grown such phase by alternate Mn and Pt deposition on a Pt(001) substrate. Here these experiments will be briefly discussed, further details can be found in ref. 54 and [91].

The Pt(001) surface is well suited for the coherent epitaxial growth of MnPt films. The Pt lattice parameter (a_{Pt} = 3.924 Å) lies between the bulk $L1_0$ MnPt cell parameters, a_{PtMn} = 4.002 Å (2.0% > a_{Pt}), c_{Pt} = 3.665 Å (6.6% < a_{Pt}).[92] The smaller mismatch with a_{PtMn} is expected to favors a MnPt(001) film orientation, with the *c*-axis perpendicular to the surface. Alternate deposition of 1 ML of each element mimic the layered structure of MnPt and is expected to favor the chemical order. A drawback of the clean Pt(001) surface

80 M. Eder, J. Hafner, and E. G. Moroni, Phys. Rev. B **61**, 11492 (2000).
81 O. Rader, W. Gudat, C. Carbone, E. Vescovo, S. Blügel, R. Kläsges, W. Eberhardt, M. Wuttig, J. Redinger, and F. J. Himpsel, Phys. Rev. B **55**, 5404 (1997).
82 W. Kim, S. C. Hong, J. Seo, S.-J. Oh, H. G. Min, and J.-S. Kim, Phys. Rev. B **70**, 174453 (2004).
83 O. Elmouhssine, G. Moraïtis, J. C. Parlebas, C. Demangeat, P. Schieffer, M. C. Hanf, C. Krembel, and G. Gewinner, J. Appl. Phys. **83**, 7013 (1998).
84 W. Kim, S. C. Hong, J. Seo, S.-J. Oh, H. G. Min, and J.-S. Kim, Phys. Rev. B **70**, 174453 (2004).
85 S. Gallego, C. Ocal, J. Méndez, X. Torrelles, and F. Soria, Surf. Sci. **482-485**, 1303 (2001).
86 S. Gallego, C. Ocal, M. C. Muñoz, and F. Soria, Phys. Rev. B **56**, 12139 (1997).
87 S. Gallego, M. C. Muñoz, J. Zabloudil, L. Szunyogh, and P. Weinberger, Phys. Rev. B **63**, 064428 (2001).
88 R. F. C. Farrow, R. F. Marks, S. Gider, A. C. Marley, S. S. P. Parkin and D. Mauri,J. Appl. Phys. **81**, 4986 (1997)
89 K. Shimoyama, T. Kato, S. Iwata and S. Tsunashima, IEEE Trans. Magn. 35, 3922 (1999)
90 S. Honda, M. Nawate, and T. Norikane, JMMM **220**, 85 (2000)
91 M. M. Soares, M. De Santis, H. C. N. Tolentino, A. Y. Ramos, M. El Jawad, and Y. Gauthier, Phys. Rev. B **85**, 205417 (2012)
92 P. Villars and L. D. Calvert, *Pearson's Handbook of Crystallographic Data for Intermetallic Phases* (American Society for Metals, Metals Park, OH, 1985).

is its topmost layer quasi-hexagonal reconstruction.[93] This reconstruction is lifted when atoms are adsorbed on the surface, resulting in intermixing in the interface layer.[94]

The black curve in Fig. 26(a) shows the diffracted intensity measured by a line-scan along the Pt (20) CTR on a sample obtained by deposition of 6 MnPt bilayers at room temperature. The (201) reflection is a superstructure Bragg peak for the $L1_0$ phase and hence a peak is expected at L~1 for an ordered MnPt film with the c axis perpendicular to the surface.

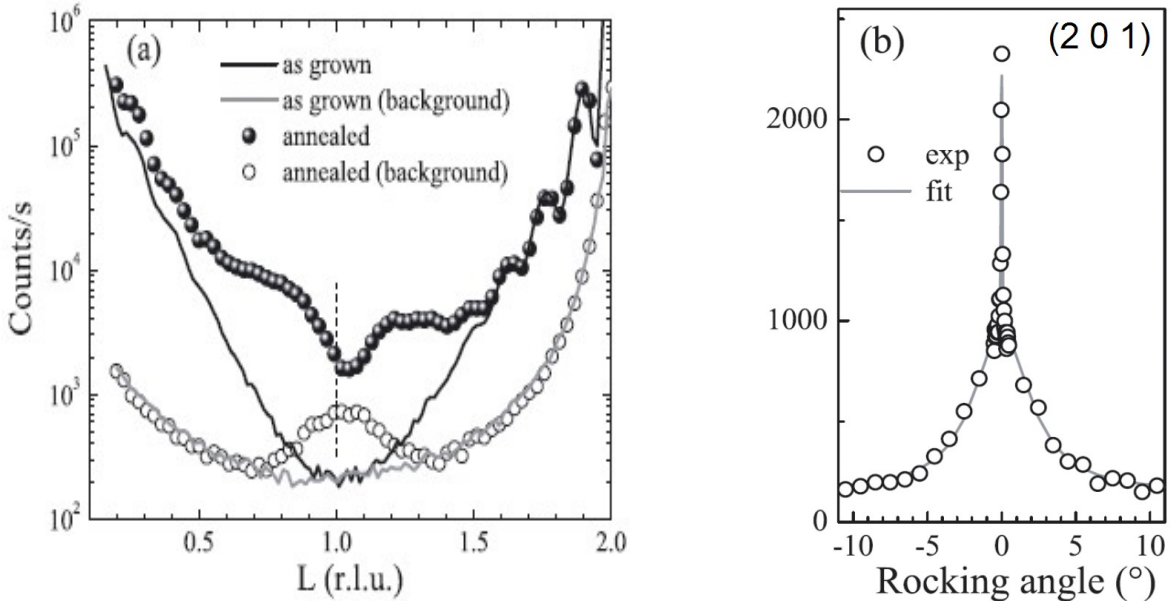

FIG. 26. (a) *L* scans along the (2 0)-CTR for the as deposited 6 MnPt bilayers film (black solid line) and after annealing at 770 K (full circles). The offset scans, along (2.06 0), before annealing (gray solid line) give the background, and after annealing show a broad peak coming from $L1_0$ domains. The vertical (dash) line indicates the position for the rocking scan shown in (b).

The gray line in the figure represents the incoherent x-ray scattered background, measured through a *L*-scan nearby the CTR [at (2.06 0)]. The comparison between CTR and background shows that at *L*=1 there is no coherent scattering, which proves both the lacking of chemical order and a large film surface roughness.[37] A detailed SXRD study showed that the surface is quite rough already after deposition of 1 bilayer, which is due to the three-dimensional Pt growth mode at room temperature on the first Mn ML,[91] preventing the establishment of long range order (LRO). Annealing at 770 K smooths the surface and the diffracted intensity in anti-phase position increases (full circles), but still no peak arising from chemical order is observed. The fringes close to the Bragg peaks keep the same frequency, indicating that the film thickness does not change under annealing [see Eq. (2.18)]. The interdiffusion at the interface with the substrate is therefore negligible, and there is no Pt enrichment of the film. Scanning nearby the CTR a bump now appears. A large rocking scan at the (2 0 1) position [Fig. 26(b)] explains its origin. After annealing some chemical order is indeed established, but the domain size is so small (about 2 nm) that the peak on the CTR is hidden by the intensity diffracted from the flat surface.

A quite different situation is encountered keeping the substrate at 570 K during the same process of alternated Mn and Pt deposition. In this case layer by layer growth, and a LRO peak of the wanted MnPt(001) phase are observed, already at the first stages (Fig. 27).

Domains of the MnPt phase with the c axis parallel to the surface are observed for

93 D. L. Abernathy, S. G. J. Mochrie, D. M. Zehner, G. Grübel, and D. Gibbs, Phys. Rev. B **45**, 9272 (1992).
94 B. Schaefer, M. Nohlen, and K. Wandelt, J. Phys. Chem. B **108**, 14663 (2004)

both the film grown at room temperature and then annealed at 770 K, and for that one grown at 570 K, but they represent a minority component for the last one.

For studying the exchange bias properties, both the films discussed above were covered with a ferromagnetic layer. The first sample was covered with about 2 nm of iron, which has an in-plane magnetization. The second one was covered by about 2 nm of an ordered FePt(001) alloy, which has an out of plane easy axis. Both samples were capped with ~2 nm of Pt which prevents the oxidation of the magnetic layers thus allowing for *ex-situ* magnetic characterization.

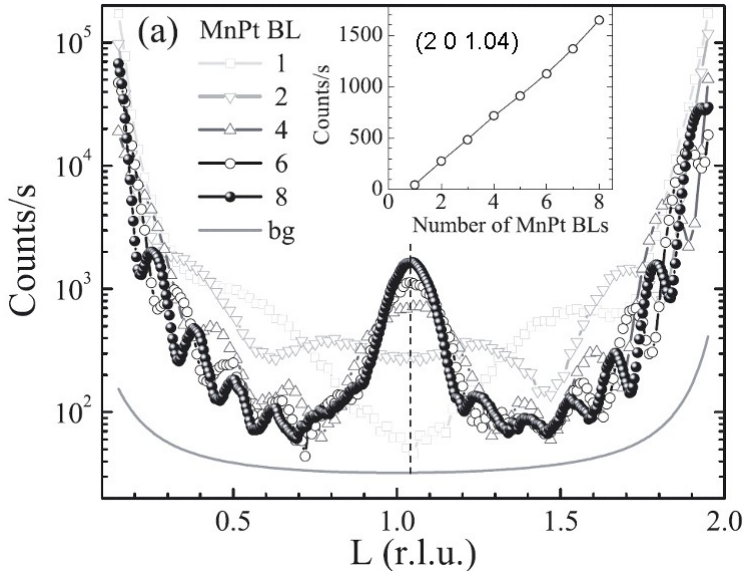

Fig. 27 *L* scans along the (2 0)-CTR during MnPt deposition at 570 K for 1, 2, 4, 6, and 8 (closed circle) MnPt bilayers (BLs); the background is also shown (gray solid line). Inset: counts at the (2 0 1.04) reciprocal space point (indicated by vertical dashed line) as a function of the number of deposited MnPt BLs.

For bulk-like magnetic structure (Fig. 14) the MnPt(001) plane is compensated, therefore for a flat interface no exchange coupling is expected. A coupling requires defects at the interface and/or in the film structure. Indeed polar magneto-optical Kerr rotation (MOKE) measurements on the Pt/FePt/MnPt/Pt(001) sample showed a small exchange bias at 5K, which vanishes after a few hysteresis loops (Fig. 28).

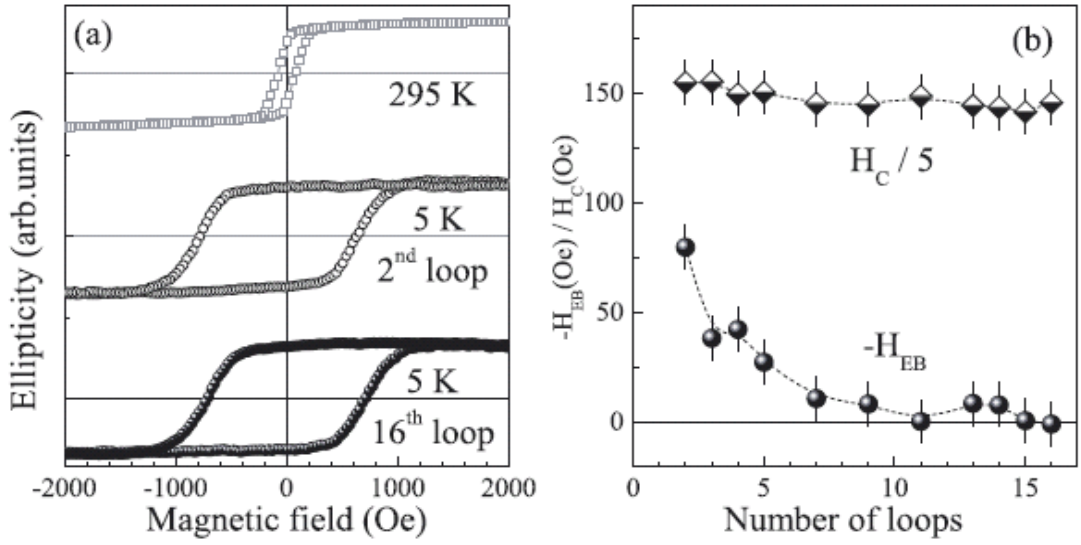

Fig. 28. (a) Polar MOKE hysteresis loops of the Pt/FePt/MnPt/Pt(001) film at 295 K (squares) and after field cooling down to 5 K: second loop (open circles) and sixteenth loop (closed circles). (b) Coercivity (H_C) and exchange bias shift ($-H_{EB}$) as a function of the number of loops measured (from ref. 91).

The magnetic field cooling from RT down to 5 K creates a metastable state with uncompensated spins that are responsible for the initial EB shift.

On the Pt/Fe/MnPt/Pt(001) sample, which has in-plane magnetization, MOKE measurements were performed in longitudinal geometry (Fig. 29).

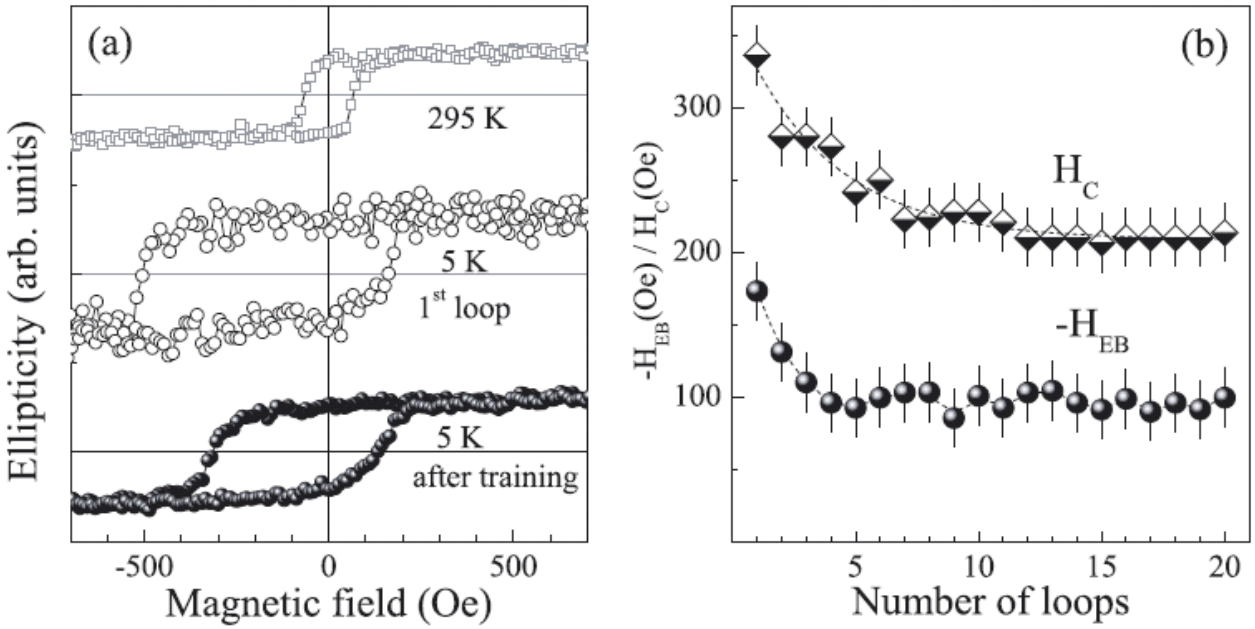

Fig. 29 Longitudinal MOKE hysteresis loops of the Pt/Fe/MnPt/Pt(001) film along the [100] Fe easy axis at 295 K (squares) and after magnetic field cooling to 5 K: first loop (open circles) and average from loop 10 to 20 (closed circles). (b) Coercivity (H_C) and exchange bias shift ($-H_{EB}$) as a function of the number of loops (from ref. 91).

An exchange bias at 5 K was observed, which is the result of a thermodynamically stable spin configuration at the interface. This is attributed to the coupling of the Fe layer with the observed MnPt domains having the c axis parallel to the surface. Indeed, in type-II magnetic structure (Fig.14), MnPt(100) planes are not compensated.

4. CoO/PtCo/Pt(111)

Transition-metal oxides (TMO) represent an important class of antiferromagnetic materials because of their high Néel temperature and chemical stability. Most of the reported investigations in which an insulated AFM layer is used to bias ferromagnetic films involve CoO or NiO monoxide. The bulk T_N for CoO is 293 K; for NiO, it is 525 K. For $Ni_xCo_{1-x}O$, T_N varies linearly with x.[95] Above T_N, both oxides have a rocksalt structure with close lattice constant (a_{CoO} =4.261 Å,[96] a_{NiO} =4.17 Å). A distortion is observed below the Néel temperature. For CoO the structure becomes almost tetragonal (indeed is slightly monoclinic).[96] In the AFM state of both CoO and NiO spins order parallel on (1 1 1) planes (as indexed in the cubic structure), and take anti-parallel spin directions on adjacent planes (i.e., the spins of next nearest-neighbors along <1 0 0> directions are anti-parallel due to the superexchange interaction via oxygen atoms) (Fig. 30). For CoO, spins are oriented in the ac monoclinic plane at about 20° from the [001] direction.[96] A lower angle was found both by a previous experiment[97] and by theoretical calculations,[98] which deduced a spin alignment along the $[\bar{1}\,\bar{1}\,7]$ direction. The uncompensated (111) face is then expected to give rise to a large exchange coupling when grown in epitaxy on a ferromagnetic layer.

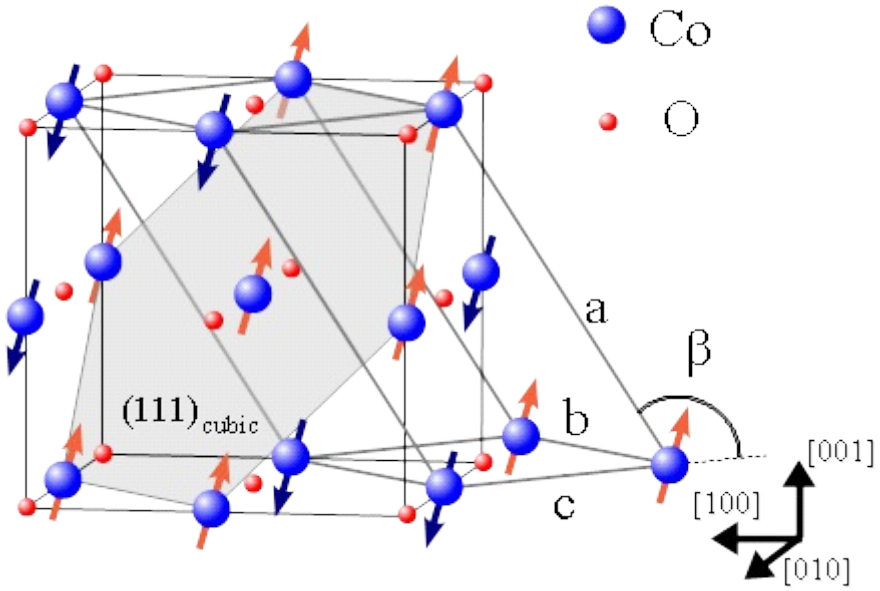

FIG. 30. CoO structure and spins ordering in the AFM state.

$L1_0$ FePt and CoPt ordered alloys are promising medium material for high-density magnetic recording because their high magnetocrystalline anisotropy suppresses superparamagnetism in nanoscale particles and films. The origin of such an anisotropy resides in the large spin-orbit coupling of Pt atoms and in the strong hybridization of Pt *d* bands with the *3d* bands of Co or Fe.[99] This needs to be associated with the presence of a uniaxial anisotropy of the crystal structure, like is the case for the $L1_0$ phase.

95 M. J. Carey and A. E. Berkowitz, Appl. Phys. Lett. 60 3060 (1992)
96 W. Jauch, M. Reehuis, H. J. Bleif, F. Kubanek, and P. Pattison, Phys. Rev. B **64**, 052102 (2001)
97 W. L. Roth, Phys. Rev. **110**, 1333 (1958)
98 A . Schrön, C. Rödl, and F. Bechstedt, Phys. Rev. B **86**, 115134 (2012)
99 A. Sakuma, J. Phys. Soc. JAP. **63**, 3053 (1994)

Co_3Pt hcp(0001) films obtained by codeposition on a substrate kept at about 650 K show chemical order along the growing direction, which has no counterpart in the bulk phase diagram.[100] A large perpendicular magnetic anisotropy (PMA) is exhibited by these films, as well as by $Pt_{75}Co_{25}$(111) fcc films, grown in the same temperature range.[101] These Pt-rich films show no LRO, but it was suggested that Co platelets form as a surface-driven-growth effect during codeposition.[102] It is indeed well known that Pt_xCo_{1-x}(111) bulk alloys show Pt segregation at the surface and an oscillating Pt concentration profile in the underlying layers.[103]

On this basis, the pseudomorphic growth of a sub-nanometric CoPt alloy film on top of Pt(111) will be discussed in this chapter, which shows PMA at room temperature. It will be covered by an epitaxial NiO(111)/CoO(111) nanometric multilayer, exhibiting an exchange coupling at the interface.

4.1. PtCo/Pt(111)[104,105]

At the initial stage of Co deposition on Pt(111) at room temperature, the first atomic layer occupies preferably the three-fold Pt fcc hollow sites at the surface as sketched in Fig. 31. Due to the mismatch between the bulk Co and Pt lattice the Co overlayer becomes strained. The tensile stress is partially relieved by dislocations.[106]

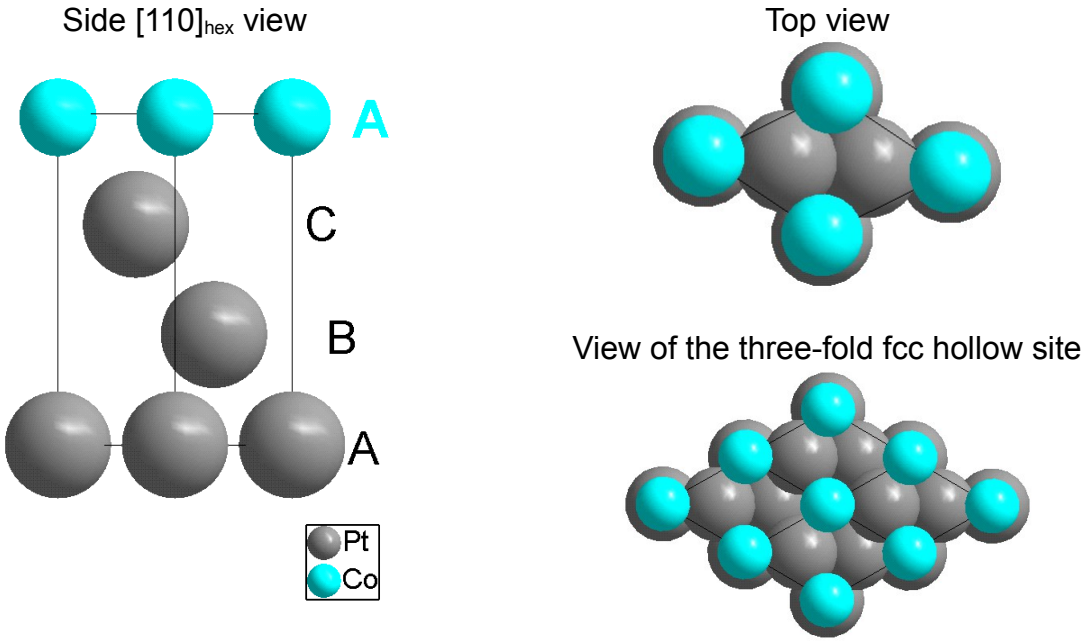

FIG. 31. Side view (a) and top view (b) of Co on top of Pt(111), represented within its hexagonal surface unit cell. The Co three-fold coordination is shown in (c).

A subsurface growth mode is instead observed when 1 ML of Co is deposited onto Pt(111) held at about 540 K. A thermally activated exchange reaction leads to a bilayer

100 G. R. Harp, D. Weller, T. A. Rabedeau, R. F. Farrow, and M. F. Toney, Phys. Rev. Lett. **71**, 2493 (1993).
101 C.-J. Lin and G. L. Gorman, Appl. Phys. Lett. **61**, 1600 (1992).
102 A. L. Shapiro, P. W. Rooney, M. Q. Tran, F. Hellman, K. M. Ring, K. L. Kavanagh, B. Rellinghaus, and D.Weller, Phys. Rev. B **60**, 12 826 (1999)
103 Y. Gauthier, R. Baudoing-Savois, J. M. Bugnard, U. Bardi, and A. Atrei, Surf. Sci. **276**, 1 (1992).
104 M. De Santis, R. Baudoing-Savois, P. Dolle, and M.C. Saint-Lager, Phys. Rev. B **66**, 085412 (2002).
105 L. Giovanelli, M. De Santis, G. Panaccione, F. Sirotti, P. Torelli, I. Vobornik, R. Larciprete, S. Egger, M.C. Saint-Lager, P. Dolle, and G. Rossi, J. Mag. Mag. Mat. **288**, 236 (2005)
106 E. Lundgren, B. Stanka, M. Schmid, and P. Varga, Phys. Rev. B **62**, 2843 (2000)

structure with the Co mainly buried in the second atomic layer, as we showed by SXRD.[104,105]

Figure 32 illustrates the drastic change in the CTRs structure factors measured on the two interfaces, obtained by deposition at room temperature (followed by annealing at 430 K, to decrease the roughness) and at 540 K, respectively. The last one was fitted with a bilayer structure where Co and Pt exchange in the last two layers, maintaining the bulk-like stacking (...*ABCA*, see Fig. 31) of the hexagonal planes. Structural parameters are the Co atomic concentration and the interlayer distances between the three layers closest to the surface.

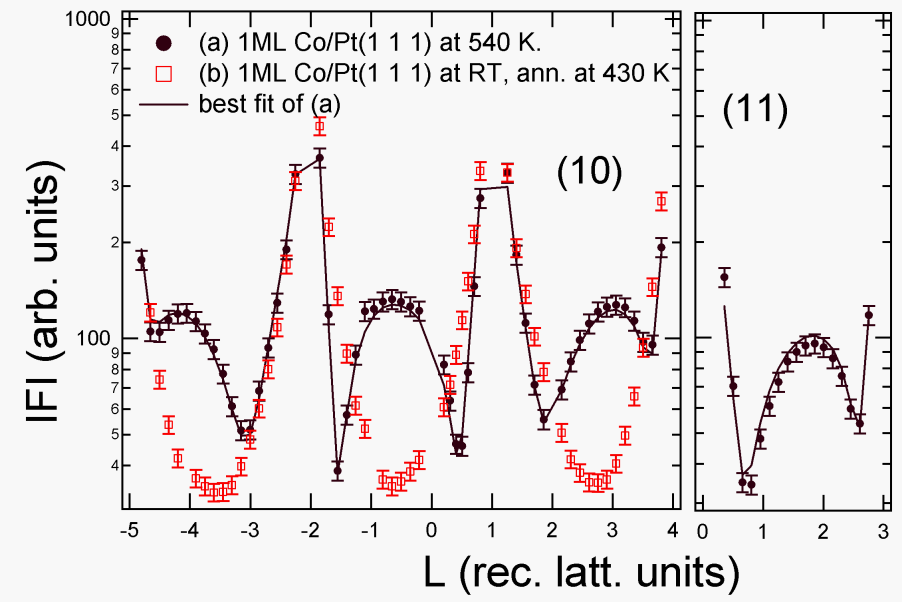

FIG. 32. Experimental CTRs of 1 ML Co/Pt(111) deposited at 540 K and best fit curves. The experimental data of 1 ML Co/Pt(111) deposited at RT are also shown (empty red squared). The CTRs are labeled using the hexagonal surface unit cell[107] and the Friedel's law ($|F(0,1,L)| \equiv |F(1,0,\bar{L})|$)

The best fit values are given in Table IV. The result is a very rich Co layer (C_2 ~ 80 %) sandwiched between two almost Pt layers. The interlayer distances are strongly compressed, much more than observed at the surface of fcc $Pt_{80}Co_{20}$(111) alloys.[103] This is due to the strained Co layer, where atoms take the in-plane Pt NN distance of 2.775 Å (it is of 2.51 Å in bulk Co).

TABLE IV. Best fit Pt-Co bilayer structure.

C_1	$20(+2/-20)\%$
C_2	$80(5)\%$
C_3	$5(+2/-5)\%$
d_{12}(Å)	2.09(4)
d_{23}(Å)	2.06(4)
d_{bulk}(Å)	2.266

All criteria for a large PMA are here fulfilled. Fig. 33 shows a comparison of the room

107 G. Grübel, K. G. Huang, D. Gibbs, D. M. Zehner, A. R. Sandy, and G. J. Mochrie, Phys. Rev. B **48**, 18119 (1993)

temperature polar-MOKE measurements performed on 1 ML Co/Pt(111) deposited at RT and at 540 K. Both surfaces exhibit an almost rectangular hysteresis loop, and hence PMA. In the first case however the coercive field is quite small (of 80 Oe), and it strongly increases in the bilayer structure.

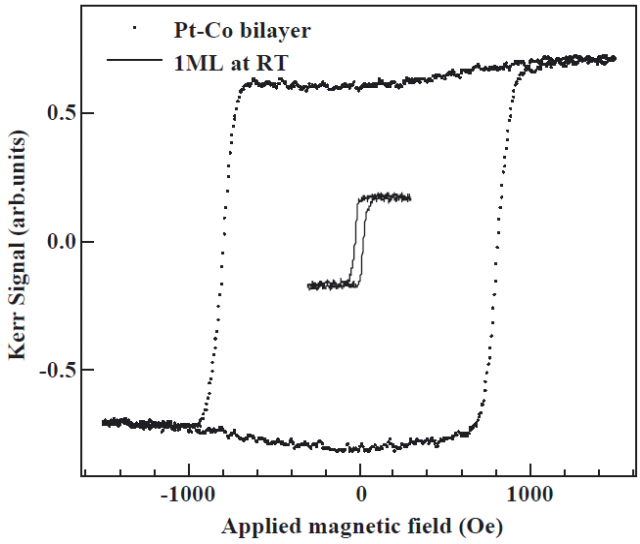

FIG. 33. Polar Kerr hysteresis loop for, respectively, 1 ML of Co/Pt(111) grown at RT (smaller loop) and at 540 K (larger loop) (from ref. 46)

The local magnetism can be probed by XMCD on the Co $L_{2,3}$ adsorption edges, using magneto-optical sum rules that give the orbital and spin magnetic moment of Co atoms separately.[108,109] The values obtained for the Pt-Co bilayer structure ore given in Table V,[105] and compared with that one for $CoPt_3$(111) films grown at 690 K and with the bulk values.

TABLE V. Effective spin and orbital magnetic moments of Co in the Pt-Co bilayer compared to that one of a $CoPt_3$ film grown at 690 K and of Co HCP.

	m^{eff}_{spin} (μ_B)	m_{orb} (μ_B)
Pt-Co bilayer on Pt(111)	1.7(2)	0.39(5)
$CoPt_3$(111) grown at 690 K (ref. [110])	1.6(1)	0.30(2)
Co HCP (ref. [111])	1.62	0.15

4.2. CoO/Pt(111)

Ultrathin TMO films are investigated mainly for their magnetic and catalytic properties.[112,113] In exchange coupling applications involving TMO, a key parameter is the control of the AFM/FM interface structure at the atomic level, which determines the

108 B.T. Thole, P. Carra, F. Sette, G. van der Laan, Phys. Rev. Lett. **68**, 1943 (1992).
109 P. Carra, B.T. Thole, M. Altarelli, X. Wang, Phys. Rev. Lett. **70**, 694 (1993).
110 W. Grange, M. Maret, J.-P. Kappler, J. Vogel, A. Fontaine, F. Petroff, G. Krill, A. Rogalev, J. Goulon, M. Finazzi, N.B. Brookes, Phys. Rev. B **58**, 6298 (1998).
111 C.T. Chen, Y.U. Idzerda, H.-J. Lin, N.V. Smith, G. Meigs, E. Chaban, G.H. Ho, E. Pellegrin, F. Sette, Phys. Rev. Lett. **75**, 152 (1995).
112 Hans-Joachim Freund, Helmut Kuhlenbeck and Volker Staemmler, Rep. Prog. Phys. **59**, 283 (1996)
113 E. Lundgren, A.Mikkelsen, J. N. Andersen, G. Kresse,M. Schmid, and P. Varga, J. Phys. Condens. Matter **18**, R481 (2006).

strength of the exchange interaction.

CoO grows with the (111) orientation on several fcc(111) metallic substrates, like e.g. on Au(111).[114] Growth of CoO on Pt(111) at RT was investigated by RHEED (reflection high-energy electron diffraction), resulting in ultrathin CoO(111) films described as relatively flat.[115] The (111) planes in the rocksalt structure are formed alternatively by pure oxygen and pure cobalt layers, thus the bulk terminated surface is polar, and the calculated surface energy is infinite.[116,117] This divergence can be suppressed by various mechanisms,[118] e.g. surface reconstructions,[119] a surface phase with different structure,[120] vacancy islands,[121] reduced charge of the surface ions,[122] non-stoichiometric surfaces.[123] For ultrathin films, the polar surface divergence problem is alleviated; nevertheless, it reduces the stability of the films, making it difficult to achieve layer-by-layer growth of well-ordered nanometric CoO(111) films.

The reduction of the critical temperature with the thickness is a general behavior expected in several systems including magnetic films, when their size become smaller than the characteristic correlation length.[124] Experiments have evidenced a drastic reduction of the Néel temperature in CoO films. Measurements performed on CoO/SiO_2 multilayers have shown that the transition temperature rapidly decrease for CoO films thinner than 6nm.[62]

a) Surface structure and morphology of CoO/Pt(111)[125]

Scanning tunneling microscopy (STM) is the most powerful technique allowing a direct, real-space determination of the surface structure at an atomic level and of the surface roughness.[126] It is based on the quantum mechanical process of electron tunneling through the vacuum barrier, which happens when sample and tip are close enough. The tunneling current I_t probe the convolution of the tip and sample local density of states, integrated over an energy range defined by the sample bias voltage V_s. It decay exponentially with the sample tip distance.[127] All the images shown below are taken in constant current mode, with the tip following the surface electron density corrugation (topographic mode).

Figure 34 shows STM images of the surface Co oxide obtained by deposition of 1 ML of Co on Pt(111) followed by O_2 exposure at (a) RT, (b) 450 K, and (c) 570 K, respectively. Samples were shortly annealed at the same temperature before to introduce oxygen. The dosing time was typically 10 min. at 10^{-7} mbar, i.e. ~50 Langmuir (L, 1 L corresponds to a dosage of $10^{-6} torr \times s$). Image (d) was obtained after a further annealing of (c) at 730 K in 10^{-8} mbar O_2 for 10 min. (direct annealing at such a high temperature would result in Co dissolution in the substrate).

In (a) we observe small clusters, ~250 pm in height and 2 nm in size, resulting from the

114 A. Chassé, L. Niebergall, M. Heiler, H. Neddermeyer, K.-M. Schindler, Surface Sci. **602**, 443 (2008)
115 S. Entani, M. Kiguchi, and K. Saiki, Surf. Sci. **566–568**, 165 (2004).
116 J. W. Tasker, J. Phys. C **12**, 4977 (1979).
117 J. Goniakowski, F. Finocchi, and C. Noguera, Rep. Prog. Phys. **71**, 016501 (2008).
118 C. Noguera, J. Phys. Condens. Matter **12**, R367 (2000).
119 D. Wolf, Phys. Rev. Lett. **68**, 3315 (1992).
120 W. Meyer, D. Hock, K. Biedermann, M. Gubo, S. Müller, L. Hammer, and K. Heinz, Phys. Rev. Lett. 101, 016103 (2008).
121 O. Dulub, U. Diebold, and G. Kresse, Phys. Rev. Lett. **90**, 016102 (2003).
122 W. Hebenstreit, M. Schmid, J. Redinger, R. Podloucky, and P.Varga, Phys. Rev. Lett. **85**, 5376 (2000).
123 C. Noguera and J. Goniakowski, J. Phys. Condens. Matter **20**, 264003 (2008).
124 N. D. Mermin, and H. Wagner, Phys. Rev. Lett. **17**, 1133 (1966)
125 M. De Santis, A. Buchsbaum, P. Varga, and M. Schmid, Phys. Rev. B **84**, 125430 (2011)
126 G. Binning, H. Rohrer, Rev. Mod. Phys. **71**, S324 (1999)
127 R. M Tromp, J. Phys.: Condens. Matter **1**, 10211 (1989)

oxidation of previously Co-covered areas, whereas no islands appear on Pt areas (dark regions). Clusters are the result of the expulsion of atoms from the underlying Co layer during oxidation: a bulk CoO(111) plane has a Co atomic density ~15% lower than pseudomorphic as-deposited Co on the Pt(111) surface. The dendrites formed when depositing Co submonolayers on Pt(111)[128] are still observed on the oxidized sample. These dendrites should consist mainly of Pt, and almost no clusters form on them.

In Fig. 34(b) the clusters are wider, the height is about twice, and they take the three-fold substrate symmetry. Finally, a flat surface oxide is obtained by dosing oxygen at 570 K (brighter regions on the terraces correspond to a corrugation of 50 pm only, and are related either to delocalized electronic states or to additional physisorbed oxygen).

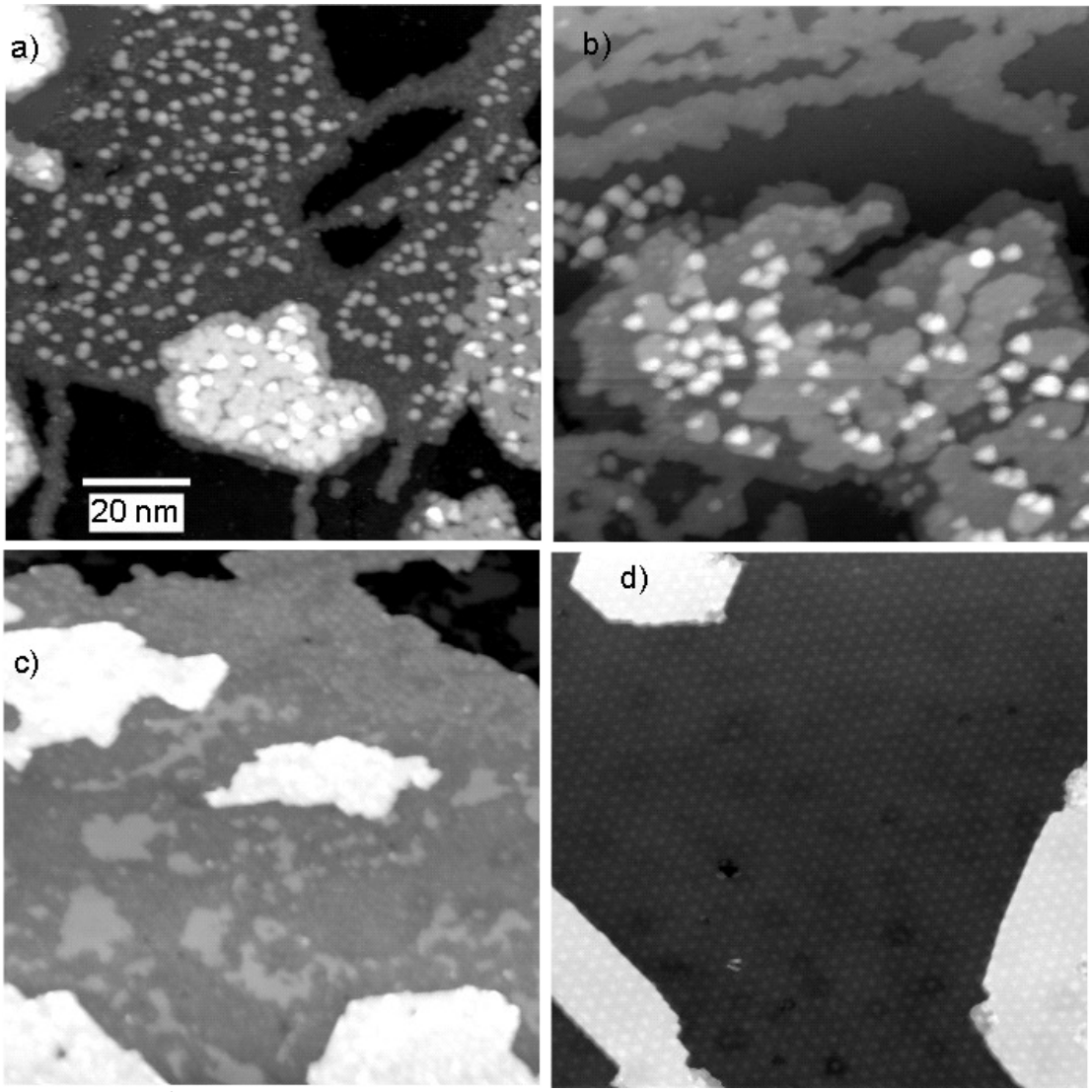

FIG. 34. 100x100 nm^2 STM images of 1 ML Co/Pt(111) deposited at RT and: (a) dosed with 50 L O_2; (b) annealed and dosed with 50 L O_2 at 450 K; (c) annealed and dosed with O_2 at 570 K; (d) sample (c) followed by a further annealing under oxygen at 730 K. Image processing was used in (d) to reduce the step height,making the corrugation on the terraces more apparent. (I_t = 0.1 nA; V_s = +0.5 V in (a), (b), and (d); V_s = +1.2 V in (c)).

Further annealing at higher temperature in O_2 (d) results in an almost flawless moiré pattern of period 2.70(5) nm. Atomic resolved images of this surface (Fig. 35) show the CoO(111) hexagonal mesh with an interatomic distance d_{oxide} = 309 ± 2 pm. This misfit

128 E. Lundgren, B. Stanka, W. Koprolin, M. Schmid, and P. Varga, Surf. Sci. **423**, 357 (1999).

value roughly agree with that ones calculated from LEED images (Fig. 36). The moiré is given by the (unrotated) superimposition of the substrate lattice and of the epitaxial CoO, with 10 Pt surface cell (d_{Pt} = 277.5 pm) corresponding to 9 ones of the CoO layer ($\frac{10}{9} d_{Pt}$ = 308.3 pm). A ball model of the structure is shown in Fig. 37. Within the supercell, Co atoms shift from fcc to hcp and on top sites with respect to the substrate. A comparison with images showing triangular dislocation loops allows to identify each kind of site in the STM image.[125] Low energy ion scattering (LEIS) on this same surface shows contributions mainly from Co and O atoms, the Pt peak being only a few percent of the total signal. Despite the large annealing temperature there is no Pt segregation in the top layer. Assuming that the Pt signal comes from uncovered Pt areas, comparison with standard spectra of pure Pt indicates that 1% of the surface is pure Pt. The CoO stoichiometry of the layer is roughly confirmed by Auger electron spectroscopy, by comparison with thicker CoO films. The structure therefore looks very closely to that one of 2D oxygen terminated FeO on Pt(111).[129,130,131,132]

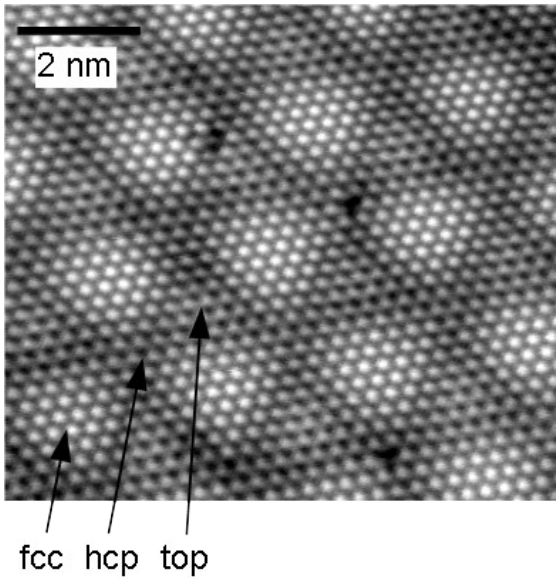

FIG. 35. Atomic resolved image of the CoO/Pt(111) moiré structure. (I_t = 1 nA; V_s = -2 mV). Regions with Co in fcc, hcp, and on-top sites of the Pt substrate atoms were identified by comparison with images showing triangular stacking faults.[125]

FIG. 36. LEED pattern of the moiré shown in Fig. 34(d) (E = 120 eV).

It is interesting to note that the in plane hexagonal CoO lattice constant (d_{oxide} = 309 ± 2 pm) is even larger than the corresponding bulk value (301 pm), which is at the opposite of what is expected from the epitaxy relationship. Indeed the in plane expansion should allow a compression of the Co-O interlayer distance, reducing then the surface dipole energy. Such an out-of-plane contraction was observed in FeO/Pt(111).[132] The moiré structure is then expected to submit the Pt interface layer to a large stress.

129 H. C. Galloway, J. J. Benitez, and M. Salmeron, Surf. Sci. **298**, 127 (1993).
130 H. C. Galloway, P. Sautet, and M. Salmeron, Phys. Rev. B **54**, R11145 (1996).
131 M. Ritter, W. Ranke, and W. Weiss, Phys. Rev. B **57**, 7240 (1998).
132 Y. J. Kim, C. Westphal, R. X. Ynzunza, H. C. Galloway, M. Salmeron, M. A. Van Hove, and C. S. Fadley, Phys. Rev. B **55**, R13448 (1997).

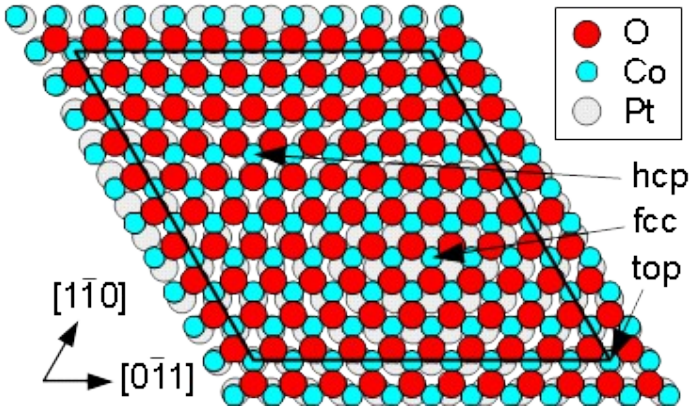

FIG. 37. Ball models of the moiré structure

The CoO bilayer structure would result then considerably distorted with respect to the rocksalt one, like is the case of CoO on Ir(100). It was shown that a few monolayer thick CoO films grow on Ir(100) in (111) orientation. Despite the fact that the bulk of these films has a rocksalt structure, near the surface there is a switch towards the wurtzite type structure, with a reduced Co-O interlayer distance.[120]

The moiré structure might find applications as templates for growing metal nanostructures. The similar FeO/Pt(111) moiré has been used for growing fairly regularly arranged self-assembling arrays of gold adatoms.[133]

Growing CoO films of nanometric thickness on Pt(111) results in a rough surface and in a Stranski-Krastanov growth mode over a large temperature range. Fig. 38 (a) and (b) shows the STM images collected on films obtained by three cycles of Co deposition (1 ML) and O_2 dosing (50 L) at 450 K and 570 K, respectively, pursuing the growth beyond the first monolayer stage shown in Fig. 34 (b) and (c), respectively (the sample of Fig. 38(b) has been submitted to a final annealing at 740 K in oxygen). Both surfaces exhibit triangular shaped islands, whose size increases with temperature, on top of an epitaxial first layer. This last one is the moiré structure in (b), while in (a) a triangular dislocation network is formed, which is shown in the inset.

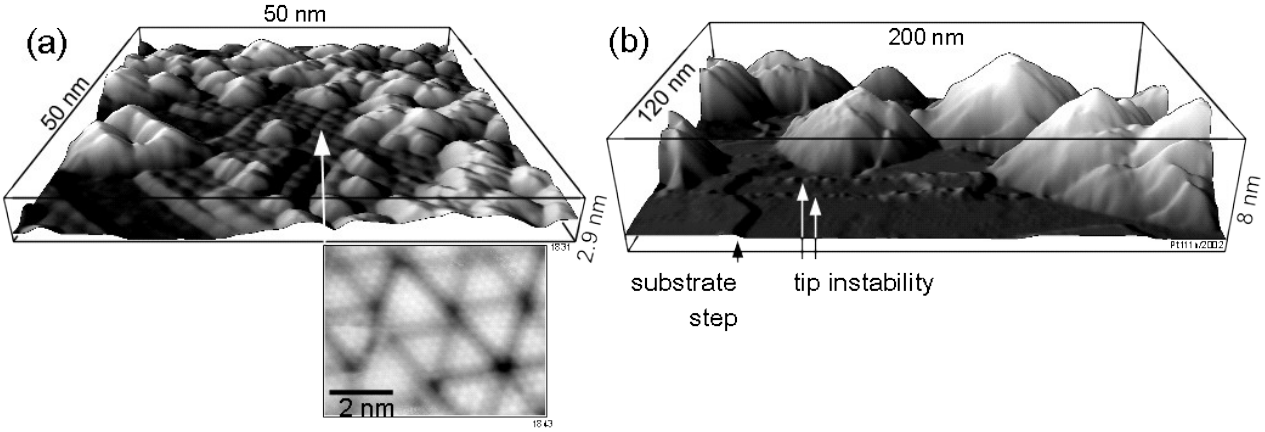

FIG. 38. STM images of thicker films. (a) Three cycles of Co deposition (1 ML) and O2 dosing (50 L) at T = 450 K (V_s = −1 V, I_t = 0.1 nA). (b) The same procedure at 570 K, followed by annealing in oxygen at 740 K at the end (V_s = 1.2 V, I_t = 0.1 nA). In both cases, the first monolayer is deposited at RT. The inset in (a) shows a zoom in the flat region in between the islands.

133 L. Giordano, G. Pacchioni, J. Goniakowski, N. Nilius, E. D. L. Rienks, and H.-J. Freund, Phys. Rev. Lett. **101**, 026102 (2008).

b) Structure of ultrathin CoO/Pt(111) films

A complementary description of the structure of the CoO films discussed in the previous section is obtained by *in-situ* SXRD. Here the discussion is focused on films grown at T < 470 K. Higher oxidation temperatures would compromise the stability of the FM layer in the exchange coupling system discussed in the following.

Figure 39 shows SXRD measurements on a CoO/Pt(111) sample grown by three steps of alternate Co deposition (1 ML) and O_2 exposure (20 L) at 430 K. The diffracted intensity is collected at each step, scanning the momentum transfer parallel to the (010) direction of the hexagonal reciprocal space Pt(111) surface cell. A peak is observed at (0 0.925 0.48), starting from a thickness of 2 CoO ML. It correspond to the position of the $(01)_{CoO\text{-}hex}$ rod of the hexagonal CoO(111) surface cell, as confirmed by a deep investigation of the reciprocal space. We can conclude from SXRD data that a few monolayer thick films grow in orientation epitaxy with the substrate and with an in-plane lattice constant value very close to the corresponding CoO bulk one ($\frac{a_{Pt}}{a_{CoO}} = 0.921$).

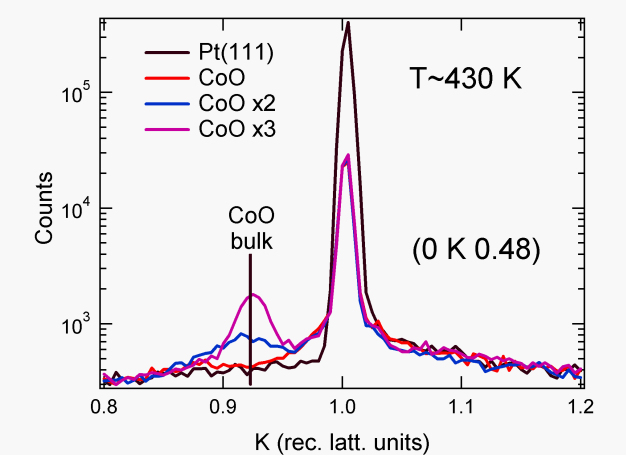

FIG. 39. SXRD measurements collected by scanning the momentum transfer parallel to the $\vec{b}_2$ reciprocal space vector of the hexagonal Pt(111) surface cell. The curves refer to clean Pt substrate and to subsequent three steps of Co deposition (1 ML) and O_2 dosing (20 L).

Figure 40 shows the structure factors along the $(10)_{CoO\text{-}hex}$ rod extracted from the measurements on two samples of different thicknesses, grown by 3 and 6 repetitions of the step procedure described above. A Comparison between these two curves allows to find out the incoherent scattering background contribution from the substrate, which appears close to L=-2, 1 and 4 (this contribution is the same in both samples).

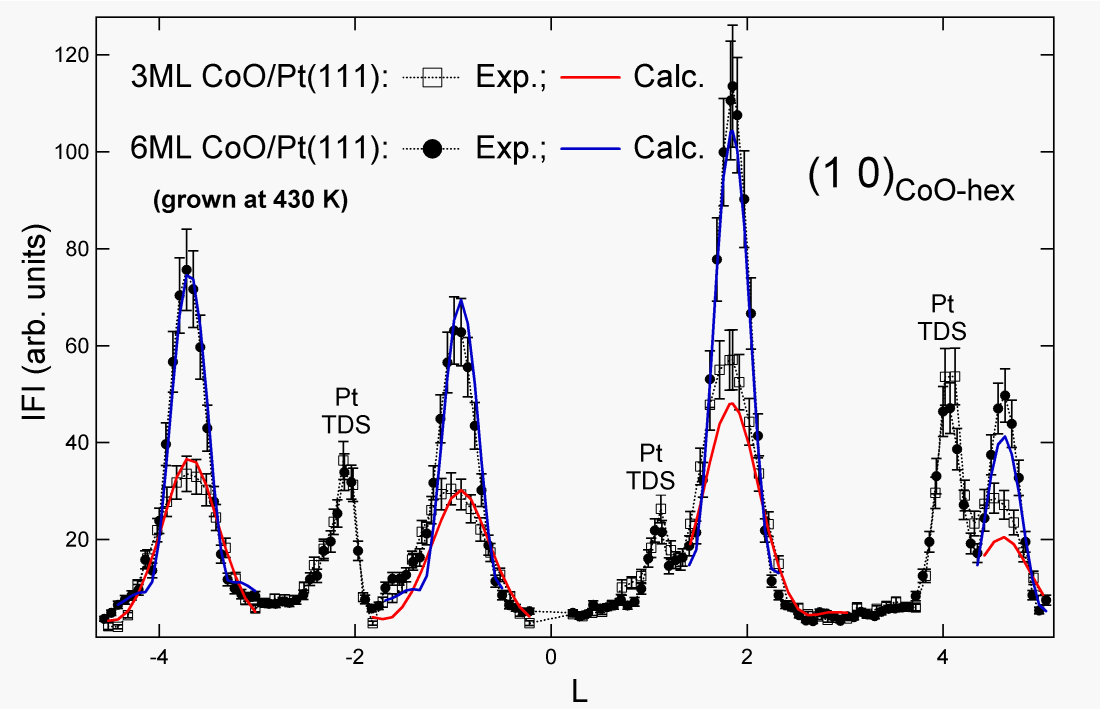

FIG. 40. $(10)_{CoO\text{-}hex}$ rod of "3 ML" and "6 ML" CoO on Pt(111). Both experimental values and best fits in the diffraction region are shown ($|F(0,1,L)|\equiv|F(1,0,\bar{L})|$).

The remaining diffraction peaks can be fitted within a simple CoO(111) layer model with bulk-like structure, because the diffraction contributions from CTRs and from the relaxed (incommensurable) film does not interfere each other [Eq.(2.18)]. A top and side view of the CoO hexagonal unit cell is shown in Fig. 41. Only three free structural parameters are required to fit the experimental data with a reasonable accuracy: the interlayer spacing, the thickness, and the film roughness. The layer by layer Co and O occupancy was modeled using the complementary error function distribution. This corresponds to a Gaussian distribution of the terraces surface.[134] The best fit values are reported in Table VI. The layer thickness is expressed in equivalent monolayers, and the r.m.s. (root means square) values are given for the roughness, which are related to the σ of the distribution.[134] The interlayer Co-O spacing is very close to the bulk one, while the roughness is similar to that one (5 Å) measured on the STM image of Fig. 38(a).

Table VI. Best fit interlayer spacing and thickness values, and r.m.s. roughness obtained from the best fit σ of the occupancy distribution.

	"3 ML" CoO/Pt(111)	"6 ML" CoO/Pt(111)	CoO bulk
$d_{Co-O}(\AA)$	1.225(2)	1.225(2)	1.230
$ML(Co)$	4	6.5	
$r.m.s.(\AA)$	3.2	4.7	

In the fit an *ABC* stacking sequence of the Co and O hexagonal layers was used, which is the same as Pt layers in the substrate. This means that the Co sub-lattice follows the reversed stacking sequence *ACB*. For this reason, while the $(10\bar{2})_{hex}$, $(101)_{hex}$, and $(104)_{hex}$ nodes are substrate Bragg peaks, the film peaks are centered at $(10\bar{4})_{CoO-hex}$, $(10\bar{1})_{CoO-hex}$, and $(102)_{CoO-hex}$. The twinned domain is not formed, otherwise the

134 ANA-ROD manual, extended version, http://www.esrf.eu/computing/scientific/joint_projects/ANA-ROD/

overall film structure would have an additional mirror plane and it would be measured that $|F(1,0,L)| \equiv |F(1,0,\bar{L})|$.

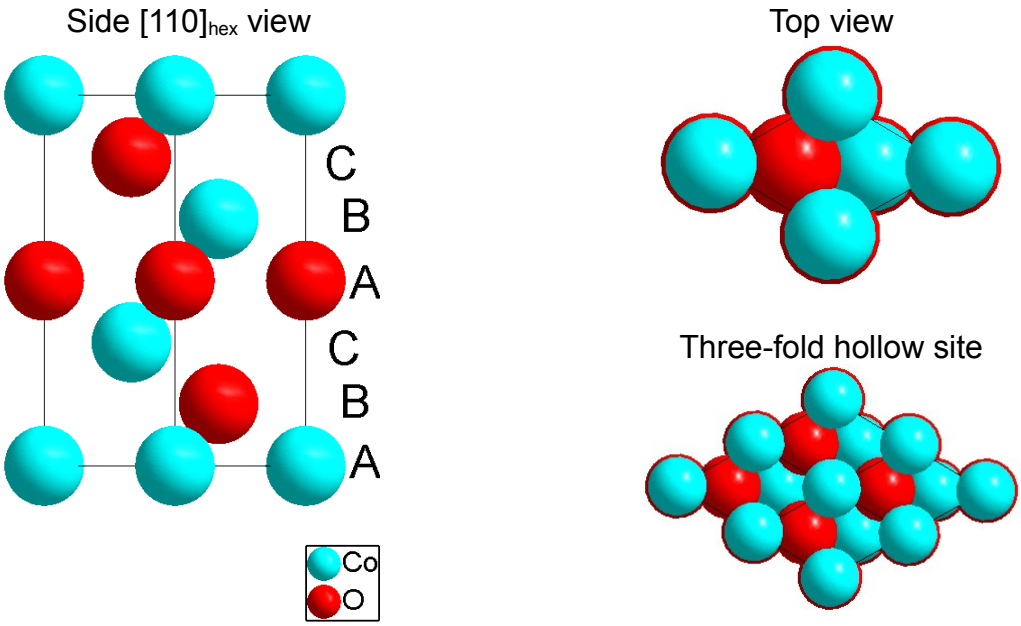

FIG. 41. Side view (a) and top view (b) of the CoO(111) hexagonal unit cell. A 2×2 surface cell is shown in (c).

Such a twinned domain is indeed observed in CoO films grown in a different manner, i.e. by oxidation at 430 K of a previously deposited 6 ML thick Co/Pt(111) layer. The single domain stacking is therefore due to interaction with the substrate during the layer by layer oxidation. This conclusion is at a first view surprising, because the site occupied by the first Co layer on top of Pt is expected to shift locally from fcc to hcp due to the misfit, as observed in the moiré sketch of Fig. 37. This difference in the local stacking would result in the growth of the two CoO domains. This apparent contradiction is solved by looking at the domain size. An in-plane Lorentzian fit of CoO rods gives ΔQ_{FWHM} ~1 nm^{-1}, i.e. a domain size of about 4 nm [Eq. (3.1)] parallel to the surface, which is of the same order of magnitude of the moiré cell size shown in Fig. 37. The inset in Fig. 38 shows a zoom taken in the flat region of STM image (a). Triangular dislocation loops are observed on it, centered on sites where the overall atomic stacking is the same of the substrate one.[125] Merte and coworkers in the Aarhus group have studied similar dislocation triangles on FeO/Pt(111).[135,136] They created these loops by chemically reducing the perfect FeO film with atomic hydrogen, whereas the structures observed here are formed during growth. They have interpreted their dislocations as vacancies in the oxygen layer. The driving force behind the formation of these defects was explained as a preference for fcc-like stacking in the upper layers (Pt-Fe-O), avoiding the regions of hcp-like stacking. In the present case triangular dislocation loops with oxygen vacancies could represent the way to lower the surface electrostatic energy. They could also simply represent a metastable state with walls between domain nucleating at different fcc sites, the growth of a defect-free moiré pattern requiring an annealing at higher temperature. They play in any case a major role in the morphology, in the stacking and in the grain size of CoO film, modifying its AFM properties.

135 L. R. Merte, J. Knudsen, L. C. Grabow, R. T. Vang, E. Lægsgaard, M. Mavrikakis, and F. Besenbacher, Surf. Sci. **603**, L15 (2009).

136 J. Knudsen, L. R. Merte, L. C. Grabow, F. M. Eichhorn, S. Porsgaard, H. Zeuthen, R. T.Vang, E. Lægsgaard, M.Mavrikakis, and F. Besenbacher, Surf. Sci. **604**, 11 (2010).

The FM PtCo/Pt(111) bilayer structure discussed in section (4.1) is Pt terminated. It is then expected that the growth of CoO on top of it proceeds in a similar manner than on clean Pt(111), and this is indeed what is observed. CoO rods measured for this layered CoO/PtCo/Pt(111) structure can hardly be distinguished from that ones shown in Fig. 40.

4.3. Magnetic properties of NiO/CoO/PtCo/Pt(111) multilayers

Perpendicular exchange bias was already observed growing CoO on top of CoPt multilayers with out-of-plane magnetic easy axis. This system exhibits enhanced coercivity and loop shifts after field-cooling, with a blocking temperature of about 220 K.[137] It is indeed quite similar to the system studied in this chapter, albeit here the FM layer is formed just by the atomic PtCo bilayer described above. In the magnetic characterization, we have coupled this FM bilayer to a AFM short period superlattice of CoO and NiO, which exhibits a single transition temperature in between the values of the respective bulk oxides.[138,139] Such a film benefits at the same time of the high magnetocrystalline anisotropy of CoO.

The studied system was grown as follow: 1 Co ML was deposited onto a clean Pt(111) substrate held at 540 K to get the structure described in paragraph (4.1). Afterwards, 1 ML Co was evaporated at 450 K and oxidized by exposure to O_2. Repeating this procedure 3 times, an epitaxial 3 ML CoO(111) layer was obtained. Following the same procedure, a 3 ML NiO(111) layer was grown on top of it. This NiO/CoO sequence was repeated 3 times, yielding an oxide film of about 4 nm thickness. A unique lattice parameter for the oxide was measured that is, within the error bar, the same as the 6 ML CoO/Pt(111) film (despite the fact the NiO bulk one is 2% smaller).

The magnetic properties of this system were characterized by polar MOKE. The sample was first heated at 383 K, then it was field cooled at room temperature under a magnetic field of 5 kOe, and hysteresis curves were measured at steps of about 10 K (Fig. 42).

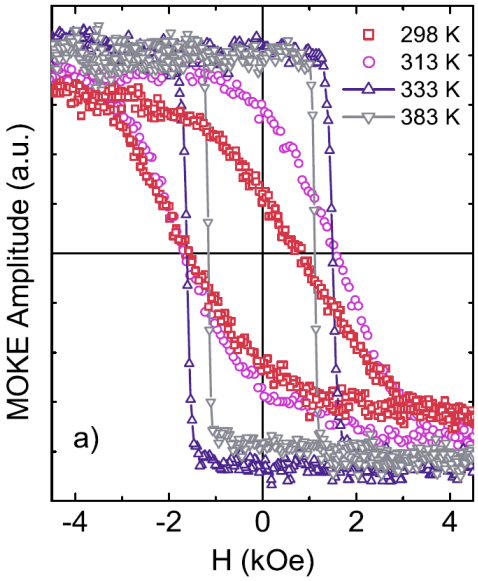

FIG. 42. Polar MOKE of $(NiO_{3ML}/CoO_{3ML})_3$/PtCo/Pt(111) versus T close to T_B.

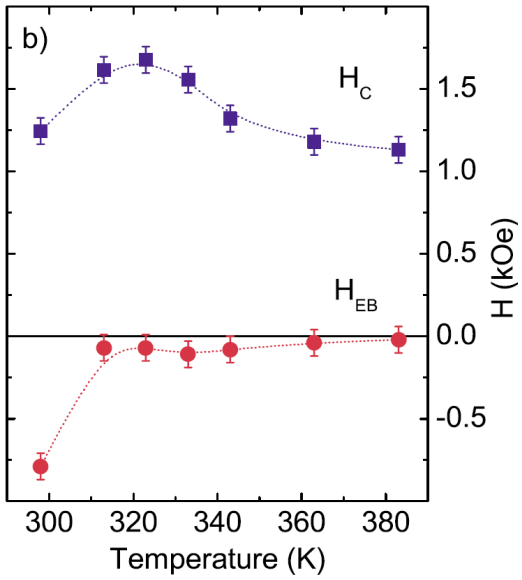

FIG. 44. Coercivity (H_C) and exchange bias (H_{EB}) versus T.

137 S. Maat, K. Takano, S. S. P. Parkin, and E. E. Fullerton, Phy. Rev. Lett. **87**, 087202 (2001)
138 M. J. Carey ,and A. E. Berkowitz, J. Appl. Phys. **73**, 6892 (1993)
139 J. A. Borchers, M. J. Carey, R. W. Erwin, C. F. Majkrzak, and A. E. Berkowitz, Phys. Rev. Lett. **70**, 1878 (1993).

From 383 K to 323 K, the hysteresis curves exhibit square loops with increasing H_C and essentially no H_{EB}. From 323 K down to 298 K, the loop becomes more and more elongated and shifted to the negative field value with decreasing H_C. The blocking temperature is inferred to be T_B 320 K (Fig. 44). This represent a large increase compared to CoO films of equivalent thickness, for which a Néel temperature of about 230 K was obtained.[140] Above T_B, the complete reversal of the out-of-plane magnetization of the Pt-Co ferromagnetic layer is observed. The increased coercivity H_C, which reaches a maximum of 1.7 kOe around T_B, is related to long range AFM order appearing in the mixed oxide layer. It is worth noting that the extrapolated value of H_C for temperature above T_N, 1.2 kOe, is close to the coercivity of the FM Pt-Co/Pt(111) bilayer (Fig. 33). Below T_B, the easy magnetization axis of the FM layer is no longer perpendicular. Upon field cooling, the AFM spins should align along the spin anisotropy axis that is closest to the applied magnetic field. The CoO has a high magnetocrystalline anisotropy. The orientation of the NiO magnetic moments is assumed to follow the CoO spins because of a lower magneto-crystalline anisotropy constant and a strong exchange interaction at the CoO/NiO interface. Hence, the change in the hysteresis loops is related to the reorientation of the Co spins in the FM layer due to exchange coupling with the oxide multilayer.

140 T. Ambrose, and C. L. Chien, J. Appl. Phys. **83**, 6822 (1998)

5. Conclusion and perspectives

My short term research projects will follow the footprint of my recent activity. They will focus on the growth and on the structural analysis of ultrathin films and nanostructures for spintronics applications. The purpose will be still to growth model systems where a complete structural knowledge will help the understanding of the magnetic properties. The tools for the structural analysis will be as in the past SXRD and STM. At short term, systems involving TMO will be privileged, which allow a comfortable *ex-situ* analysis of the magnetic properties without substantial alterations.

This research will take advantages from a few experimental improvements. The SXRD experimental set-up installed on the CRG-IF beamline, on which I have a role as local contact, will be completely renewed with a new diffractometer, a new UHV chamber, and improved growing facilities. This refurbishing is already funded.

At the Néel institute I am in charge of a variable temperature STM/AFM working in UHV and of the associated preparation chamber. It would be not very difficult to implement such an instrument for magnetic force microscopy measurements, allowing a coupled *in-situ* measurement of both structure and properties. The considered research themes would greatly benefit from such an improvement, which however is not funded up to now.

The magnetic properties will be studied mainly through two experimental techniques, the MOKE and the x-ray absorption at the transition metals $L_{2,3}$ edges. We have established a collaboration with Matthieu Jamet (CEA-INAC) for *ex-situ* MOKE measurements, and a CNRS international cooperation projects (PICS) with the MPI of HALLE which give us an access to *in-situ* MOKE.

This manuscript was dedicated to the study of AFM films and FM/AFM interfaces of interest for exchange coupling applications. The approach of growing epitaxial films on single crystal substrate has allowed to push the structural analysis as far as possible. Two class of materials have been discussed, which presents different problematics.

Most of the studied systems were conceived on the basis of the knowledges of thin film properties and structure. However, both of them can differ deeply in ultrathin epitaxial films due both to the film thickness and to the epitaxial relationships. Indeed, while the properties of FM surfaces, ultrathin film and nanostructures have been deeply investigated in the last few decades,[141,142] much less is known about Néel temperature, easy axis, interface spin structure, etc. of low dimension AFM films and nanostructures. One of the reason is the lack of well suited experimental techniques. However soft x-ray absorption spectroscopy and its related techniques like for example x-ray magnetic linear dichroism (XMLD) offer an insight into these properties.

Chemical order, roughness and intermixing at the interface with the FM layer are crucial for the properties of metallic AFM films like for example MnPt. They determine the strength of the exchange coupling interaction. As discussed in the first chapter, the roughness allows the establishment of a directional anisotropy at compensated FM/AFM interfaces. The size of chemically ordered domains play a role on one hand by limiting the correlation

141 C. A. F. Vaz, J . A. C. Bland, and G. Lauhoff, Rep. Prog. Phys. **71**, 056501 (2008)
142 F. J. Himpsel, J. E. Ortega, G. J. Mankey, and R. F. Willis, Advances in Physics **47**, 511 (1998)

length of AFM domains, on the other hand allowing unbalanced spins which bring to a net magnetic moment.

In chapter 3 it was shown that exchange bias with coupling perpendicular to the surface is observed in FePt layers grown on well ordered MnPt/Pt(001) films. In this system indeed an exchange bias is not expected for the ideal interface, which is compensated both considering type II and type III (bulk) magnetic order (see Fig.14). The observed EB disappears after several hysteresis cycles (training effect). This can be explained in the domain state model with a rearrangement of the AFM domains. XMCD measurements performed on this system after field cooling at 5 K evidenced the presence of uncompensated Mn spins.[54] Most of them are strongly coupled with the FM layer and turn with it, but a fraction is frozen, at least during a few hysteresis loops, and is responsible for the observed exchange bias. A deeper insight into the coupling mechanism can be gained trough the knowledge of the spatial distribution of such uncompensated spins. Details about the magnetization depth profile in the MnPt film and at the interface can be provided by x-ray resonant magnetic scattering (XRMS) in specular geometry at the Mn L_3 edge. The Mn spin frozen spatial distribution can be deduced comparing four reflectivity measurements collected at the Mn edge resonance, at low temperature and after field cooling. The difference between the x-ray reflectivity collected with circular left and circular right polarized x-ray beam is first measured, which gives the uncompensated spin distribution. Then a magnetic field in applied that reverse the FM layer magnetization. Measuring once more the reflectivity dichroism, the distribution of uncompensated spins after flipping the magnetization is obtained, which allows to deduce the frozen fraction. This experiment has been already conducted by our group on the SEXTANTS beam line at SOLEIL using the RESOXS end station, and the data analysis is in progress.

For Fe films coupled with MnPt a stable exchange bias parallel to the surface was observed. However this sample suffer of an important drawback, showing ordered MnPt domains of small size, and with the c axis either perpendicular or parallel to the surface. The last one form a uncompensated interface with the FM iron layer when the type II AFM order is realized, which could explain the observed exchange bias.

The second class of EB systems discussed in this manuscript involve TMOs, mainly CoO, which is widely employed as AFM layer in studies which aim to compare the experimental results with the expected theoretical behaviors. The dependence of the magnetic properties of AFM layers on the film thickness is well understood from the theoretical point of view.[124] Experimentally, a strong reduction in the Néel temperature with the thickness of the AFM layer in the nanometric range was observed in CoO/SiO_2 multilayers.[62] An even larger decrease of the experimentally more accessible blocking temperature was measured in NiFe/CoO bilayers.[140] However in such films little is known about the structure and the spin arrangement at the interface. Indeed, the suppression in T_N is strongly reduced in CoO/MgO multilayers.[143] This discrepancy was explained with the presence, in CoO/SiO_2 multilayers, of an amorphous CoO layer at the interface,[144] while in the permalloy/CoO system the origin of the decreased blocking temperature with respect to the bulk T_N stay unknown.

These experiments have motivated the study of the detailed structure of the TMO layer employed in ultrathin exchange bias systems. In the case of epitaxial CoO/Pt(111) films, the substrate plays a fundamental role, because as I showed it determines both the strain

143 E. N. Abarra, K. Takano, F. Hellman, and A. E. Berkowitz, PRL 77 3451 (1996)

144 Y. J. Tang, David J. Smith, B. L. Zink, F. Hellman, and A. E. Berkowitz, PRB 67, 054408 (2003)

and the grain size of ultrathin films. Both of them, affect the spin configuration of the CoO layer. The AFM ordering between Co ions is stabilized by superexchange which is mediated by the oxygen atoms.[145,146] The presence of triangular dislocation loops like that ones shown in the inset of Fig. 38, which are explained with the lack of oxygen atoms, are expected to deeply modify the spin configuration at the interface.

Lattice distortion and CoO magnetic properties are intimately related.[98] In the octahedral crystal field associated to the cubic structure, the two minority spin electrons of the Co^{+2} ion are distributed in three degenerate t_{2g} orbitals. This degeneracy is removed by a tetragonal distortion (Jahn-Teller effect). This results in an orbital momentum and in a spin momentum whose orientation is mainly determined by the spin-orbit coupling. However exchange and correlation also contribute in determining the easy axis, turning it out of the [001] direction. The monoclinic distortion which adds to the tetragonal one would then have its origin in the magnetostriction.[96] Than, it seems logical that lattice induced distortion can modify considerably the establishment of the AFM order and the spin orientation.

The role of the epitaxial strain on the magnetic properties of AFM films has been hardly considered up to now. It was observed that the orientation of the magnetic moments strongly depend on the strain in CoO(001) ultrathin films.[147] The lattice constant of CoO sandwiched by MnO(001) layers is expanded in-plane, and spins are oriented out-of-plane. CoO/Ag(001) suffer a compressive strain, and as a result the Co spins are in-plane.

On the basis of the relationship between AFM order and monoclinic distortion, the following question arise that seems very interesting: is it possible to manipulate the Néel temperature in CoO ultrathin films by epitaxial growth induced distortions ? To inquire this aspect we are performing a few experiments on the CoO/Pt(001) and CoO/FePt/Pt(001) systems. Growth of cobalt oxide by reactive molecular beam epitaxy on a Pt-terminated PtFe/Pt(001) surface gives rise to a monoclinic distorted CoO film at room temperature for thicknesses in the nanometer range.[148] Its structure is close to that one of a rocksalt CoO(111) film, forming hexagonal atomic planes parallel to the interface. The epitaxy induced stress being not the same along the CoO $[1\bar{1}0]$ and $[11\bar{2}]$ directions, a monoclinic distortion is observed at room temperature. This could explain the unusually high blocking temperature (~290 K) that we measure on this system. The elemental resolved spin orientation in such films can be investigated using linear and circular magnetic dichroism at the Fe and Co $L_{2,3}$ x-ray absorption edges. The x-ray absorption linear dichroism (XLD) probes the charge anisotropy associated to both the local crystal field and the local exchange field through the spin-orbit coupling.[147,149,150] The experiments we performed on CoO/FePt/Pt(001) has allowed to find the Co spin orientation, and the coupling of Co and Fe spins through the interface.[151] These measurements give also directly the Néel temperature of the film. A systematic study of spin orientation and T_N needs to be performed as function of the oxide layer thickness.

Even more crucial for the exchange properties is the manipulation of the epitaxial

145 P. W. Anderson, Phys. Rev. **79**, 350 (1950).
146 P. W. Anderson, Solid State Phys. **14**, 99 (1963).
147 S. I. Csiszar, M.W. Haverkort, Z. Hu, A. Tanaka, H. H. Hsieh, H.-J. Lin, C. T. Chen, T. Hibma, and L. H. Tjeng, Phys. Rev. Lett. **95**, 187205 (2005).
148 A. D. Lamirand, M. M. Soares, M. De Santis, H. C. N. Tolentino, A. Y. Ramos, submitted to J. Appl. Phys.
149 J. Wu, J. S. Park, W. Kim, E. Arenholz, M. Liberati, A. Scholl, Y. Z. Wu, C. Hwang, and Z. Q. Qiu, Phys. Rev. Lett. **104**, 217204 (2010).
150 G. van der Laan, E. Arenholz, R. V. Chopdekar, and Y. Suzuki, Phys. Rev. **B 77**, 064407 (2008).
151 A. D. Lamirand, M. M. Soares, A. Y. Ramos, H. C. N. Tolentino, M. De Santis, J. C. Cezar, A. de Siervo, and M. Jamet, Phys. Rev. B **88**, 140401(R) (2013)

growth relationship. Both the structural characteristic of the substrate surface and its chemical nature play a crucial role in the growth of epitaxial films. Interface stress and interfacial energy determines the crystallographic orientation of the film. In the growth of CoO on metallic (100) surfaces, the (100) orientation is preferred for low strain values like for CoO on Ag(100) (see for ex. Ref. [152]). For large strain, as for CoO/Ir(100), (111) films are usually observed.[120] This qualitatively agrees with our findings for CoO/Pt(001). It has been recently shown that the CoO growth orientation on Ir(100) can be tuned to (100) by controlling the chemistry at the interface.[153] Such a switching is achieved by the deposition of a buffer layer of almost 2 ML Co on the clean (unreconstructed) surface. Such an ultra-thin layer is pseudomorphic, and after a moderate oxidation it forms a c(4x2)-Co_3O_4/Co/Ir(100) surface. Such a phase becomes the precursor for the growth of CoO(100), which is obtained by further Co reactive deposition in oxygen.

We are actually successfully growing CoO/FePt/Pt(100) EB systems where the oxide films is (100) oriented. This is achieved using the method described above, i.e. depositing a Co buffer layer at the interface. The magnetic properties of such a multilayer deeply differ from that ones of the system with the same chemical composition but with a CoO(111) oriented film. The origin of such a difference in exchange coupling could reside in the interface structure and stoichiometry, which need to be carefully investigated.

These topics and more in general the relationship between EB properties and film structure is part of the Phd thesis (in progress) carried out in our group by A. Lamirand.

A second subject that we are going to investigate in the next years involve magnetite, and is a continuation of the study of the CoO/Fe/Ag(001) EB system which was part of the Phd thesis of Marcio Soares.[54]

It is well known that (001) oriented bcc iron grows layer by layer and pseudomorphic on Ag(001) up to a few nanometer thickness. A spin reorientation transition is also observed from out of plane to in-plane above a thickness of 4-5 ML.[154,155,156] In our group we have studied the CoO/Fe/Ag(001) system, which seemed well suited to inquire the influence of the interfacial chemical composition on exchange bias and anisotropy properties.[157] We observed that an iron oxide is formed at the interface, which play a crucial role in the magnetic properties of the system.[158] To answer to the question about the role of iron oxide at the interface we plan to study the CoO/Fe_3O_4/Ag(001) bilayer.

The CoO/Fe_3O_4 system has several peculiar characteristic and it has been deeply studied in the past.[159,160,161] At room temperature the magnetite is ferrimagnetic and

152 P. Torelli, E.A. Soares, G. Renaud, S. Valeri, X.X. Guo, P. Luches, Surf. Sci. 601 (2007) 2651

153 M. Gubo, C. Ebensperger, W. Meyer, L. Hammer, K. Heinz, F. Mittendorfer, J. Redinger, Phys. Rev. Lett. 108, 066101 (2012).

154 M. Stampanoni, A. Vaterlaus, M. Aeschlimann, and F. Meier, Phys. Rev. Lett. **59**, 2483 (1987).

155 Z. Q. Qiu, J. Pearson, and S. D. Bader, Phys. Rev. Lett. **70**, 1006 (1993).

156 D. M. Schaller, D. E. Bürgler, C. M. Schmidt, F. Meisinger, and H.-J. Güntherodt, Phys. Rev. B **59**, 14516 (1999).

157J. Wu, J. S. Park, W. Kim, E. Arenholz, M. Liberati, A. Scholl, Y. Z. Wu, Ch. Hwang, and Z. Q. Qiu, Phys. Rev. Lett. **104**, 217204 (2010).

158 R. Bali, M. M. Soares, A. Y. Ramos, H. C. N. Tolentino, Fikret Yildiz, C. Boudot, O. Proux, M. De Santis, M. Przybylski, and J. Kirschner, Appl. Phys. Lett. **100**, 132403 (2012)

159 P. J. van der Zaag, A. R. Ball, L. F. Feiner, R. M. Wolf, and P. A. A. van der Heijden, J. Appl. Phys. **79**, 5103 (1996)

160 Y. Ijiri, T. C. Schulthess, J. A. Borchers, P. J. van der Zaag, R.W. Erwin, Phys Rev Lett **99**, 147201 (2007)

161 P. J. van der Zaag and J. A. Borchers, in “Magnetic Properties of Antiferromagnetic Oxide Materials”, WILEY-VCH (2010), edited by L. Duo, M. Finazzi and F. Ciccacci.

crystallizes in the inverse spinel structure (AB_2O_4).[162] This can be viewed as a fcc oxygen lattice with Fe^{3+} cations occupying tetrahedral Fe (*A*) sites and a 1:1 mixture of Fe^{2+} and Fe^{3+} cations occupying 1⁄2 of the Fe (*B*) octahedral interstitial sites. It has been shown, on single crystal films grown on MgO, that antiphase boundaries play an important role for its magnetic properties.[163]

The magnetite has a lattice constant of 8.397 Å, but the oxygen sublattice has the same arrangement in CoO and Fe_3O_4 with a misfit of 1.5 %, and a good (pseudomorphic) epitaxy relationship is therefore expected. On such a system a very small critical thickness, ~0.4 nm, was observed for the onset of biasing.[159] It seems a very good candidate for inquiring the relationship between thickness, distortion, domains size and blocking temperature. We have recently grown such CoO/Fe_3O_4/Ag(001) interface. Both structural and magnetic studies are in progress.

A research direction that we aim to explore in the next years is the growth of exchange coupled magnetic particle arrays self-organized on nanostructured templates. The synthesis of artificial magnetic nanoparticles is motivated by the application in magnetic data storage. Shrinking the size below a domain wall thickness favors a single-domain behavior. However, reducing the size in the tenth of nanometer range one fall into the superparamagnetic limit where a spontaneous flip of the magnetization can happen by thermal activation. It has been shown however that the superparamagnetic limit can be beated thanks to exchange coupling.[164] For proper investigations and applications of magnetism at the nanometer scale, obtaining clusters with well-aligned easy axes and monodisperse size distribution is a key challenge, resulting in well-defined properties.[165,166]

The surface morphology at the nanometers scale has been exploited in the past two decades to achieve specific and regular atomic cluster arrangements. An example of such artificial nanostructures is the elaboration of regularly spaced Cu and Co atomic chains[167,168] or nanoparticles[165] at step edges of vicinal Pt and Au surfaces. An other well known example is the self-organization of Co nanoparticles on the Au(111) herring-bone reconstruction.[169] More recently, nanostructured epitaxial ultrathin TMO films grown on metals, as for example the moiré and the zigzag pattern resulting respectively from the growth of a single FeO bilayer on Pt(111),[170,171] and of TiO_x/Pt(111),[172] as well as the (4×4) vanadium oxide mesh on Pd(111),[173] were used for this same purpose. In this framework we tried to grow Pd nanoparticles by deposition on the CoO/Pt(111) moiré structure described in the previous chapter, but we observed that the periodicity of the template

162 See for ex.: F. Walz, J. Phys.: Condens. Matter, **14** R285 (2002)

163 D. T. Margulies, F. T. Parker, M. L. Rudee, F. E. Spada, J. N. Chapman, P. R. Aitchison, and A. E. Berkowitz, Phys. Rev. Lett. **79**, 51621 (1997)

164 V. Skumryev, S. Stoyanov, Y. Zhang, G. Hadjipanayis, D. Givord and J. Nogués, Nature **423**, 850 (2003).

165 N. Weiss, T. Cren, M. Epple, S. Rusponi, G. Baudot, S. Rohart, A. Tejeda, V. Repain, S. Rousset, P. Ohresser, F. Scheurer, P. Bencok, and H. Brune, Phys. Rev. Lett. **95**, 157204 (2005)

166 S. I. Woods, J. R. Kirtley, Shouheng Sun, and R. H. Koch, Phys. Rev. Lett. **87**, 137205 (2001)

167 P. Gambardella, M. Blanc, H. Brune, K. Kuhnke, and K. Kern, Phys. Rev. B **61**, 2254 (2000).

168 P. Gambardella, A. Dallmeyer, K. Malti, M. C. Malagoli, W. Eberhardt, K. Kern, and C. Carbone, Nature **416**, 301 (2002).

169 O. Fruchart, P.-O. Jubert, C. Meyer, M. Klaua, J. Barthel, J. Kirschner, J Mag Mag Mat **239**, 224 (2002)

170 N. Berdunov, G. Mariotto, K. Balakrishnan, S. Murphy, and I. V. Shvets, Surf. Sci. **600**, L287 (2006).

171 L. Giordano, G. Pacchioni, J. Goniakowski, N. Nilius, E. D. L. Rienks, and H.-J. Freund, Phys. Rev. Lett. **101**, 026102 (2008).

172 E. Cavaliere, I. Kholmanov, L. Gavioli, F. Sedona, S. Agnoli, G. Granozzi, G. Barcaro, and A. Fortunelli, Phys. Chem. Chem. Phys. **11**, 11305 (2009).

173 S. Hayazaki, T. Matsui, H. Zhang,W. Chen, A.Wee, and J. Yuhara, Surf. Sci. **602**, 2025 (2008).

layer is destroyed during such a process.

Ultrathin alumina obtained by oxidation of a $Ni_3Al(111)$ substrate offers ideal properties for template-mediated growth of self-organized two-dimensional arrays of clusters. The structure of this 0.5-nm-thick oxide film exhibits holes reaching down to the metal substrate, which are located at the corners of a $\sqrt{67}\times\sqrt{67}\,R12.2°$ unit cell.[174,175] These holes are large enough to trap any kind of metal atoms, but only Pd atoms have been shown to be trapped so far. This template is especially useful because it combines large distances between the nucleation sites (4.1 nm) with the possibility to grow three-dimensional clusters, allowing to tune the cluster size in a range of more than 2 orders of magnitude. The applicability of this alumina film as a template for growing well-ordered metal clusters was first demonstrated for Pd and Pd/Au.[176] The unmodified oxide is not a good template for most other metals. However, once that the corner holes are filled with Pd atoms, a metallic nucleation site is created where other metal atoms such as Fe and Co can nucleate and form a well-ordered arrangement, too.[174] Figure 45, taken from ref. [177], show a regular arrangement of Co nanoclusters, obtained by deposition of 0.06 nm of Co at 470 K on the surface oxide were three Pd atoms per corner hole were predeposited.

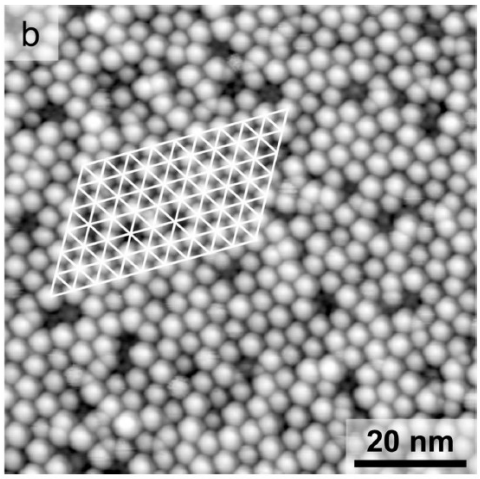

Fig. 45. STM of 0.06 nm Co deposited on the Pd seeded $Ni_3Al(111)$ $\sqrt{67}\times\sqrt{67}\,R12.2°$ surface oxide at 470 K. Cross points of the white grids mark the corner holes.

Using MOKE it was observed that such Co cluster have a superparamagnetic behavior at least down to a temperature of 100 K, were the substrate itself becomes ferromagnetic.[178]

It was shows that the exchange coupling, providing an extra source of magnetic anisotropy, can lead to a stabilization of the magnetization in Co nanoparticles embedded in a CoO matrix.[164] It seems therefore quite appealing to try to built a similar system growing a CoO oxide layer on top of the monodisperse nanostructures shown in Fig. 45. It would have the advantage, for fundamental investigations, which is epitaxially grown on the oxide surface.

174 M. Schmid, G. Kresse, A. Buchsbaum, E. Napetschnig, S. Gritschneder, M. Reichling, and P. Varga Phys. Rev. Lett. **99**, 196104 (2007).
175 G. Hamm, C. Barth, C. Becker, K. Wandelt, and C. R. Henry, Phys. Rev. Lett. **97,** 126106 (2006)
176 S. Degen, C. Becker, and K.Wandelt, Faraday Discuss. **125**, 343 (2004).
177 A. Buchsbaum, M. De Santis, H. C. N. Tolentino, M. Schmid, and P. Varga, Phys. Rev. B **81**, 115420 (2010)
178 M. Schmid, private communication.

It should also be possible to grown alloy nanoparticles such as CoPd or CoPt on top of such a surface oxide. This is expected to increase further the magnetic anisotropy and to protect the core against oxidation. This nanoparticles, covered by a CoO layer, would be the counterpart of the nanofilms discussed in the previous chapter.

Transition metal carbides (TMC) is other class of interesting substrate for the growth of exchange coupled nanoparticles. They are mostly known for their outstanding wear resistance and for their chemical stability in a hostile environment. The (110) face of TMCs tends to reconstruct with a ridge-and-valley morphology. We studied in details $VC_{0.8}$(110), which shows two different structures with (3×1) and (4×1) periodicities, obtained for different annealing temperatures. Both phases reconstruct with a missing row configuration. The surface has a ridge-and-valley structure resulting from {10 0} faceting.[179]

Figure 46 shows the STM of 0.5 ML Co deposited on $VC_{0.8}$(110) at 480 K. In the image it is observed that Co growth mainly in the valley, but large clusters form due probably to the large mobility along the $(1\bar{1}0)$ direction.[180]

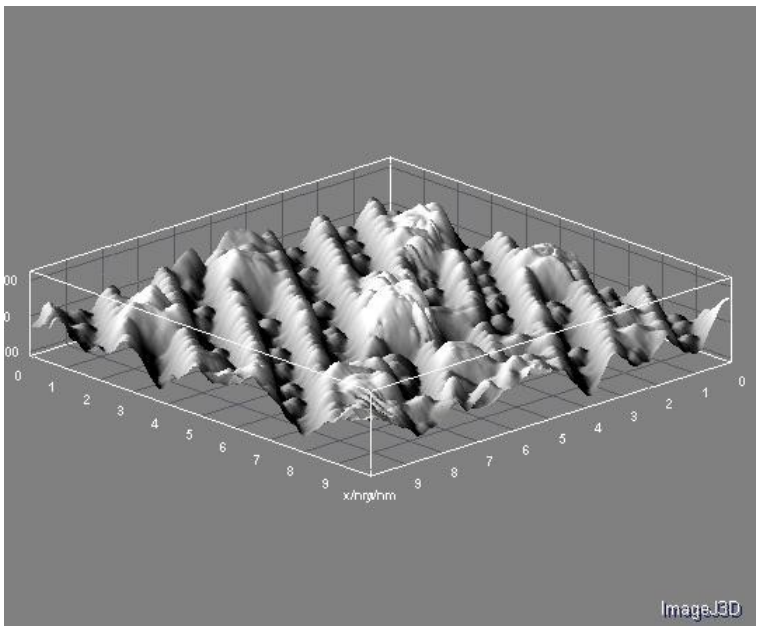

Fig. 46. STM of 0.5 ML Co/$VC_{0.8}$(110) grown at 480 K

Such a {100} faceting of TMCs should be very stable. A large period of steps and kinks is then expected on vicinal surfaces, which would be more suitable for nanostructures growth.

A further thematics that we plan to develop in the next years involve the use of the TMO layers, mainly CoO and NiO, as template for the growth of molecular assembly. This subject is a collaboration with Veronique Langlais of CEMES-Toulouse, with is the coordinator of a related ANR project. In the framework of nanoelectronics development, the use of single molecules or molecular assemblies as active components is considered as a promising way to design and fabricate at atomic scale nanosized integrated electronic

179 Y. Gauthier, I. Zasada, M. De Santis, V. Langlais, C. Virojanadara, L.I. Johansson, Surf. Sci. **601**, 3383 (2007)

180 M. De Santis, M. Schmid, P. Varga, unpublished.

devices. Technologies based on organic semiconductor devices such as organic light emitting diodes (OLEDs), organic photovoltaics (OPVs), organic field effect transistors (OFETs) and organic memory have seen major improvements and have already begun to be used in devices. A successful application is found in ultra-high-resolution OLED displays. The rapid development of the organic electronics is the result of a large-scale concerted effort from the science and engineering research community. These devices involve the use of multiple layers composed by various materials. Operating such devices requires charge carriers to pass through these layers and therefore electrons should cross several interfaces along their paths. The quality of these interfaces in terms of structure, electronic properties, roughness and stoichiometry is the key parameter that strongly influences the overall performance of the devices. All these hybrid components imply organic materials but also require insulating barriers to electronically decouple the molecules from metal or low resistance charge carriers to inject either electrons or holes into the organic layers. In the studies performed at the fundamental level, wide bandgap alkali halides are used as insulating layers and enable the control of the charge state of individual molecules and assemblies. Nevertheless, alkali halides could hardly be used for technological applications. The relevant alternative to alkali halides films is encountered in oxide, especially in oxide thin films. The structural and electronic quality of these thin films dictates the performance of the devices since their work function directly depends on the surface roughness, crystal face, impurities and stoichiometry of the oxide.

Our objective is to study bistable organometallic complexes on top of NiO(001) and CoO(001) films epitaxially grown on various substrates (Ag, Au and MgO), as electron trapping elements,[181,182] with several potential applications like for example for charge storage based memories. A key issue is to grow high structural quality oxide ultrathin films in a controlled fashion since defects are proven to play an important role in adsorption. Scanning Tunneling Microscopy (STM) imaging and spectroscopy will be used to detect the presence of structural defects and the oxide films electronic properties (bandgap and work function) as a function of the thickness. The film growth will be monitored by Grazing Incidence X-Ray Diffraction (GIXRD) to get precise information on domain size, roughness and interface quality with the metallic substrate. Then bistable M-(bis-dibenzoylmethanato) organometallic molecules (M=Cu, Zn, Ni) having different d shell configurations will be deposited on these ultrathin films and the overall structure and properties will be inquired, in order to get a deep understanding of electron or hole trapping mechanism.

181 T. Leoni, O. Guillermet, H. Walch, V. Langlais, A. Scheuermann, J. Bonvoisin, and S. Gauthier, Phys. Rev. Lett. **106**, 216103 (2011)

182 H. Walch, T. Leoni, O. Guillermet, V. Langlais, A. Scheuermann, J. Bonvoisin, and S. Gauthier, Phys. Rev. B **86**, 075423/1-7(2012)